Investigation of Creep Characteristics for Stresses close to Failure

Experiments and Anaysis

Jørgen Rasmussen Olsen

Abstract

This study consists of a series of experiments set up to investigate the active processes in creep, with emphasizes on unloading and recovery of strain. The experiments were performed on dry 1x2 inch cylindrical core samples of Castlegate, tested with a uniaxial electromechanical load frame. The strain was measured using high precision displacement sensors (LVDT's) and strain gauges, while recording acoustic P-wave velocities and monitoring the temperature. Each test have been performed over a period of 20-24 hours, with incremental changes in stress, both loading, unloading and reloading, with hold periods of 2-4 hours. The stress is typically increased to a state near failure in the beginning of the experiment, before it is decreased in increments toward the end. The series of experiments resulted in 5 high quality data sets.

Existing models have been used in attempts to reproduce the measured data from the experiments. The Burger's model was able to reproduce the measured data to high precision, given a sufficient number of free variables. However using only one set of parameters the model could only reproduce the first increase in stress, leaving the remainder of the interval far off the measured data. The parameters obtained when fitting the data was deviating between each sample, especially the viscosity based parameters. The elastic parameters were also found to decrease for each drop in stress, meaning that the instant elastic recovery increased. The FORMEL model was fitted using three free variables, less than the Burger's model, however the interval which was possible to predict was smaller. The FORMEL model is still unable to predict strain recovery.

Further experiments were compared to each other in the search for repeating trends. It was found that the P-wave velocity increased during hold periods with constant stress following a decrease in stress. This observation coincides with existing knowledge of hold periods following increases in stress, where the P-wave velocity decreases. Another interesting observation during reloading showed P-wave velocities increased during hold periods following reloading to previously held stress levels.

Sammendrag

Denne avhandlingen består av en serie av eksperimenter, gjennomført med formål om å undersøke hvordan tidsforsinket deformasjon påvirkes av forskjellige spenningsstier. Eksperimentene ble uført på tørkede, sylindriske kjerner av Castlegate med dimensjoner på 1x2 tommer, ved hjelp av en en-aksiell elektromekanisk lastramme. Deformasjonen ble målt ved hjelp av deformasjons følere (LVDT) og strekklapper, samtidig som akustiske målinger ble gjennomført for å undersøke hvordan P-bølge hastighetene varierte under eksperimentet. Hver enkelt test ble gjennomført i løpet av en periode på 20-24 timer, der spenninger ble holdt konstant ved ulike spenningsnivå i 2-4 timer. En typisk spenningssti innebærer at spenningen først blir økt til et nivå nære brudd, før den trinnvis blir redusert. Av de utførte eksperimentene endte totalt fem eksperimenter med gode resultater.

Eksisterende modeller har blitt brukt i forsøk på å reprodusere eksperimentelle data. Burger's modellen var i stand til å gjenskape de målte dataene til en høy nøyaktighet, gitt at tilstrekkelig antall sett parametere ble brukt. Ved bruk av kun et sett parametere var imidlertid modellen ikke i stand til a å reprodusere de målte dataene for hele eksperimentet. Parameterne som ble funnet avvek fra hverandre om en sammenlignet flere eksperimenter, særlig parameterne relatert til viskositet varierte. En annen oppdagelse er at den elastiske parameteren blir mindre for vær gang spenningen blir redusert, noe som betyr at den umiddelbare ekspansjon øker selv om reduksjonen av spenning er lik. FORMEL modellen ble tilpasset de målte dataene ved hjelp av tre frie variabler, noe som er færre enn Burger's modellen. Intervallet som modellen er i stand til å reprodusere er imidlertid mindre.

Videre ble de eksperimentelle dataene sammenlignet med hverandre for å forsøke å finne trender. Det ble oppdaget at P-bølgehastighetene økte i perioder med konstant spenning etterfulgt av en reduksjon i spenning. Denne observasjonen sammenfaller med eksisterende kunnskap om P-bølgehastigheter i perioder med konstant spenning, etterfulgt av en spennings økning, der hastigheten faller som en funksjon av tid. En annen bemerkelsesverdig observasjon relatert til P-bølger, indikerte at bølgehastigheten i perioder med konstant spenning etterfulgt av gjentatte opplastning til et gitt nivå førte til en i hastighet, snarere enn en reduksjon.

Preface

This master thesis is the culmination of 5 years of study within the field of Petroleum Engineering with the Department of Petroleum Engineering and Applied Geophysics at the Norwegian University of Science & Technology. The thesis has been conducted in cooperation with SINTEF, which has provided facilities and equipment for the experiments, in addition to academically strong support during the course of this thesis.

I would like extend my gratitude to my supervisor Erling Fjær for the support over the course of the thesis. I would like to thank Anna Stroisz for instructions and help during the start-up phase of the experiments. I would also like to thank the rest of the group at the SINTEF lab for useful tips and help during the course of the experiments.

Table of contents

List of figures

List of tables

Nomenclature

A	Material dependent constant in FORMEL model
c	Half the length of a pre-existing crack
d	Grain size
E	Young's modulus
E^*	Simplified dynamic Young's modulus
E_1	Spring characteristic of the Kelvin-Voigt model
E_2	Spring characteristic of the Maxwell model
E_e	Dynamic Young's modulus
E_{eff}	Effective Young's modulus
F	Additional non-elastic deformation caused by shear loading
f_i	Model value
G	Shear modulus
G_c	Critical strain energy release rate
H	Uniaxial compaction modulus
K	Bulk modulus
K_I	Tensile stress intensity factor
K_{Ic}	Critical tensile (mode-I) fracture toughness.
L	Length
n	Parameters controlling the strain contribution in FORMEL model
P_z	Non-elastic compliance due to axial loading
Q	Coefficient depending on shape and orientation of cracks
q	Inverse of the current strain at the time of failure
R	Resistance
R^2	Statistical parameter related to the distance between two data series
S	Material dependent constant in FORMEL model
SS_{res}	Residual sum of squares
SS_{tot}	Total sum of squares
t	Time
T	Temperature

t_c	Time at which stress is changed
v_P	P-wave velocity
$\bar{y}$	The average of the measured data series
y_i	Measured value

$\dot{\varepsilon}$	Strain rate
ε	Stain/Deformation
ζ	Uncertainty, related to temperature
η	Coefficient of viscosity
η_1	Viscosity characteristic of the Kelvin-Voigt model
η_2	Viscosity characteristic of the Maxwell model
v	Poisson's ratio
ξ	Crack density
ρ	Density
σ	Stress
σ^*	Crack propagation stress
σ_c	Critical stress for closing a crack
σ_f	Fracture limit
σ_y	Stress limit of onset of micro plasticity
τ	Characteristic time of creep cycle in FORMEL model

List of abbreviations

AE	Acoustic emissions
K-V	Kelvin-Voigt
LVDT	Linear Variable Differential Transformer
M.	Maxwell
SD	Squared difference
UCS	Uniaxial (Or unconfined) compressive strength

1 Introduction

Modelling and predicting time dependent deformation in rocks is a useful and important tool in the design of underground cavities such as salt mines, shafts and boreholes, the latter being related to reservoir compaction, subsidence, casing design and permanent barriers. To permanent barriers the application of modelling, is predicting the expected time before the formation seals around the casing. A wide range of studies have previously been conducted with the purpose of investigating parameters impacting the characteristics of creep. Various models have been suggested to reproduce data and predict the behavior of several types of rock. Among these models are simple viscoelastic models like the Burgers model and more complex ones, like the FORMEL model. It is known that these models can predict rocks response to increases in stress reasonably well, while the recovery of deformation is harder to model.

This Master Thesis is the continued work of the Specialization Project: "Creep investigation: - Experiments and model fitting", completed in the fall of 2014. The aim of the previous project was to investigate the time dependent effects of loading and unloading on Castlegate cores. The experiments were conducted on a manual load frame, which yielded highly temperature dependent results, not suitable for discussion in fine detail.

In this study a new series of experiments has been conducted with a goal to obtain new information about rocks response to different stress paths, with emphasize on unloading, using stresses close to failure. The experiments have been performed using a uniaxial electromechanical load frame. Dried cylindrical Castlegate and Saltwash South core samples with dimensions of 1.0 x 2.0 ″ and 1.5 x 3.0 ″ (diameter x length) respectively, have been used. Data has been acquired using load cells, LVDT's, strain gauges, acoustics (P-wave) and temperature sensors.

The thesis will apply the experimental data and test several scenarios of the Burger's model to investigate if, and optionally why and when, the model fails to predict time dependent deformation. In addition it will check the FORMEL models applicability. Further the acoustic data will be used to support observations in the strain data set, and to discuss how crack densities and creep affect P-wave velocities.

1.1 Thesis structure

The thesis is structured in to 5 main chapters:

- Chapter 2: The *Background theory* presents existing theory and models applied in the rest of the thesis
- Chapter 3: *Equipment and methods* describes the setup, cores and measuring equipment, along with the method and procedure used to perform the experiments
- Chapter 4: *Experimental results* is an overview and explanation of the results from the experiments. More detailed visualizations of the data can be seen in Appendix IV
- Chapter 5: In the *Discussion* creep models are applied to find interesting characteristics for the defamation data. Also the acoustic data is discussed in relation to
- Chapter 6: The *Conclusion* summarizes the most important findings and results

1.2 Previous work

The Specialization Project was completed as part of the Master's degree in the 9th semester. A series of experiments with varying stress were conducted and data was successfully obtained. However the recorded data was strongly influenced by temperature fluctuations. Some of the affected data was corrected, but intervals where the temperature changed too rapidly were not successfully corrected. No clear conclusion could be drawn on what part of the experimental setup was most affected by the temperature variations.

Although some of the data was of poor quality 6 experiments was fitted to the Burgers and 8 fitted to the FORMEL model. However the fitting parameters found for the two models did not match particularly well between experiments.

When stress was reduced or removed it was discovered that the recovery of the deformation did not match the elastic and transient response predicted by the Burger's model. The elastic recovery was smaller than expected and the transient recovery was smaller or absent.

The most important realization throughout the project was that the temperature had a very large impact on the strain data. It was not believed that the fluctuations of the strain were caused by creep effects alone, rather the opposite, it had no or very small effects. The cause was suspected to originate from the experimental setup.

2   Background theory

2.1   Introduction to creep

Creep is the time-dependent deformation occurring in rocks and other materials when it is subjected to a constant stress. It is related to the viscoelastic response of the solid framework and can be observed both in dry and wet rocks (Fjær, Larsen, Holt, & Bauer, 2014). For wet rocks consolidation can be misinterpreted as creep since this is also a time dependent effect. These effects can be observed both in the lab and the field, but the timescale can be very different (Fjær, Larsen, Holt, & Bauer, 2014). In the field creep can occur over geological time, but for experiments in the lab the duration of observation is much shorter.

Strain rates are time dependent, and are divided into three different stages, which can be seen in Figure 2-1. The first is the primary stage, where the strain rate decreases as a function of time before the rate approaches a constant value. The second stage of creep is reached when the rates of recovery and work hardening become equal (Charit & Murty, 2008), which means that the deformation rate is constant during this stage. The last stage of creep is called tertiary or accelerated creep, where the deformation rate increases as a function of time until the failure limit of the rock is reached, and the sample breaks. The creep rate is highly dependent of stress and temperature. The creep rate increases both for increasing stress and generally also for increasing temperatures. If stress is removed during primary creep, the strain will recover and approach zero. If stress is removed during the secondary or tertiary the strain will recover to a non-zero value, where residual strain has caused permanent deformation (Jaeger, Cook, & Zimmerman, 2007).

In brittle rocks, time-dependent deformation is primarily controlled by sub-critical crack growth. Flaws, defects, voids and other small cracks have a tendency to grow slowly when the stresses are less than the material strength or the stress intensity factor is less than the fracture toughness. Sub-critical crack growth is typically caused by stress and chemical corrosion (Shen & Rinne, 2007). Traditionally, time-dependency in rocks has been modelled by the principles of continuum and damage mechanics. However, when the instability of the rock mass is dominated by explicit fracturing, it is more realistic to use theories of fracture mechanics and sub-critical crack growth to predict its time dependent behavior. (Shen & Rinne, 2007)
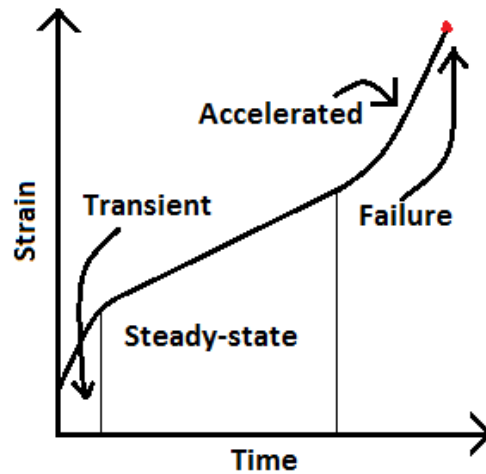
Figure 2-1 The three different stages of creep; transient, steady state and accelerated creep.

2.1.1   The different stages of creep

The first stage of creep is called transient creep, due to the fact the deformation rate decays with time. If the stress applied is low, the deformation rate will converge to zero and creep will approach a final value, as indicated for the lower case in Figure 2-2. This means that the two final stages of creep will not occur. In the transient period the mechanism causing creep is the creation of stable microfractures spreading at a decaying rate (Fjær, Holt, Horsrud, Raaen, & Risnes, Petroleum Related Rock Mechanics 2nd edt., 2008). According to Günther, Salzer, & Popp (2010) the processes controlling primary creep are dislocations between the grains which start to move when stress increases. With increasing deformation, the motion capability of present dislocations diminishes. If deformation continues, new dislocations will be formed, resulting in increased dislocation density. In turn this process causes increased resistance to deformation, maintaining a constant deformation rate. This material hardening which increases proportionally with deformation is counteracted by the recovery of dislocations (Günther, Salzer, & Popp, 2010). If the stress applied rock is removed, the rock will expand to its original size and the deformation will disappear and approach zero (Fjær, Holt, Horsrud, Raaen, & Risnes, Petroleum Related Rock Mechanics 2nd edt., 2008).

If the applied stress or temperature is sufficiently high, the transient creep stage will be followed by a steady state stage, where the deformation rate will stabilize and approach final value. The strain rate stabilizes because the formation rate becomes equal to the annihilation rate of the

4

dislocations (Günther, Salzer, & Popp, 2010). If the applied stress is reduced during the steady state stage, the deformation originating from this phase will not recover.

If stress is maintained for a long enough time and the stress (and/or temperature) is sufficiently high, the deformation will go into the final stage called accelerating creep. The deformation rate increases exponentially as unstable microfractures spreads at a rapid rate, and the rock eventually fails.

The principles discussed above are illustrated in Figure 2-2, where three different loads are applied to a rock and the creep characteristics change accordingly.
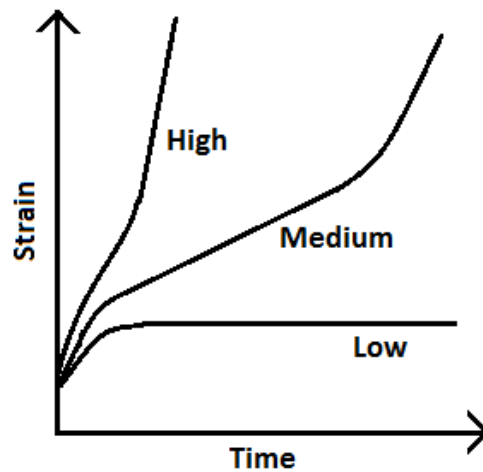
Figure 2-2 Creep response for different applied stresses

2.1.2 Internal processes causing creep

Grain scale processes in quartz rich minerals include brittle behavior, frictional mechanisms of intergranular slip, grain rearrangement, pore collapse, micro fractures, grain crushing and time and temperature dependent mechanisms of subcritical crack growth (Chester, Lenz, Chester, & Lang, 2004).

Shen & Rinne (2007) claim time dependency in brittle rocks is dominated by sub-critical crack growth. Classical fracture mechanics propose that a fracture tip with stress intensity equal K_{Ic}, will propagate at velocities close to the rocks elastic wave speed. During long term loading cracks can propagate at stress intensities lower than K_{Ic} (Shen & Rinne, 2007). This is known as sub-critical crack growth. The process happens at velocities depending on stress intensity in the tip of the crack, and can be many orders of magnitude lower than growth velocity at critical stress intensities (Shen & Rinne, 2007).

Crack propagation has been subject to many studies over the last decades. Among them is Atkinson's (1982) description of crack growth caused by tensile stress, referred to as mode I. He identified four key micro-mechanisms that explain the propagation of cracks leading fracture after minor plastic flow and fractures forming after large strains.

The first mechanism is propagation of pre-existing cracks. A crack or flaw in a brittle rock can propagate at stresses lower than what is required for slip in any crystallographic system. Fracturing can occur at the stress σ_f, given by (Atkinson, 1982):

$$\sigma_f \cong \left(\frac{E G_c}{\pi c}\right)^{1/2} \qquad\qquad 2\text{-}1$$

where E is Young's modulus and, 2c is the length of the pre-existing crack, G_c is the critical strain energy release rate ($G_c = K_I{}^2(1 - v^2)/E$, v: poisson's ratio) and K_I is the tensile stress intensity factor.

The second mechanism is fracturing controlled by cracks generated from micro-plasticity. If there are no cracks in the rock, or the cracks are very small, the stress can build up to levels required to initiate slip (Atkinson, 1982). This occurs when stress pile up along grain boundaries, and crack

lengths are proportional to the grain size, d, since this is the wavelength of the internal stress. If stresses exceed σ*, given as:

$$\sigma^* \cong \left(\frac{E G_c}{\pi d}\right)^{1/2} \qquad\qquad 2\text{-}2$$

a crack will propagate as soon as it is formed and fracture will occur at the stress for the onset of micro plasticity, σ_y. However if the stress acting along the grain boundary is within the range $[\sigma_y < \sigma < \sigma^*]$, the crack will form, but it will not propagate before the stress is increased. (Atkinson, 1982; Olsen, 2014)

The third mechanism is fractures controlled by cracks generated through general plasticity/grain boundary sliding. Large deformation through plastic strain is causing this type of fractures and is caused by increasing temperatures that decreases the flow stress, which leads to plastic flow and creep. Plasticity makes pre-existing faults less sharp and increases the resistance to fracture, G_c (Atkinson, 1982).

The last fracture propagation mechanism is intergranular creep fracture. This occurs under low stresses and high temperatures. Void- and wedge-cracks nucleate and grow on grain boundaries. "Nucleation[1] is probably controlled by dislocation creep, but when cracks are small growth is occurring by diffusion; the rate of diffusion being controlled by dislocation creep in the surrounding grains" (Atkinson, 1982).

If sudden sliding or new cracks are opened quickly, acoustic waves will propagate through the rock. These acoustic occurrences are called acoustic emissions (AE) and have been studied widely (Bart, Kenter, & Munster, 2001; Heap, 2009). Heap (2009) stated that AE output is a reliable proxy for crack growth within a sample. He also found that new micro crack damage, in general, is generated once the previous maximum stress has been exceeded during cyclic stressing. This effect is called the Kaiser "stress-memory" effect, which states that the onset of AE does not occur before the previously held peak stress is exceeded (Holt, Pestman, & Kenter, 2001).

---

[1] Crack nucleation is the initial process where sufficient quantity of dislocations accumulates to allow separation of crystal planes (Physics forum, 2009).

The microscopic changes in the structure, causing creep also lead to changes in the elastic moduli of the rock. As an effect of creep Shear modulus and Young's modulus are reduced, the Poisson ratio increased and while bulk modulus remains unaffected (Fjær, Holt, Horsrud, Raaen, & Risnes, Petroleum Related Rock Mechanics 2nd edt., 2008).

2.2 Acoustics

2.2.1 P-waves

P-waves are compressional waves where the displacement of the medium the wave is travelling through moves parallel to the direction of the wave. Figure 2-3 shows how a compressional pulse travels through an elastic substance, three different times. The pulse compresses an area of the medium before it propagates forward. When the wave has passed the previously compressed area in the medium the substance returns to its original state and is decompressed, as seen in Figure 2-3.

The velocity of a P-wave is depending on the uniaxial compaction modulus (H) and the density (ρ). This can be derived by combining Newton's second law of motion in with Hook's law and solving for displacement parallel to the wave in one direction[2]. The relation between the P-wave velocity and the elastic moduli and the density is:

$$v_P = \sqrt{\frac{H}{\rho}} = \sqrt{\frac{K + \frac{4}{3}G}{\rho}}, \qquad \text{2-3}$$

where K is Bulk modulus and G is shear modulus. This expression can be re-written and as a function of Young's modulus (E) and Poisson's ratio (v), by using elastic moduli relations:

$$v_P = \sqrt{\frac{E}{\rho} \frac{(1-v)}{(1-2v)(1+v)}}, \qquad \text{2-4}$$

It should be noted that the moduli given in equation 2-3 and 2-4 are the dynamic moduli, which can deviate significantly from the static moduli. This will be explained in chapter 2.2.3.

---

[2] The derivation is not included in the thesis, but can be found in Fjær et al. (2008)
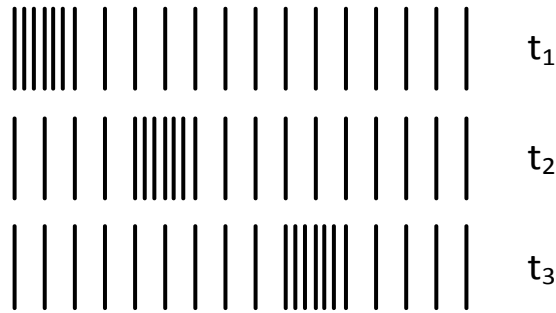
Figure 2-3 A compressional pulse at 3 different times, propagating from left to right

2.2.2 P-waves in porous materials

P-wave velocities in sandstones and other porous mediums are depending on the stress applied to the medium. The cause of this is believed to be the change in the number and size of cracks sensitive to stress (Fjær E. , 2006). Sandstone naturally contains small cracks in arbitrary directions. When stress is applied, cracks aligned normal to the direction of the stress will tend to close when a sufficiently high stress is applied, as illustrated in Figure 2-4.

Micro cracking is part of the processes causing creep, and cracks cause the P-wave velocity to decrease. Thus it is natural to think that the wave velocities will change as a result of micro cracking active in these processes. This was confirmed by Fjær (2006) by monitoring the strain and P-wave velocity over a period of time, holding the stress constant. The P-wave velocity was found to decrease as the strain increases.

The explanation of this is believed to be linked to an increase in the crack density as a result of one (or more) of the processes mentioned in chapter 2.1.2 becoming active. The increase in crack density leads to a decrease in the effective Young's Modulus since no stress can be transferred over the cracks. The reduction in effective Young's Modulus follows the relation (Fjær, Holt, Horsrud, Raaen, & Risnes, Petroleum Related Rock Mechanics 2nd edt., 2008):

$$E_{eff} = E(1 - \xi Q) = \frac{\sigma_z}{\varepsilon_z}, \qquad\qquad 2\text{-}5$$

where ξ is the crack density and Q is a coefficient depending on the shape and orientation of the crack. Consider a block equal to the one in Figure 2-4 containing only one crack. As stress is applied and σ_z approaches σ_c the cracks closes and $\xi \rightarrow 0$ and also implying that $E_{eff} \rightarrow 0$. The plot on the right in Figure 2-4 could show the stress-strain relationship for a real sandstone.
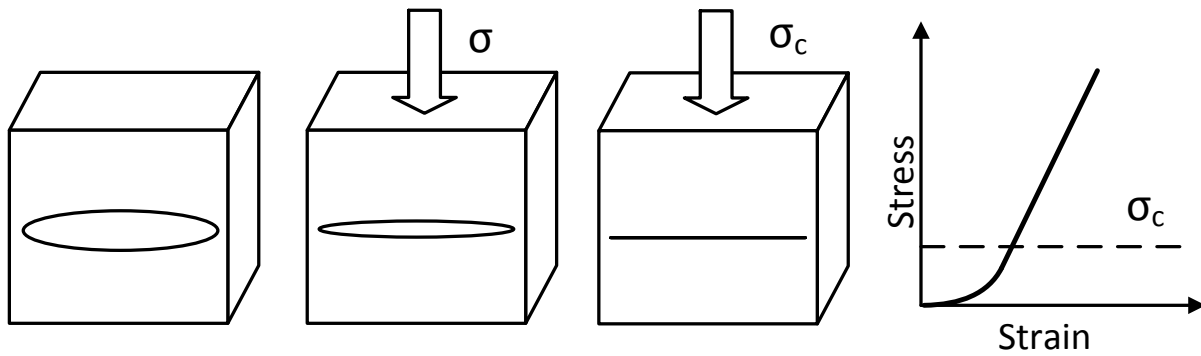
Figure 2-4 Left: A crack closing under increasing stress Right: Non-linear deformation in the start caused by several cracks closing. The non-linear part in the start is caused by the several cracks closing, and the critical stress σ_c is the point where all the perpendicular cracks are closed. A study confirmed that non-linear behavior is mainly caused by the structure of the rock itself rather than pore fluids (Stroisz & Fjær, 2011).

In a study of core damage effects on compaction behavior Holt et al. (1994) found that sound velocities decrease permanently as a result of an unloading-reloading cycle. They also claim that velocities decrease during unloading. The reason the velocity is decreasing during unloading is that cracks reopen or that grain bonds breaks. When the rock is reloaded to the forming stress state, the sound velocity does not recover to the initial values. The reason for this permanent drop is local displacements that prohibit complete closure of opened cracks and broken bonds, leading to higher crack density (Holt, Brignoli, Fjær, Unander, & Kenter, 1994).

2.2.3 Static and dynamic moduli

Sound velocities depend on elastic modulus which describes a material's ability to resist deformation occurring due to change in external stresses (Fjær E. , 1999; Olsen, 2014). Equation 2-4 shows that P-wave velocity depends explicitly on elastic moduli, which also implies that it depends on cracks and crack densities, as shown in equation 2-5. This means that the moduli found from sound velocities; the dynamic moduli, should be equal to the moduli found from traditional stress vs. strain tests; the static moduli. However this does not fit the wide range of observations from experiments where the static moduli deviate significantly from the dynamic moduli (Fjær, Holt, Horsrud, Raaen, & Risnes, Petroleum Related Rock Mechanics 2nd edt., 2008).

Static moduli describe a substance's response to strain rates normally smaller than 10^{-2} s^{-1} with large amplitudes. Dynamic moduli on the other hand are measures of materials response to rapid

10

stress oscillations where the strain rate is typically $1\text{-}10^{-4}$ s^{-1} and the amplitude is small (Fjær E. , 1999; Olsen, 2014). This means that the strain amplitude is the most significant difference between the measurements of static and dynamic moduli. Repeated unloading-reloading cycles for static tests have however shown to be similar to the dynamic test results. Plona and Cook (1995) found that the elastic moduli derived from the slope of a stress vs. strain curve during such cycles approach the moduli derived from velocity measurements when the amplitude of the cycles becomes sufficiently small (Fjær, Holt, Horsrud, Raaen, & Risnes, Petroleum Related Rock Mechanics 2nd edt., 2008).

The amplitude is important for the behavior of the rocks since small amplitude dynamic oscillations are unable to overcome the static friction needed to close a crack. The difference of the static and dynamic moduli in porous rocks can deviate significantly, especially for lower stresses. According to Montmayeur & Graves (1986) microcracks are the key to the relationship of dynamic-static properties:

> Measured static properties are affected by the presence of microcracks. In Montmayeurs and Graves (1985) research, microcracks close under high confining pressures (270bars) and the rock behave as if it were untracked. As confining pressures increase and micro cracks close, the difference between dynamic/static values can be corrected using Biot's theory.

Consequently the difference between the two moduli is decreasing as the confinement stress increases, and the difference is also less for well cemented, strong sandstones than for weak ones (King, 1969; Fjær, Holt, Horsrud, Raaen, & Risnes, Petroleum Related Rock Mechanics 2nd edt., 2008). Further it is worth noting that the static and dynamic moduli are equal for homogeneous, elastic materials like steel, which is not the case for inhomogeneous rocks. Thus the source of the discrepancy is likely to be linked to the heterogeneous microstructure of the rocks. The effect caused by the heterogeneities is further expected to be linked to local stress concentrations at the grain boundaries exceeding the elastic limit of the material. Fjær (1999) formulated relations between the static and dynamic moduli based on observation from experiments on weak sandstone (Fjær, Holt, Horsrud, Raaen, & Risnes, Petroleum Related Rock Mechanics 2nd edt., 2008):

$$E = \frac{E_e}{1 + P_z E_e}(1 - F) , \qquad\qquad \text{2-6}$$

$$K = \frac{K_e}{1 + 3PK_e} , \qquad\qquad \text{2-7}$$

The subscript e is the notation for the dynamic moduli; P is a measure for the non-elastic compliance[3] due to normal loading a process which involves crushing of asperities at the grain contacts. F is a measure of the additional non-elastic deformation caused by shear loading (Fjær, Larsen, Holt, & Bauer, 2014; Olsen, 2014). F is believed to be proportional to the density of sliding cracks (Fjær E. , 1999) and will be further explained in chapter 2.3.2.

The discrepancy between static and dynamic moduli in weak rocks can be interpreted as a series of local failure processes on a microscopic scale occurring during the entire loading sequence (Fjær, Holt, Horsrud, Raaen, & Risnes, Petroleum Related Rock Mechanics 2nd edt., 2008, p. 194).

---

[3] Compliance: The inverse of stiffness

2.3 Creep models

2.3.1 Burgers model

Rheological models can be used to describe the macroscopic creep effects. The models are based on combinations of springs, plastic sliders and dashpots. They are placed in series or parallel and the characteristics of the elements are changed to best match the viscoelastic and elasto-viscoplastic behavior (Maranini & Brignoli, 1999). Viscoelasticity means that the material has both elastic and viscous properties. These types of models are simple and does not account for normal stress, shear stress, temperature and intrinsic structure. The elasto-viscoplastic substance shows time dependent behavior in which the deviatoric stress give rise to viscous behavior, or plastic behavior if the instantaneous elastic strength of the material is temporarily exceeded (Hudson & Harrison, 2000, s. 214; Olsen, 2014).

The two most common material models used to represent a viscoelastic material are the Maxwell-material (elstoviscous) and the Kelvin-Voigt-material (viscoelastic).Figure 2-5 shows the Maxwell-element, which consist of a spring and a dashpot in series. The dash-pot will absorb more and more strain as time passes, while the strain of the spring remain constant as long as the force is not changed. The dashpot consists of a viscous container and a piston arm with room for the fluid to pass through to the other side. The fluid flows from one side of the piston to the other as a function of time. Hence the strain absorbed by this element is time dependent and increases with time. The Maxwell model the strain is given by equation 2-8 (Kristensen, 2013):

$$\varepsilon = \frac{\sigma_{spring}}{E},$$

2-8

where ε is the strain, σ_{spring} is the stress absorbed by the spring and E is the spring characteristics, an analogue to Young's modulus in rock mechanics.
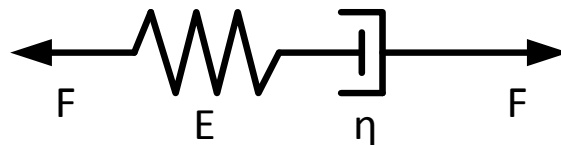
Figure 2-5 The Maxwell-element

The strain absorbed by the dashpot is time-dependent and follow the relation in equation 2-9:

$$\dot{\varepsilon}_{dashpot} = \frac{\sigma_{dashpot}}{\eta} \quad,$$

2-9

where $\dot{\varepsilon}_{dashpot}$ is the strain rate in the dashpot, $\sigma_{dashpot}$ is the stress acting on the dashpot and η is the material coefficient of viscosity.

Assuming the total strain of the Maxwell model is the combined strain of the dashpot and the spring, adding equation 2-8 and 2-9 gives the following:

$$\dot{\varepsilon}_{total} = \dot{\varepsilon}_{spring} + \dot{\varepsilon}_{dashpot} = \frac{\sigma_{dashpot}}{\eta} + \frac{1}{E}\dot{\sigma}_{spring} \, ,$$

2-10

where $\dot{\sigma}_{spring}$ is the derivative of equation 2-8 with respect to time. Integration of the equation 2-10 yields:

$$\int d\varepsilon = \frac{1}{E}\int \frac{d\sigma}{dt}dt + \frac{\sigma}{\eta}\int dt \xrightarrow{yields} \varepsilon = \frac{\sigma}{E} + \frac{\sigma}{\eta}t + C$$

2-11

$$,$$

given that the strain rate is non-zero. Also assuming the material behaves elastic at t = 0 ($\varepsilon_0 = \sigma_0/E$), C = 0.

If the stress is increased instantaneously before the strain is held constant and the strain rate ($\dot{\varepsilon}$) is zero, the relaxation for the stress absorbed by the spring would be:

$$\int \frac{1}{\sigma}d\sigma = -\frac{E}{\eta}\int dt \xrightarrow{yields} \sigma = \sigma_0 e^{-\frac{E}{\eta}(t-t_1)} \, ,$$

2-12

given that t=t_1 (time when $\dot{\varepsilon} \to 0$) and $\sigma = \sigma_0$ yields C = ln(σ) + (E/ η)t_1. This means that the stress within the material will decrease when the strain rate approaches zero, and relaxation will be non-linear (Hudson & Harrison, 2000). The reason for the relaxation is that the dashpot takes up strain from the spring.

The Kelvin-Voigt model illustrated in Figure 2-6 is another model used to describe the rheology of a material. It consists of the same elements as the Maxwell-element, but the two elements are set in parallel instead of series, giving the material different properties.
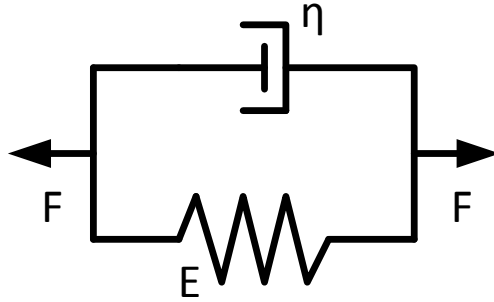
14

Figure 2-6 The Kelvin-Voigt element

In the time right after a force is applied to the system in Figure 2-6 the dashpot absorbs most of the stress. As the piston in the dashpot is pulled through the cylinder the spring is also extended. This means that the stress absorbed by the spring increases with time. The strain development of the Kelvin-Voigt model is also different from the Maxwell model. For the Kelvin-Voigt model the strain increases simultaneously in both elements as a function of time. The strain in the Maxwell model is instant in the spring and time dependent for the dashpot.

The Kelvin Voigt model can be explained mathematically by rearranging equation 2-8 and 2-9 isolating the stress on one side and adding the stresses together, yielding:

$$\sigma_{total} = \sigma_{spring} + \sigma_{dashpot} = E\varepsilon + \eta\dot{\varepsilon} \qquad \text{2-13}$$

If the stress is assumed to be constant (σ_0) for the entire period the differential equation 2-14 would describe the deformation rate:

$$\frac{d\varepsilon}{dt} = \frac{\sigma_0 + E\varepsilon}{\eta} \qquad \text{2-14}$$

If equation 2-14 is rearranged and integrated the solution would be:

$$\frac{1}{\eta}\int dt = \int \frac{d\varepsilon}{\sigma_0 - E\epsilon} \xrightarrow{yields} \varepsilon = \frac{\sigma_0}{E}\left(1 - e^{-\frac{E}{\eta}t}\right), \qquad \text{2-15}$$

since $\varepsilon = 0$ at t = 0, giving C = (1/E)ln(σ_0) (Hudson & Harrison, 2000). Equation 2-15 states that the deformation for the Kelvin-Voigt substance is non-linear.

If the Maxwell and Kelvin-Voigt substances are combined in a series, the composed substance is called Burgers substance and is illustrated in Figure 2-7. This model can describe the instantaneous strain, transient creep and steady state creep, for both loading and unloading (Fjær, Holt, Horsrud, Raaen, & Risnes, Petroleum Related Rock Mechanics 2nd edt., 2008).

Figure 2-8 shows how the Burger substance responds to instant loading to a constant stress as well as instant unloading back to zero. The stress σ_0 is applied to the Burger's substance from $0 < t < t_c$. From $t > t_c$ the stress is removed and the strain recovery follows in opposite order as loading. Another difference from the loading phase is that the steady-state deformation is permanent and leaving a non-recoverable deformation. Deformation in the Burger's substance can be represented mathematically by a set of equations given by presented by Fjær et al. (2008):

$$\varepsilon = \begin{cases} 0 & for\ t < 0 \\ \dfrac{\sigma_0}{E_2} + \dfrac{\sigma_0}{E_1}\left(1 - e^{-t/t_1}\right) + \dfrac{\sigma_0}{\eta_2}t & for\ 0 < t < t_c \\ \dfrac{\sigma_0}{E_1}\left(e^{t_c/t_1} - 1\right)e^{-t/t_1} + \dfrac{\sigma_0}{\eta_2}t_c & for\ t > t_c \end{cases} \qquad \text{2-16}$$

where $t_1 = \eta_1/E_1$. The derivation of the equation can be found in Appendix I.
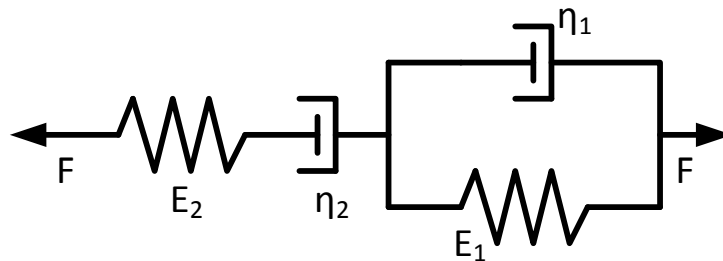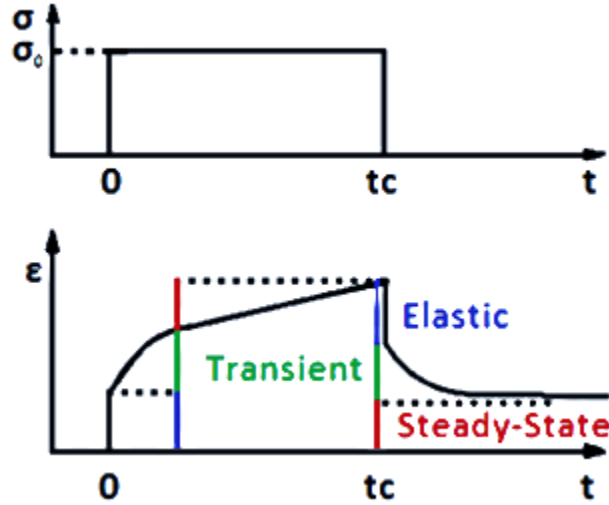

Figure 2-7 The burgers substance

Figure 2-8 Strain response in a Burger's substance

2.3.1.1 Finite difference method

The Burgers model consists of two simple differential equations based on the Maxwell and Kelvin-Voigt models. In order to solve the Burgers equations analytically, two equations are solved separately and the solutions are added. If a finite difference method is used, the solution can be approximated for the entire equation.

The two basic models used in the Burgers model are discretized using backward difference in order to give the two following expressions:

$$\dot{\varepsilon}_{Maxwell} = \frac{\sigma}{\eta_2} + \frac{1}{E_2}\dot{\sigma} \xrightarrow{yields} \frac{\varepsilon_{M,i} - \varepsilon_{M,i-1}}{\Delta t} = \frac{\sigma_i}{\eta_2} + \frac{1}{E_2}\frac{\sigma_i - \sigma_{i-1}}{\Delta t}, \qquad 2\text{-}17$$

rearranging gives the Maxwell part:

$$\varepsilon_{M,i} = \varepsilon_{M,i-1} + \frac{\sigma_i}{\eta_2}\Delta t + \frac{\sigma_i - \sigma_{i-1}}{E_2}, \qquad 2\text{-}18$$

$$\sigma = E_1\varepsilon_{K-V} + \eta_1\dot{\varepsilon}_{K-V} \xrightarrow{yields} \sigma_i = E_1\varepsilon_{K-V.i} + \eta_1\frac{\varepsilon_{K-V.i} - \varepsilon_{K-V.i-1}}{\Delta t} \qquad 2\text{-}19$$

rearranging gives the Kelvin-Voigt part:

$$\varepsilon_{K-V.i} = \frac{\sigma_i + \eta_1 \frac{\varepsilon_{K-V.i-1}}{\Delta t}}{\frac{\eta_1}{\Delta t} + E_1} \qquad \text{2-20}$$

Equation 2-18 and 2-20 are inserted into two different columns in Excel and are added to one model. Further on the squared difference between the model and the LVDT data is found and minimized using the built-in Solver function, changing the four parameters (E_1, E_2, η_1, η_2) in the equations above. The process described is sketched in Figure 2-9.

2.3.1.2 Boltzmann Superposition Principle

The simple Burgers model can describe the concept in Figure 2-8 using the same boundary conditions as used for the derivation of equation 2-16 in Appendix I. This is the basic model for that specific stress path. This does not cover the stress path used for several of the experiments where the stress path is changed from a non-zero value to another non-zero value. To cope with this issue the Boltzmann Superposition Principle can be used, breaking up the stress path in several increments. The Boltzmann superposition principle states that a materials response to a given stress is independent of the stress already applied to the material, which gives the following expression (University of Minnesota, 2000):

$$\varepsilon(t) = P(t - t_{c1})\sigma_1 + P(t - t_{c2})(\sigma_2 - \sigma_1) + \cdots + P(t - t_{ci})(\sigma_i - \sigma_{i-1}), \qquad \text{2-21}$$
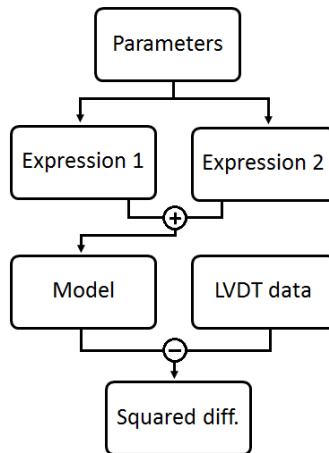

Figure 2-9 Sketch of the fitting process

giving the general form for discrete changes (Tropea, Yarin, & Foss, 2007, p. 627; University of Nottingham):

$$\varepsilon(t) = \sum_i \varepsilon_i = \sum_i P(t - t_{ci})\Delta\sigma_i,$$

2-22

where $P(t)$ is the time dependent compliance of the rock and t_{ci} is the time where the stress is changed. This expression can model the stress path and strain curves found in Figure 2-10. It is achieved using the three terms of "compliance" from the burgers equation yielding:

$$\varepsilon_{i+} = \sum_{i=0} \frac{\Delta\sigma_i}{E_2} + \frac{\Delta\sigma_i}{E_1}\left(1 - e^{-(t-t_{ci})/t_1}\right) + \frac{\Delta\sigma_i}{\eta_2}(t - t_{ci}) \quad,$$

2-23

Equation 2-23 is one of the addend in the sum of equation 2-22.

Equation 2-23 can only model the stress path given in Figure 2-10. This means another term is needed to model the decreases in stress applied during the experiments. Equation 2-16 consists of two parts, one for the increases in stress and one for decreases in stress. By applying the Boltzmann Superposition principle to the term for $t > tc$ we obtain:

$$\varepsilon_- = \sum_{i=0} \frac{\sigma_i}{E_1}\left(e^{t_{ci}/t_1} - 1\right)e^{-t_i/t_1} + \frac{\sigma_0}{\eta_2}t_{ci}$$
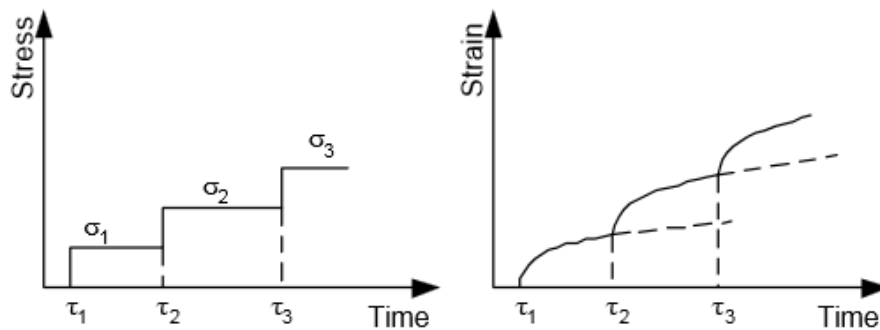
2-24

Figure 2-10 Stress and strain curves using the Boltzmann superposition principle

(University of Minnesota, 2000).

19

The stress increments given in Figure 2-11 are interested into equation 2-23 for the duration of a stress step, from $t_{c,i-1}$ to $t_{c,i}$. When stress step is removed, the same size increment is inserted into equation 2-24. When the interval for the positive stress increment ends the negative begins. For $\Delta\sigma6$ this means that the strain increment is:

$$\varepsilon_3 = \varepsilon_{3+} + \varepsilon_{3-} \qquad\qquad 2\text{-}25$$

where ε_{3+} is:

$$\varepsilon_{3+} = \frac{\Delta\sigma_6}{E_2} + \frac{\Delta\sigma_6}{E_1}\left(1 - e^{-(t-t_{c1})/t_1}\right) + \frac{\Delta\sigma_6}{\eta_2}(t - t_{c1}) \qquad from\ t_{c1} < t < t_{c2} \qquad 2\text{-}26$$

and ε_{3-} is:

$$\varepsilon_{3-} = \frac{\Delta\sigma_6}{E_1}\left(e^{t_{c2}/t_1} - 1\right)e^{-t/t_1} + \frac{\Delta\sigma_6}{\eta_2}t_{c2} \qquad from\ t_{c2} < t < t_{c7} \qquad 2\text{-}27$$

The same equations are applied to all the strain increments which in sum give the total strain curve. This gives the stress and strain curves for a 6 step experiment which can be seen in Figure 2-11 and Figure 2-12. In Figure 2-12 the red line is the sum of all the strain steps. The curve is bending upwards after the first unloading steps because the contribution from the loading of the previous steps ($\Delta\sigma_{i-1}$) is greater than the effect of the unloading step ($\Delta\sigma_i$).
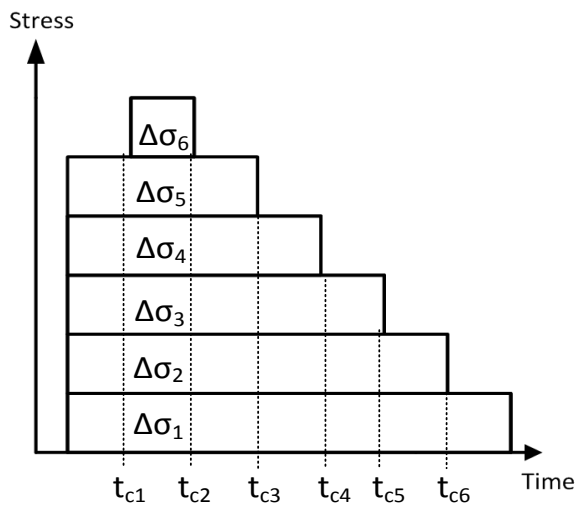

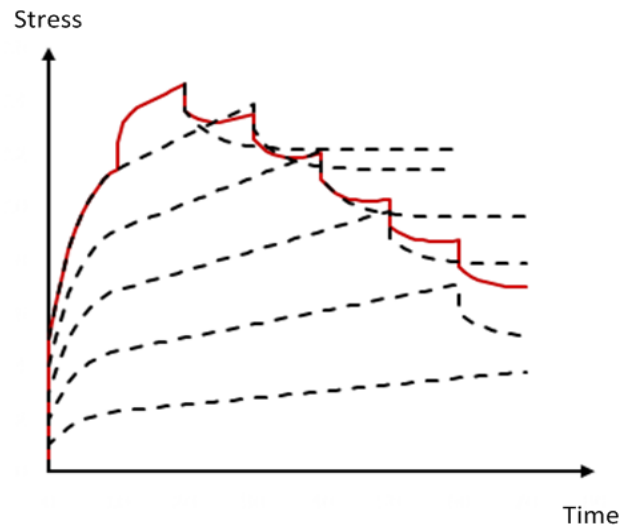
Figure 2-11 Stress path of added stress increments

Figure 2-12 Strain of added strain increments

2.3.2 The FORMEL model application in creep modelling

The early work on the FORMEL model was first published in 1996 as project to determine the *in situ* mechanical properties from logs. The idea was based on describing the internal processes occurring in rocks during mechanical loading (Raaen, Hovem, Jøranson, & Fjær, 1996). Further work was performed relating static and dynamic mechanical properties of weak sandstones (Fjær E. , 1999). This model was further developed by Fjær et al. (2014) and uses the principles of the FORMEL model to describe the time delayed deformation.

The model uses the relationship between the static and dynamic Young's and Bulk modulus described in Equation 2-6 and 2-7 (Fjær E. , 1999). According to Fjær et al. (2014) the F-parameter is depending on the shear strain and the stress level according to Equation 2-28 (Fjær E. , 1999):

$$F = A \frac{\varepsilon_z - \varepsilon_r - \varepsilon_0}{\sqrt{\sigma_z + \sigma_r + S}}, \qquad \text{2-28}$$

where A and S is material dependent constants and ε_0 is the shear strain at the start of axial loading. The F-parameter is associated with local failure caused by shear stress, e.g. friction controlled slip along crack surfaces, which is the source of creep in the model (Fjær, Larsen, Holt, & Bauer, 2014). According to Hook's law a step increase in axial stress ($\Delta\sigma_z$) leads to an instantaneous strain ($\Delta\varepsilon_z$), following Equation 2-29:

$$\Delta\varepsilon_z = \frac{\Delta\sigma_z}{E} \qquad \text{2-29}$$

The increase in stress also causes the F-parameter to increase due to the fact that the axial strain increases to $\varepsilon_z \rightarrow \varepsilon_{z,0} + \Delta\varepsilon_z$. In turn this leads to a decrease in Yong's modulus, following Equation 2-6, which induces an additional increase in ε_z. Consequently setting off another full cycle, which repeats until $\frac{d\varepsilon_z}{dt} \rightarrow 0$ or the sample breaks, where each cycle is completed according to the characteristic time τ. For low stress levels where F is significantly less than 1, the chain of cycles will converge to a finite strain. If stress levels are increased to high values where F is close to 1 the series will diverge and the strain rate will increase to the point where $E \rightarrow 0$ (Fjær E. , 1999). From this point the strain rate increases and quickly leads to failure. Strain-time relationship is given by Equation 2-30 and describes the axial strain induced by a step increase in the axial stress (Fjær, Larsen, Holt, & Bauer, 2014):

$$\frac{d^2\varepsilon_z}{dt^2} + \frac{1}{\tau}\left[1 - \frac{\Delta\sigma_z}{(1-q\varepsilon_z)^2}\frac{q}{E^*}\right]\frac{d\varepsilon_z}{dt} = 0,$$

2-30

where

$$E^* = \frac{E_e}{1 + PE_e}$$

2-31

$$q = A\frac{(1+v)}{\sqrt{\sigma_z + \sigma_r + S}}$$

2-32

$$(1+v)\varepsilon_z = \varepsilon_z - \varepsilon_r$$

2-33

where, E*, v, and q are assumed to be constants.

The creep characteristics are depending on the factor in the brackets [...] in equation 2-30. If this factor remains positive up until the strain rate approaches zero the total strain will converge to a final value. On the other hand, if the factor [...] turns negative before the strain rate approaches zero, the deformation will accelerate towards failure. The parameter controlling the sign of the bracket is the axial strain and if ε_z becomes sufficiently large the value of the bracket turns negative (Fjær, Larsen, Holt, & Bauer, 2014).

Fjær et al. (2014) argues that the local failure events related to the F-parameter may be associated with activation of cracks. This means that an increase in the F-parameter might be connected with crack growth or creation of new cracks (Fjær, Larsen, Holt, & Bauer, 2014). As mentioned earlier the F-parameter is depending on the local shear stress, which gives rise to activation of cracks. Global shear stress leads to locally induced shear stress that can cause crack activation. Creation or extension of cracks leads to deformation that causes the total load to redistribute and local stresses that caused crack activation is directed to intact parts of the rock. This means that new cracks can develop in the area where the shear stress is shifted to (Fjær, Larsen, Holt, & Bauer, 2014). If the number of cracks forming each cycle declines as a function of time, the process is sub-critical and will process will eventually stop. The internal processes in the rock described, is the key feature that the model is trying to predict with the series of cycles, either converging to finite strain level or diverging to failure. However it does not describe this explicitly (Fjær, Larsen, Holt, & Bauer, 2014).

The characteristic creep time in the FORMEL model, τ, is also believed to be a function of the strain contribution from each cycle. The extended model is believed to follow the relation:

$$\frac{d^2\varepsilon_z}{dt^2} + \frac{1}{\tau^2}\left[1 - \left(\frac{\Delta\sigma_z}{(1-q\varepsilon_z)^2}\frac{q}{E^*}\right)^{1+n}\right]\left(\tau\frac{d\varepsilon_z}{dt}\right)^{\frac{1+2n}{1+n}} = 0,$$ 2-34

where n is the parameter controlling the strain contribution from each cycle. For n = 0 equation 2-30 is equal to equation 2-34.

On discrete form the equation becomes:

$$\varepsilon_z^{i+2} = \varepsilon_z^{i+1} + \left(\varepsilon_z^{i+1} - \varepsilon_z^i\right)\left[1 + \left(\frac{\Delta t}{\tau}\right)^{\frac{1}{1+n}}\left[\left(\frac{\Delta\sigma_z}{\left(1-q\varepsilon_z^i\right)^2}\frac{q}{E^*}\right)^{1+n} - 1\right]\left(\varepsilon_z^{i+1} - \varepsilon_z^i\right)^{\frac{n}{1+n}}\right],$$ 2-35

3 Equipment and methods

3.1 Experiment setup

The experiments are conducted on an electromechanical load frame from MTS. It is capable of applying loads up to 10,000 Newton. This means the maximum possible stress applied to the cores are 9.48 MPa and 20.37 MPa for 25.00 mm and 36.65 mm core diameter respectively. The original plan was to use cores with a diameter of 36.65 mm for both Castlegate and Saltwash South. However, since the UCS of Castlegate is around 17.00 MPa the 10kN frame is not able to apply the required load for samples of 36.65 mm diameter size. Consequently the Castlegate cores had to be cut out in 25.00 mm.

The load frame has a rectangular shape and includes a base unit and two vertical columns. The two columns are supported by a fixed upper transverse. The moving crosshead is driven by ball screws on the load frame. The crosshead is coupled to the ball screws with high-strength, ball nuts and rides on the ball bearings (MTS Systems Corporation, No Date). A piston is mounted at the base of the frame indicated in Figure 3-1. The counterpart of the piston is mounted at the bottom of the crossbeam which is lowered by the ball screws inside the column. A close up of the two pistons can be seen in Figure 3-2.

The frame is connected to a digital indicator display, which shows the load (N) applied and the crosshead position. The frame is also connected to a computer that controls and records data from the frame, through the software TestWorks. The procedure for the experiment is written in the software and the recorded data is displayed during the test. The desired stress levels and times are defined and the frame automatically compensates as the sample deforms, by changing the position of the ball screws.

The core is placed between two pistons, made of steel, seen in Figure 3-2. In this setup, three linear variable differential transformers (LVDT) are mounted around the pistons, with 120 degrees spacing. Within the pistons there is an acoustic transmitter and receiver connected to an amplifier and data logger. A plastic sleeve was put around the core to support the core is case it collapsed.
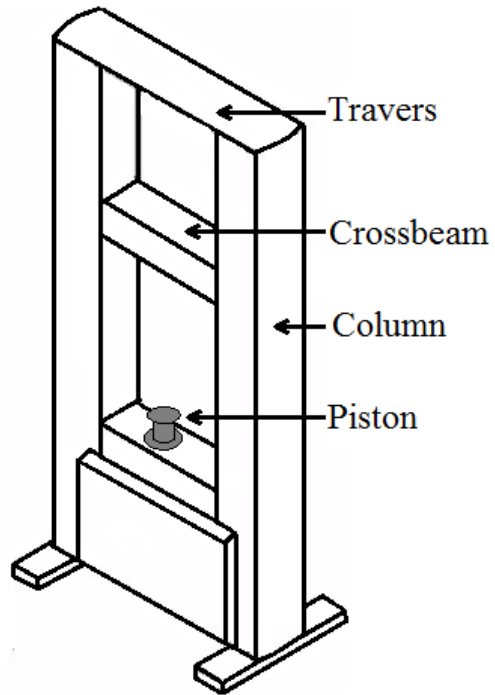
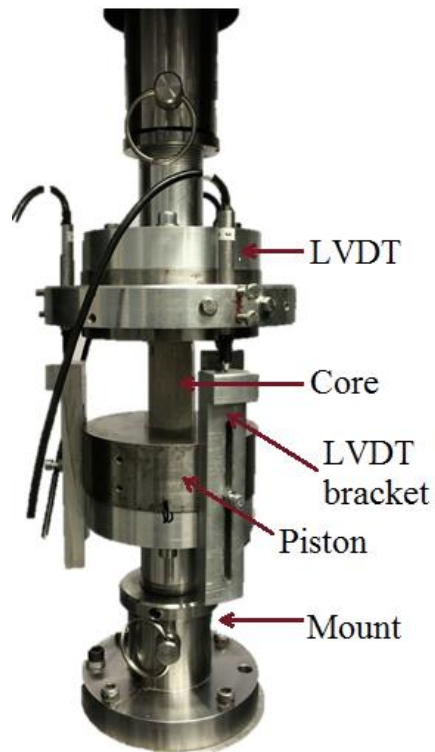*Figure 3-1 A sketch of the load frame*

Figure 3-2 Close up of the setup

3.2 Equipment

The most important components in the experiments will be presented in this section. The equipment and data acquired varies between experiments. The main reason for this is low availability in addition to lack of training and instruction for using the equipment. An overview of the equipment used for the different tests can be seen in Table 3-1. The sampling rates have been set to 5 Hz for the LVDT, 1 Hz for stress sensors, 0.1 Hz for temperature sensors, 0.1 Hz for the strain gauges and between 0.0033 and 0.05 Hz for acoustic measurements.

3.2.1 The cores

Two different rock types have been used during the experiments, Saltwash South and Castlegate. Cylindrical cores have been taken from the same block, reducing the difference between the cores from the same rock. The size of the Saltwash South cores was approximately 1.5 inches (3.8 cm) in diameter and 3.0 inches (7.6 cm) in length, while the size of the Castlegate cores was approximately 1.0 inches (2.5 cm) in diameter and 2.0 inches (5.1 cm) in length.

The uniaxial compressive strength (UCS) was measured for both rock types according to the procedure in 3.3.1 UCS testing. The dimensions of the cores were measured using a digital sliding caliper. Two perpendicular measurements were taken for the length of the core samples. For the diameter of the samples, four measurements were taken. Between each measurement the core was rotated 45 degrees and the caliper where slid up ¼ of the axial length. In addition to the dimension, the cores were weighed before the experiments. Before the cores were weighed they had been dried in an oven at 67 °C for at least 12 hours. Further the cores were cooled down to room temperature before the experiment was started.

Experiment [#]	Equipment in use			
	LVDT	**Strain Gauge**	**Temperature sensor**	**Acoustics**
343_02_06	✓		✓	
313_02_04	✓	✓	✓	✓
313_02_08	✓		✓	✓
313_02_09	✓		✓	✓
313_02_12	✓	✓	✓	✓
313_02_13	✓	✓	✓	✓

Table 3-1 Overview of the equipment in use for each experiment

Saltwash South is a soft rock consisting of well-rounded grain with mostly tangential contacts and no visible cement (Heiland & Flor, 2006). Four UCS test were run on the same amount of cores of Saltwash South in order to give a best estimate for the strength of the rock. The results from the test can be found in Table 3-2, which shows that the average UCS of Saltwash South tested 1.40 MPa.

Castlegate is a weak outcrop rock with 28-29 % porosity and consists of 70% quartz and 30% feldspar (Fjær E. , 2006). It is characterized by beige/yellow color, a relatively homogenous structure, without distinct laminations. It contains well sorted grains of fine- to medium size with sub-granular to rounded grains (Eberhard, Stead, & Morrison, 2007, p. 1712). Similar UCS test was performed as for the Saltwash South cores. The UCS for Castlegate was 17.09 MPa on average over 2 tests; the results are in Table 3-2. The Young's modulus was acquired from the same data as the USC and was interpreted from the tangential modulus, calculated from the slope of the axial stress versus the axial strain (Fjær, Holt, Horsrud, Raaen, & Risnes, 2008, p. 267). The Young's modulus found from the two tests differed significantly, most likely caused by different load rates. The measurements of the Castlegate cores can be found in Table 3-2.

Formation	Sample	UCS [MPa]	Max Strain [mStr]	Young's modulus [GPa]
Saltwash South	343_02_02	1,13	9,20	0,19
	343_02_03	1,47	12,57	0,24
	343_02_04	1,85	10,35	0,29
	343_02_05	1,14	12,13	0,19
	Average	**1,40**	**11,06**	**0,23**
Castlegate	313_02_01	16,93	7,14	2,91
	313_02_02	17,25	19,19	1,12
	Average	**17,09**	**13,17**	**2,02**

Table 3-2 Results from the UCS tests ran on Saltwash South and Castlegate cores

3.2.2 Linear Variable Differential Transformer (LVDT)

3.2.2.1 Setup

Three LVDT's are mounted in premade slots in the upper piston, and are placed at equal spacing 120 degrees apart, as can be seen in Figure 3-2. The LVDT's are connected to a Data Acquisition System called Quantum MX440B, which in turn is connected to a computer. The LVDT measurements are recorded and stored in the software called Catman AP (V 3.5.1).

The LVDT's and the brackets are position in such way that the three LVDT's are working within the linear range of the sensor during the entire experiment. The linear range is found from the calibration of each individual LVDT, the calibration data can be found in Appendix II.

The LVDT is a RDP (4528) GTX2500, which has a total range of 2.5 mm and a linearity of ±0.25 % within in the linear range. The repeatability or precision of the measurements are listed as 0.15 µm.

3.2.2.2 Working principle

Linear variable differential transformer or LVDT's can be used to measure the axial displacement over the length of a core sample. The design of the LVDT consists of a cylindrical array of primary and secondary windings with a detached cylindrical core which passes through a hollow center (Applied Measurements, No data).

An A.C. current with constant amplitude and a frequency of 1 – 10 Hz is transmitted to the primary windings. In turn this produces an alternating magnetic field in the center of the transducer which induces a signal through the secondary windings; labeled S^1 & S^2 in Figure 3-3. The signal through the secondary windings is a function of the position of core, meaning movement of the core causes the secondary signal to change. The two secondary windings are positioned and connected in a specific arrangement, causing the signal null out when the core is positioned in the center (Applied Measurements, No data).

Movement of the core from the center point in either direction causes the signal to increase. As the windings are wound in a particular precise manner, the signal output has a linear relationship with the actual mechanical movement of the core for a specific range. The equipment was calibrated within this range, and all experiments are performed within this range.

3.2.2.3 Calibration of the LVDT's

The LVDT's installed in the setup was already calibrated and the data from the calibrations was put into the software used to record the LVDT data. The linear range mentioned in chapter 3.2.2.1 is determined by comparing the linear regression of the calibration data to the real data. The squared difference of the two data series are found for all the three LVDT's. Figure 3-4 shows that the squared difference is smallest for the range from -150mV/V to 150mV/V. However, the squared difference for all LVDT's/channels are considered to be sufficiently small within in a range of -300mV/V to 300mV/V. This corresponds to a total displacement range of 4.0 mm. The calibration data and the regression equations can be found in Appendix II.
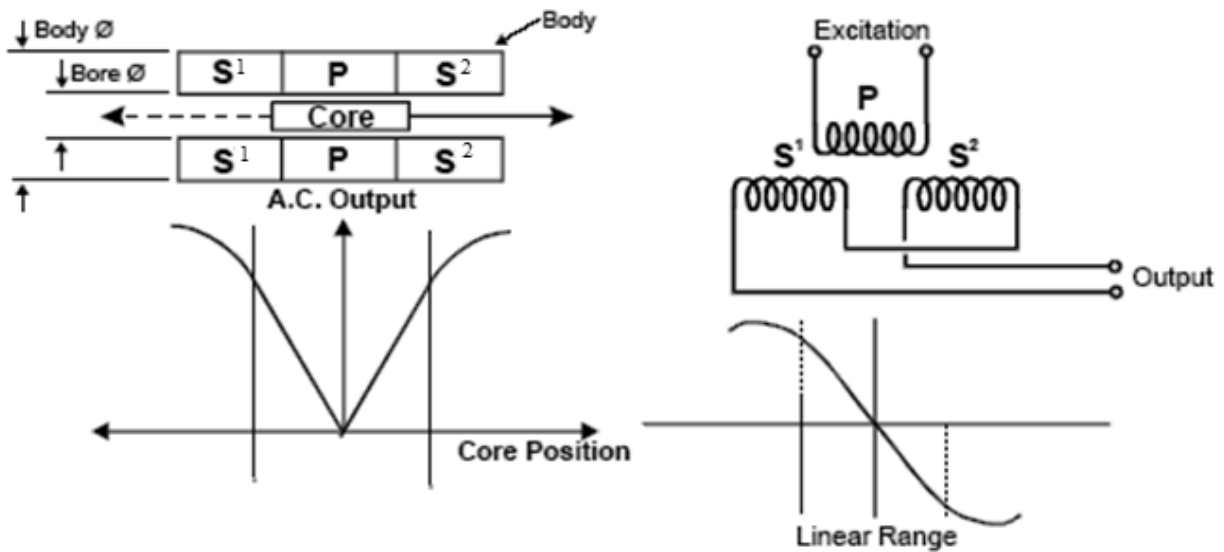
Figure 3-3 Function of the LVDT's. Figure modified from (Applied Measurements). (The right part of this figure has been moved from the bottom of the original figure)
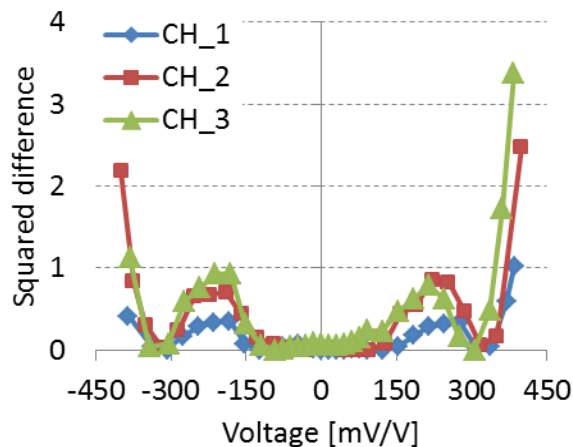
Figure 3-4 Squared difference of the calibration data and the regression of the data

3.2.3 Temperature sensor

3.2.3.1 Setup

Experiences from the Specializations Project showed the previous setup was very temperature sensitive. It was decided the setup was to be changed in addition to the location of the setup. The temperature sensitivity for the new setup was not known, neither was the temperature variation in the room. Due to this fact it was decided temperature readings were to be recorded for the series of experiments.

The temperature sensor installed was a Pico Technology TC-08 USB logger. It was directly connected to a computer with the appropriate software and was used for all the discussed in this thesis. The logger has 8 channels, of which two were coupled to temperature sensors. One sensor was put between the plastic sleeve and the sample, while the other was placed on the piston close to the outside of the plastic sleeve.

3.2.3.2 Working principle

The logger can use up to 160 thermocouples simultaneously and can record at a rate of 1 reading a minute. For this experiment the temperature was logged every 5-30 minutes depending on the predicted length of the experiment. Thermocouples are two metals with different material properties. If one of the junctions is heated with respect to the other, a current will flow. The magnitude and directions of the current is a function of the temperature difference and the material properties of the two metals. This phenomenon is known as the Seebeck Effect (Pico Technology Limited, 2005). The thermocouple circuit generates a measurable low-voltage output, which is almost proportional to the temperature difference between the two metals.

The accuracy of the measurements is according to the User's Guide (Pico Technology Limited, 2005) the sum of ± 0.2 % and ± 0.5 ℃. This means the maximum uncertainties of the readings are:

$$\zeta = 0.002 \times T[°C] + 0.5\ [°C] \qquad\qquad 3\text{-}1$$

$$\zeta = 0.002 \times 25[°C] + 0.5\ [°C] = 0.55°C \qquad\qquad 3\text{-}2$$

where ζ is uncertainty and assuming the maximum temperature during the experiments was $25°C$. Although the uncertainty is relatively high, the trends of the temperature are evident and consistent. Due to this the accuracy of temperature measurements is believed to be good.

3.2.4 Strain gauges

3.2.4.1 Specifications

In addition to LVDT's, strain gauges were used during several experiments as a second measurement for the axial deformation as well as radial deformation, to give supporting data. Figure 3-5 show a strain gauge similar to the ones used in the experiments. It has a rosette with two independent resistors, measuring the deformation in perpendicular direction. Each of the two circuits has two soldering tabs where wires are connected. The components mentioned are attached to a foil that is glued onto the rock. A detailed procedure for preparing the strain gauges can be found in 3.3.2.3. The strain gauge is connected to the StrainSmart® Data Acquisition System using a System 5000's Model 5100B Scanner, which in turn is connected to a computer. The software used to scan, calibrate and record is StrainSmart 5000 v 3.10. Specific details of the strain gauges can be found in the Appendix II.

3.2.4.2 Working principle

When a core is deforming the strain gauge will follow the local deformation of the area where it is attached. The resistors will deform, resulting in a change in the resistance through this specific part. The change in resistance is transformed to deformation by a linear relationship (Omega, 2015). The resistance in the strain gauges used was 120 ohm. The linear relationship between the changes in resistance is the gauge factor. It is determined through calibration of the specific gauge type, and is the ratio between $\Delta R / R_0$ and $\Delta L / L_0$, respectively resistance and strain. R_O is the initial unstrained resistance of the gauge and L_0 is the initial length (Vishay Micro-Measurements, 2003). The gauge factor is given to be +1.3 +/- 0.2 according to the packaging.
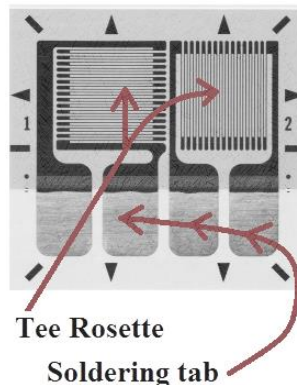
Figure 3-5 A Tee Rosette strain gauge, where the two grids are perpendicular

A three-wire quarter bridge circuit is used to connect the strain gauges to the transducer. Two wires are soldered onto the soldering tabs and run to the four-pin connector.

The benefits of using a three-wire circuit includes an intrinsic bridge balance, automatic compensation for the effects of lead wire temperature changes on bridge balance, and increased measurement sensitivity compared to the two-wire configuration (VPG & Micro-Measurements, 2010).

3.2.5 Acoustic

The setup of the acoustic system consists of an Arbitrary Waveform Generator, a Power Amplifier, Transmitter, Receiver, Data Logger/Switch Unit, Digital Oscilloscope and Computer. The setup of the system is illustrated in Figure 3-6. More specific the hardware used is:

- Waveform generator: Agilent 33220A
- Power Amplifier: T & C Power conversion Inc. Ultrasonic Amplifier AG 1017L
- Data Logger: Agilent 34970A
- Digital Oscilloscope: Tektronix TDS3012B
- Computer: Software, Aptrans

In the experimental setup a transmitter is situated in one of the pistons and receiver is situated in the opposing piston. The wave passes through the amplifier, where the signal is amplified by 30 %. The full waveform is recorded by the acoustic system and stored by Aptrans as a binary file. In order to obtain useful data from the binary file an add-on[4] is installed in MATLAB. It extracts amplitudes and travel times. In the add-on the arrival time is picked at first positive zero crossing.

---

[4] The program was developed by SINTEF

All the measurements of the P-waves are taken for waves propagating along the vertical axis of the core. This implies that there is no information about the wave anisotropy of the rock. The velocity is found by dividing the length of the core on the travel-time according to:

$$v_P = \frac{L(t)}{\Delta t} \qquad\qquad 3\text{-}3$$

where L(t) is the time dependent length of the core, found by subtracting the strain (measured by the LVDT) from the length of the core. Δt is the corrected travel time, which is originally measured from the time it takes for the wave to travel from the acoustic transmitter to receiver. However the desired information is the travel time through the core. Thus the delay through the pistons has to be subtracted. The system correction factor is 3.27 us.
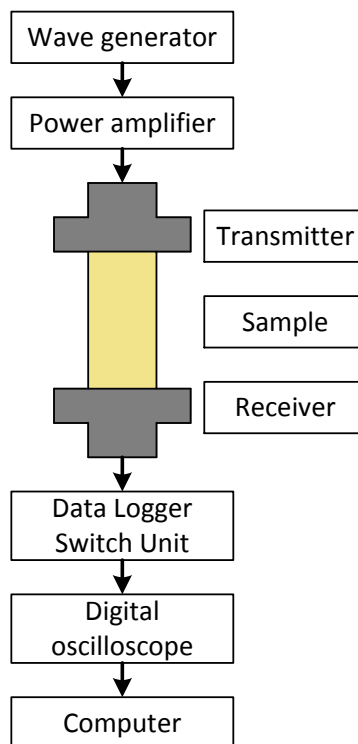
Figure 3-6 Acoustic system and signal trace

3.3   Experiment procedures

3.3.1   UCS testing

In order to measure the uniaxial compressive strength (UCS) of the materials measured, several UCS test has been run. The script for the loading was created in cooperation with a SINTEF employee. Figure 3-7 shows the stress path toward failure. As seen a stress cycle is run prior to the main loading cycle. The reason for this is to let the system set. The stress is reduced again before the main loading cycle is run until the sample fails. The max stress reached during the test is considered to be the UCS of the core. The different tests are run at the same test speeds for the core in the same material in order to get good basis for comparing the different core samples. The load rate for Saltwash South was set to 0.2 mm/min for the preload cycle and 0.1 mm/min for the final loading. For Castlegate the load rate was changed in order to match the duration for the loading of the Saltwash South cores. The load rate was set to 0.5 mm/min for the first test on Castlegate.

3.3.2   Creep tests

3.3.2.1   Stress

The peak stress used during the preliminary experiments was limited to 15 MPa, which is about 88 % of the UCS found from tests. Different stress paths were used in order to check its impact on creep, and two main paths have been chosen. The first one can is in Figure 3-8. The stress is first increased to a value laying one fixed incremental step X, below the peak stress. Further the stress is increased to the peak stress, before it is decreased in steps with the same fixed increment X. The stress change and the hold period is the same for all the steps
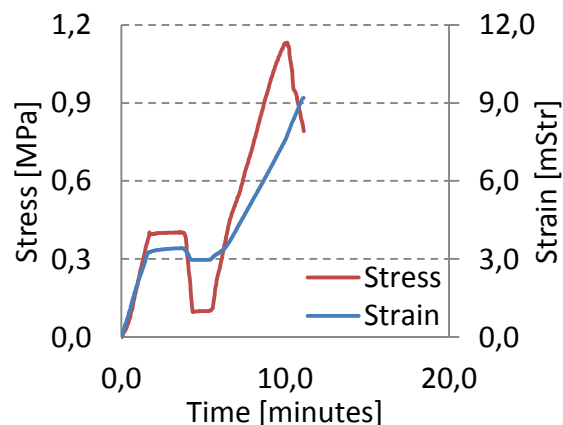
Figure 3-7 Stress and strain as function of time for core sample UCS 343_02_02

Figure 3-8 First stress path
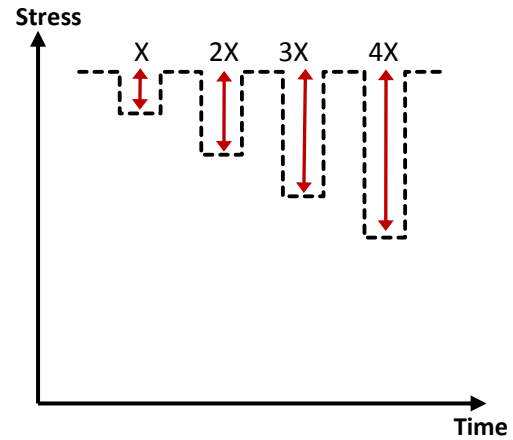
Figure 3-9 Second stress path

Figure 3-9 show the second stress path used in the experiments. First the stress path is increased to the peak stress. Next the stress is reduced by one incremental stress step, X, before it is increased to the peak stress. The cycle described here is one full cycle. Next the incremental stress change is doubled to 2X. For the next cycles the amplitude is increased with the magnitude of the primary increment, X.

3.3.2.2 Software procedure

The procedure is programmed in TestWorks and runs automatically when it is started. It controls the load rate, stress levels, hold times, max stress and the break sensitivity. A screenshot shot of the procedure editing mode is attached in Appendix III. Below is a list of the steps to make a procedure:

- The loading rate is controlled by the movement of the piston mounted on the crossbeam. This means that the loading rate is not given as MPa/min, but rather as mm/min. The appropriate loading speed is found during the UCS tests, which are run in advance of the creep experiments.
- A given number of load sequences with defined target stresses are entered.
- Next a hold period is defined, which is similar for all the steps during one experiment.
- In addition to this two safety parameters are defined. The first one being the max stress, preventing the load exceeding a given level, and the second the break sensitivity. The latter is defined as the percentage of the difference between the peak stress and the lowest stress after this point. In practice this means that the break sensitivity has to be set to above 100 % if the stress is reduced to zero.

36

3.3.2.3 Strain gauges

The strain gauges are mounted on a single foil and are mounted in a Tee position. Due to time constraints a simple glue strategy was chosen for mounting the strain gauges.

Firstly the wires were soldered onto the soldering tabs. For a good solder bond, surface oxides are removed using flux. This is applied to the tabs before small droplets of lead are melted onto them. The flux is also applied to the de-isolated ends of the wires before they are covered in lead. Further wires are soldered onto the droplets attached on the soldering tabs. The strain gauge and wires are clean with isopropanol to remove any salts from fingers and similar, which can alter the resistivity over the strain gauge. Further the resistivities over the two gauges are measured with an Installation Tester[5], to verify that there is no contact between the soldering tabs and that the resistivity is correct.

Two strips of tape is connected in parallel and the face of the strain gauge is fastened to the sticky side of the tape. A five minute glue is greased onto the backside of the strain gauge in a thin film, before the strain gauge is pressed onto the core with the thumb. The strain gauge is precisely attached and aligned along the axis of the plug. The pressure from the thumb is kept for 15-20 minutes before self-amalgamating elastic tape is wrapped around the core. The tape is non-adhesive in contact with other substances than itself, which makes it easy to remove. Due to its elastic properties it is easy to distribute the tension evenly over the strain gauge.

The wires are soldered onto a four-pin connector where a jumper wire is linking the two wires into a 3 wire quarter bridge described in chapter 3.2.4.
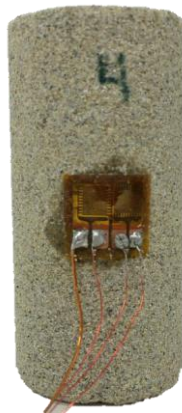
Figure 3-10 A core sample with a strain gauge soldered and glued

---

[5] Strain Gage Installation Tester Vishay Model 1300

3.3.2.4 Practical preparation and execution

The experiments conducted on unsaturated Saltwash South and Castlegate sandstone cores. The tests are run at various stress levels with different stress increases/decreases and different static periods. The stress is increased and decreased with the same speed for all core samples from the same material. The general procedure for the experiments follows the list below:

1. *Optional: Glue strain gauges
2. Dry samples in oven at 68 C.
3. Measure the weight and dimensions of the core.
4. Clean pistons for grain from previous experiment
5. Place the core between the pistons; put the plastic sleeve in place.
6. Make sure the LVDT's are connected to the pistons in a position that ensures that the core of the LVDT stays within the linear range during the entire length of the experiment
7. *Optional: Connect strain gauges to power supply/data acquisition unit.
8. *Optional: Prepare strain gauges software and check if strain gauges respond to axial and radial stress.
9. Prepare software for experiment: Acoustic, temperature, LVDT, stress and strain gauge
10. Align the sample to the center of the piston transferring the force from the load frame. This point is especially important to get an even stress distribution across the whole core.
11. Check the procedure
12. Take notes in the experiment journal
13. Lower the crosshead manually until just a small visible gap can be seen between the sample and the piston. Check the digital stress meter as the piston is lowered.
14. Use the computer controlled lowering mechanism to close the gap. Use a small piston speed to avoid damaging the core. Stop when the stress reaches 5-10 N.
15. Start the different recordings and note the time difference from the master time on the TestWorks® Software clock to the time the different recordings are started. Ideally the strain gauge measurement should be started before the procedure is started.
16. The temperature meter is hooked up to monitor the temperature during the experiment to check for any deviations in temperature.
17. The test will run automatically according to the pre-defined procedure entered in TestWorks and the equipment is left undisturbed for the rest of the experiment.

3.4 Risk assessment

As part of the preparation for the experiments an evaluation of the risks associated with the execution of the experiments and the other work on the lab was conducted. The hazards where identified and the risks associated was evaluated. Appropriate countermeasures were suggested to mitigate the risks and lower the probability and consequence of the risks. A risk register was made and serves as an overview of the risks relevant for the lab work. The actions, hazards risks and mitigations can be found in Table 3-3.

Action/ Equipment	Hazard	Risk description	Mitigation
M-Flux AR-2	Highly flammable	Fluid and fumes can catch fire in contact with source of ignition	• Good ventilation • Keep Flux and source of fire separated
	Fumes	Vapors may cause drowsiness	• Good ventilation, suction outlets. • Keep bottles closed when not being used
		Irritation/damages to skin and eyes in case of contact	• Use glasses when the Flux is in use
Soldering	High temperature	Can cause burns to skin	• Use suitable station which has a suitable holster to rest the iron in when not immediately needed
		Molten solder can cause spatter	• Component should be dry
		Ignition of the surroundings	• Housekeeping • Keep soldering pin in the station when it is not in use
	Fumes	Harmful if inhaled	• Good ventilation, suction outlets
Load frame	Crush and pinch	Personnel crush injuries	• Keep outside the identified crush zones when the frame is operated. • Operator of frame makes sure no one is inside. • Proper training
	Improper use	Damage to the frame or other equipment	• Enable safeguards such as the mechanical break, to restrict movement if sample breaks. • Specify proper break sensitivity in TestWorks • Proper training
	Hydraulic pressure	Hydraulic pressure beyond rating can rupture components and lead to personnel and equipment damage	• Do not exceed working pressure 3000 psi. • Wear safety glasses
	Flying debris	Debris from cores can cause eye injuries	• Wear safety glasses inside barriers around the frame

Table 3-3 Risk register for lab work

3.5 Model fitting

3.5.1 Data processing

The data obtained from the experiments have to be slightly altered before the Burgers model can be fitted to the real data. The loading cycle takes between 3-4 minutes, which means the stress increase is not instantaneous as assumed by the Burgers model, where the stress increases from one value to another in an infinitesimal time step. This is done although the finite difference method also can predict this period. However for the series of experiments fitted to the Burger's model, the loading phase will be discarded from the data. Also the first step of the raw data will be set to the constant value held before the loading starts; e.g. for the first loading cycle the first of the raw data will be set to zero. The second line will have the same reference time as the first line since the stress increase is instantaneous.

Time [s]	Stress [MPa]	Measured [mStr]	Model [mStr]	SD
0	0	0	0	0
0	16.393	11.084	11.086	6.47E-06
10	16.397	11.131	11.128	1.1E-05
20	16.398	11.163	11.161	5.42E-06

Table 3-4 Example of the first four rows of the model fitting in Excel

The magnitude of the axial displacement is very small, which have given rise to noise in the LVDT recordings due to insufficient precision. This issue will be discussed in chapter 5.4.3. The issue will be mitigated using forward and backward averaging (5 point forward and back, 11 in total) to smooth out the data before the models are fitted to the data. In addition any accelerated creep phase has to be discarded from the data that is to be fitted.

The units used when the Burger's model is fitted are mStr, MPa, hrs. or min.

3.5.2 Least-square regression in Excel

The data obtained in the experiments will be fit to the models described in and chapter 2.2. This will be done using least square regression, which means summing up all squared differences between measured data and model data, minimizing the sum. Described mathematically the process yields:

$$SD = \sum_{i=1}^{n} (\varepsilon_i - \varepsilon(model)_i)^2 \qquad \text{3-4}$$

where SD is the squared difference, ε_i is the empirical data and $\varepsilon(model)_i$ is the model prediction depending on the parameters in the bracket. This method will be used for both models. The fitting is performed using the built in Solver in excel, minimizing the squared difference in Equation 3-4 by changing the parameters of the model in question.

Limits for the different parameters are assumed to lie close to the range of results from the Specialization Project. The limits of parameter X in the Solver function in Excel are set to the following:

$$50\% \times lowest\ result < X < 150\% \times highest\ result \qquad \text{3-5}$$

The reason for this is to add some margin to the results found. The results of the fitting of the two models are attached in Appendix IV. The parameters listed in Table 3-5 and Table 3-6 are inserted into base equation 2-16 and 2-30 respectively or redeveloped versions of them.

	E_1	E_2	η_1	η_2
Min	4.29	0.48	2.219	29.75
Max	84.3	2.62	140.8	1456

Table 3-5 Bondaries for the Burgers Model, including the extra margin

	der	dt	E* [MPa]	n	q [1/Str]	τ [1/time]
Min	0.000008	0.02	555.5	0.05	30.685	0.00
Max	0.900000	0.50	3347	75.0	198.75	0.20

Table 3-6 Boundaries for the FORMEL model, including extra margin

3.5.3 R-squared

When a curve is fitted by linear regression in Excel R-squared is calculated as a measure for the precision of the fit between the regressed model and the measured points. The mathematical explanation of the term is explained below:

R-squared is based on the factor of the total sum of squared and the residual sum of squares.

The total sum of squares is given by:

$$SS_{tot} = \sum_i (y_i - \bar{y})^2 \qquad \text{3-6}$$

where y_i is the measured value and $\bar{y}$ is the arithmetic mean of the measured values. The arithmetic mean is given by:

$$\bar{y} = \frac{1}{n} \sum_{i-1}^{n} y_i \qquad \text{3-7}$$

where n is the number of data points.

The residual sum of square is given by:

$$SS_{res} = \sum_i (y_i - f_i)^2 \qquad \text{3-8}$$

where f_i are the modeled data points.

R-squared is finally given by:

$$R^2 = 1 - \frac{SS_{res}}{SS_{tot}} \qquad \text{3-9}$$

4 Experimental results

A total of 12 uniaxial creep tests have been performed on dried cylindrical cores of two different sandstones. Most of the experiments are run over a time period of 20-24 hours due to tight schedule. Due to this fact the peak stress of the experiment was set to ~88 % for most experiments and 96 % for one. Different stress paths was tested, where the stress was varied in increments to check the impact of variations in stress, with emphasize on unloading. The two sandstones are Castlegate and Saltwash South, labeled 313_02_xx and 343_02_xx respectively for the remainder of the thesis.

Only one experiment was conducted on Saltwash South due to the low strength of the rock, while 11 experiments where run on Castlegate. Out of these tests some of the data was partly lost due to lack of precision and wrong file format when the files were store. The LVDT data extracted from Catman (LVDT software) was stored as ASCII-files with too few digits. Consequently the resolution for small stress increments was not sufficiently good for any further discussion.

The successfully stored data will be visualized in the following sub paragraphs, structured by with one experiments in each sub-section. Both time and stress steps have been varied from experiment to experiment, as well as the type of stress (see chapter 3.3.2.1 Stress). Since most of the experiments use small stress and time increments, which has small impact on the strain and P-wave velocity, a zoom-in of all the stress steps is included for all experiments. Due to the vast amount of plots, they have been attached in Appendix IV, even though some of the figures from the appendix are mentioned in the results section.

The zoom-ins show that the accuracy of the LVDT's was inadequate, since it can be observed that a systematic error, where the strain is seemingly oscillating. In order to reduce this inaccuracy of noise, forward-backward averaging is used. Eleven point are used since the sampling rate of the LVDT was very high, 5 Hz. The zoom-ins or magnification of the different hold periods have been labeled Increase X and Drop X for the remainder of the thesis. For this context Increase X, means the hold period following an increase in the stress, while Drop X mean for the hold period following a decrease in stress.

4.1   Core sample 343_02_06

The experiment was performed on Saltwash South, which is a very weak sandstone. During preparations of the experiments the cores "crumbled" for every touch, meaning that the dimensions of the core also changed slightly. Due to the low strength it was not possible to glue strain gauges to the cores, since the strength of the core itself is much lower than the strength of the glue. In addition it was not possible to make acoustic measurements, most likely caused by poor contacts between the pistons and the cores, caused by coarse grains "sticking out" of the top and bottom of the core. Figure 4-1 shows how the stress and strain develops over time, and Figure 4-2 to Figure 4-4 show plots of zoom-sin of the three first hold periods. This can be seen in all three zoom-ins the strain curves have steps, which becomes very obvious in the figure for the 1st stress drop, where the scale of the axis is very small. The step effect is caused by the mentioned lack of digits.
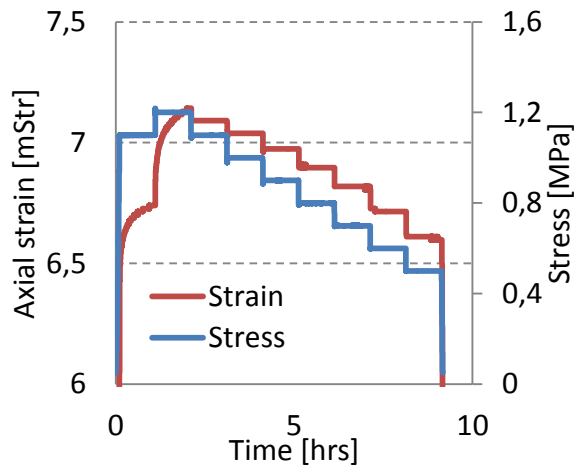
Figure 4-1 Stress and Stress and strain curves
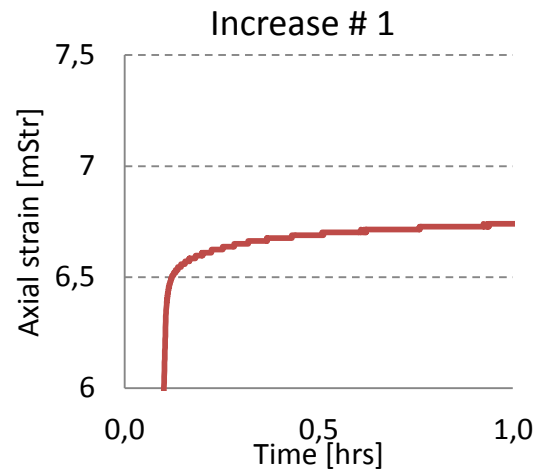
Figure 4-2 A zoom-in of the 1st streess increase
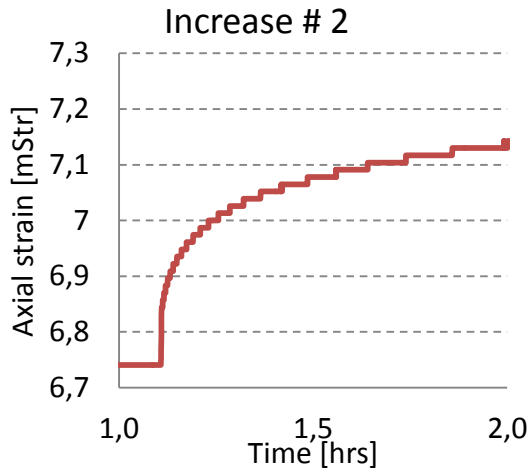
Figure 4-3A zoom-in of the 2nd stress increase *Figure 4-4 A zoom-in of the 1ˢᵗ drop in stress*
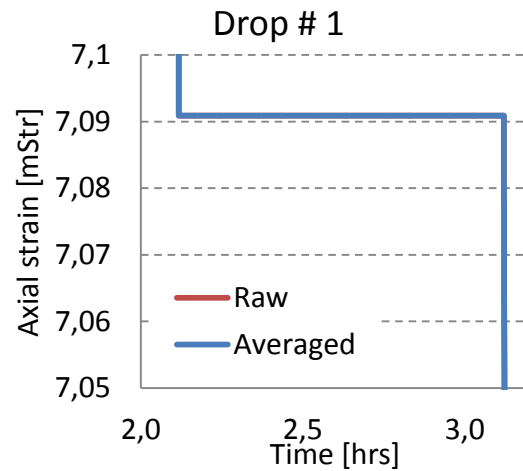
The UCS varied from 1.13-1.85 MPa over four tests with the same loading cycle and rate. The standard variance of the four tests was 0.29, which is 21 % of the average value of the samples. Due to the high variation in strength it is hard to find the correct peak load for the experiments.

Similar problems have occurred in other studies, amongst them Hoek et al (2000). To mitigate the issues with varying strength they used artificial sandstones to decrease the variance from sample to sample. The reason stated was that the low-strength Saltwash South frequently was observed to have highly variable mechanical properties and physical characteristics (Hoek, et al., 2000).

Due to the strength variations and the issues with the measuring equipment it was decided that experiment 343_02_06 would be the only experiment performed on Saltwash South. Another deciding factor for abandonment of further testing was the limited allocated lab time. Since previous experience showed better results for Castlegate cores, the rest of the test was performed on Castlegate.

4.2 Core sample 313_02_04

The test was performed on a cylindrical Castlegate core with dimension of approximately 1 inch diameter and 2 inch length (exact value can be found in Appendix III). The stress path was chosen to check how the material responds to fluctuations in the stress with increasing magnitude. The stress follows the path mentioned in Figure 3-9, where X is 1 MPa and the duration of each step is 2 hours. Totally 5 types of measurements was conducted; stress, strain (LVDT and Strain Gauge), temperature and P-wave.

The stress and strain can be seen to the left in Figure 4-5 and the temperature can be seen to right. The strain varies along with the stress and the magnitude of the variations of the strain increases as the stress increases. Figure IV-I and Figure IV-II show a zoom-in of each stress step and can be found in Appendix IV. The zoom-ins show the response of each loading cycle is very similar. The response of unloading however changes from step to step. For the first unloading the curve slopes upwards, while it starts sloping downwards for the following steps. During the experiment the temperature varies ~0.9 °C, which does not seem to affect the deformation.

A strain gauge with one axial and radial component was attached to the core sample to monitor the local deformation in the sample. Figure 4-6 show the strain curves for both strain gauges. Like for the LVDT data, a zoom-in of all the stress steps, for both axial and radial strain is attached in Appendix IV. From this data it can be observed that the transient response of the axial deformation starts to decrease compared to the first cycle, but starts increasing when the stress steps becomes sufficiently large.
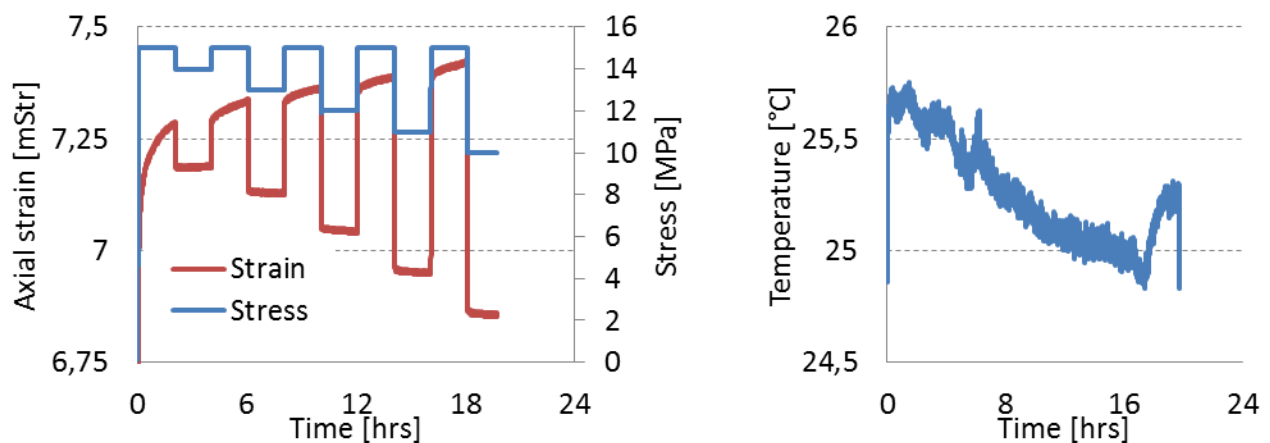
Figure 4-5 Left: Stress and strain curves. Right: Temperature fluctuations during experiment

The left part of Figure 4-7 show an overview of the acoustics measurements recorded during the experiments, while the figure to the right show the P-wave velocity plotted as function of the stress applied. In the plot to the left side it can be seen that the instant response of the P-wave velocity moves in the same direction as the stress, i.e. the instant response of the P-wave velocity is proportional to the change in stress. The transient response of the P-wave velocity on the other hand, increases while the stress is kept constant. This effect can be seen for both increases and drops in stress, and can be seen more clearly in Figure IV-VIII and Figure IV-IX.
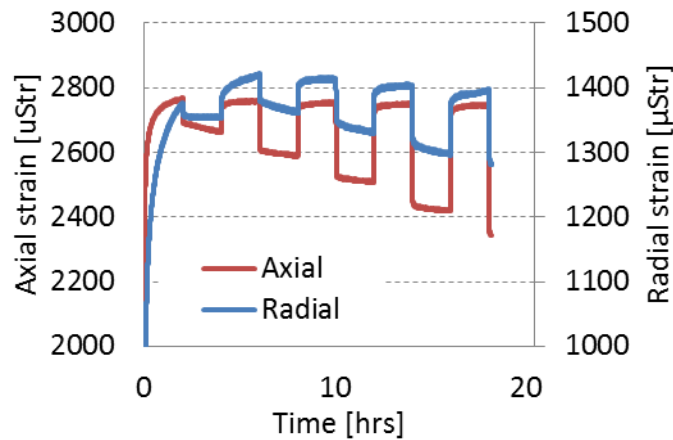
Figure 4-6 Deformation recorded by two strain gauges, one axial and one radial
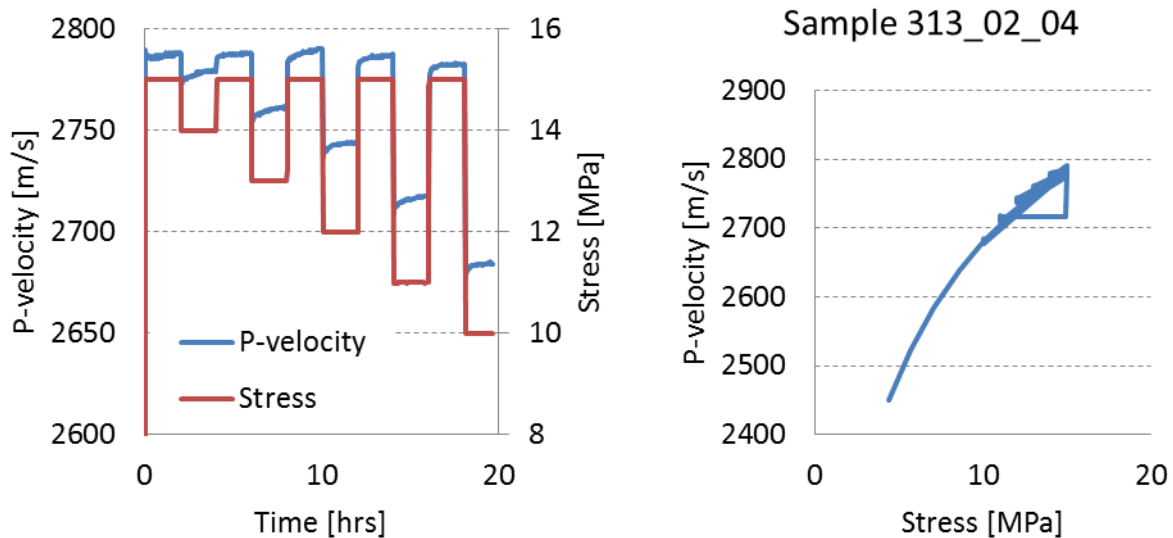
Figure 4-7P-wave velocity vs time and stress Left: P-wave velocities compared to the changes in stress. Right: P-wave velocity as a function of the stress applied.

4.3 Core sample 313_02_08

Figure 4-8 shows the first time step is longer than the other ones. Also the decrease in stress is two times the size of the other stress steps. This was caused by one wrong setting in the procedure in TestWorks, which indicated that the crosshead should go down rather than up. The consequence of this was that the stress level was skipped. The mistake was found around 6 hours into the experiment. At this point the procedure was manually overridden and was forwarded to stress level 3. Figure 4-9 show the temperature variation during the experiment. The largest difference between the highest and lowest temperature is around 0.5 °C. Investigating Figure 4-8 and Figure 4-9, the temperature does not seem to have any big impact on the strain.

The load rate used for loading and unloading is 0.2 mm/min and the first loading phase takes 4 minutes from 0-15 MPa. Unloading each step takes about 40 seconds, except for the first step which takes about the double. The max stress during the experiment is 15 MPa, which is about 88 % of the UCS, assuming the UCS values found in the UCS test are correct.

Figure IV-X shows the initial response of the rock is transient before it approaches a steady-state towards the end. Total strain at this point is 6.76 mStr, where the instant elastic response accounts for about 6.3 mStr of the strain, assuming the transient response during the loading phase is minimal.
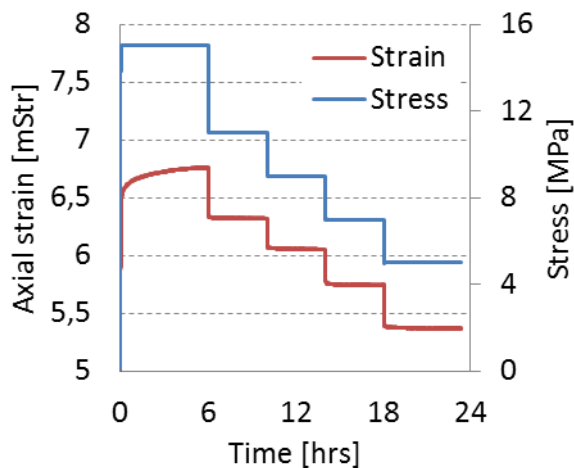
Figure 4-8 Stress and strain (LVDT) path for experiment on core sample 313_02_08.
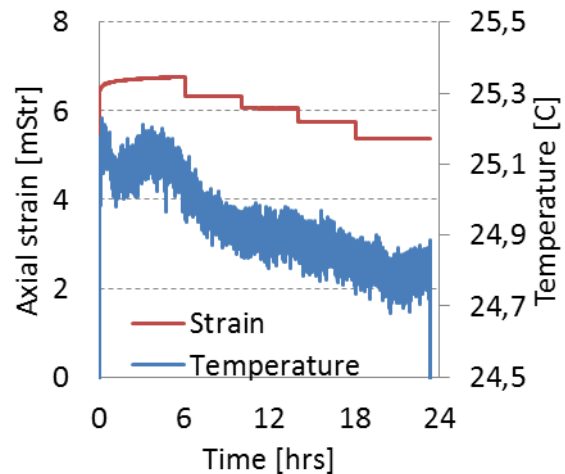
Figure 4-9 The temperature vs. the strain (LVDT) during the experiment

For the four drops in stress, the decrease in stress is 4 MPa for Drop 1 and 2 MPa for Drop 2-4. The total stress drop is 10 MPa which is 33 % of the max stress. As seen from the zoom-ins in Figure IV-X the total response of the transient recovery is about 0.09 mStr, and the instant elastic recovery is about 1.3 mStr. It is also worth mentioning that the scale of the axis (strain) in the figure of the increase step is 10 times larger than the axis in the figures where the decrease is displayed.

In addition to the recordings of the strain, using LVDT, acoustic P-wave measurements were recorded during the experiment. As for the strain data the time-dependent changes in velocities are relatively small for each time step, compared to the instant elastic response. Because of this the time-dependent part of each stress step is magnified and displayed in separate plots in Figure IV-XII. The entire path of the P-wave velocity is displayed in Figure 4-10, which shows the P-velocity is proportional to the stress. Figure 4-11 shows that the P-velocity seems to follow an exponentially declining function depending on the stress for the major part of the curve.
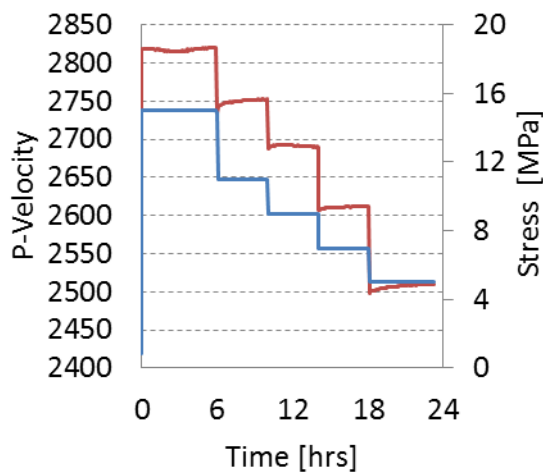
Figure 4-10 The P-wave Velocity and Stress vs. time
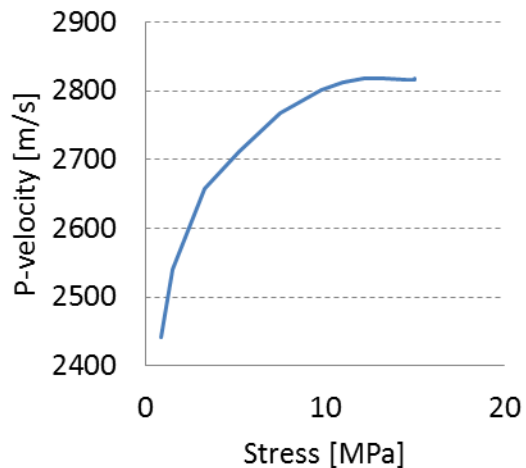
Figure 4-11 P-Velocity vs. stress

4.4   Core sample 313_02_09

As opposed to experiments on core sample 313_02_08, the time steps during this experiment were equal for every step and lasted for 2 hours. The absolute value of the stress steps was also equal for each step, shown in Figure 4-12.

Figure 4-13 show the temperature varies about 0.8 °C during the experiment, which is more than for the previous experiment. No clear temperature effects can be seen on the strain curve in Figure 4-12. Picolog crashed right after the measurements were started, due to a bug in the program. The logging was restarted after 3 minutes.

The load rate is equal to 0.2 mm/min and the first stress increase up to 14 MPa takes 4 minutes. The next increase in stress from 14 MPa to 15 MPa takes 15 seconds, while the decreases in stress take 12-13 seconds on average. The peak stress was 15 MPa, 88 % of the UCS, which was the same as for experiment 313_02_08.

Unlike the previous test, experiments on core sample 313_02_09 included one extra step where the stress level was increased. The reason for this was to compare the two first steps to each other. The total instant elastic strain was 5.98 mStr, when the all strain observed during the loading stage is included. The total transient and steady-state creep observed at the end of the loading phases (from t=0 hrs. to t=4 hrs.) was 0.64 mStr. This value is found by taking the total strain at this point subtracting the instant elastic strain.
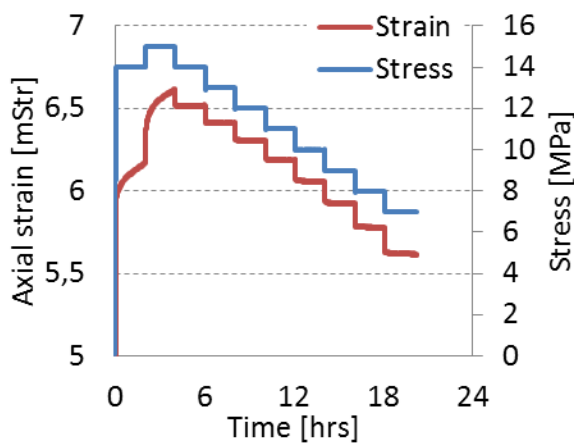
Figure 4-12 Stress and strain paths
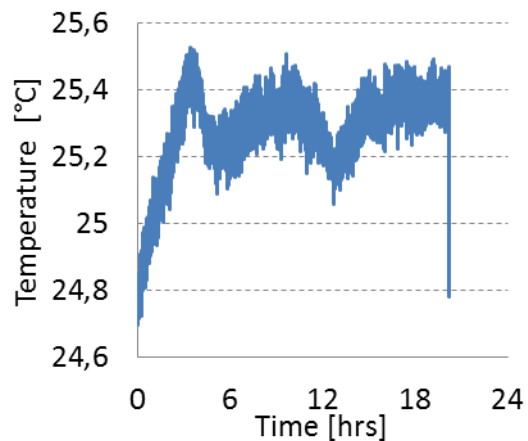
Figure 4-13 Temperature during the experiment

52

In total there are 8 steps where the stress drops. Although the stress reduction is the same for all steps the strain response clearly varies from Figure IV-XV to Figure IV-XXII. Note that the range of the vertical axis is 0.05 mStr for all the figures where the stress is decrease. The scale of the vertical axis of the figures where the stress is increased is 10 times larger.

P-wave measurements were also attained during the experiments. The travel time was used to find the velocity of the wave and is displayed in Figure 4-14 and Figure 4-15 as function of the time and stress respectively.
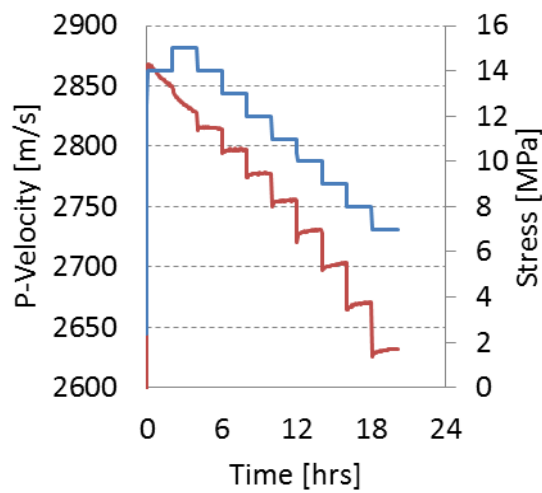
Figure 4-14 The P-wave Velocity and Stress vs. time
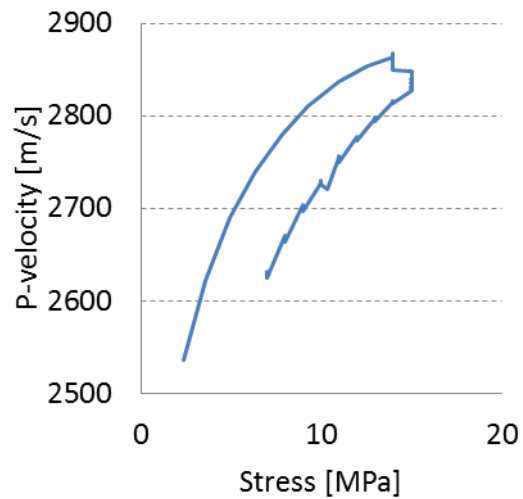
Figure 4-15 P-wave Velocity vs. stress

4.5 Core sample 313_02_12

The experiment on core sample # 313_02_12 was performed over a time span of 20 hours, with 2 hours steps with varying stress. All time steps last for 2 hours, however the change in stress varies. From step 1-2, 2-3 and 3-4 is 0.5 MPa, while it is 1.0 MPa for the other stress steps, this can be seen in Figure 4-16. The load rate was equal during all stress changes, including the initial load-phase and was 0.2 mm/min.

The max fluctuation in temperature is ~0.8 °C during the course of the experiment. As for the other experiments the fluctuations do not seem to have any significant impact on the strain rate.

The strain gauge measurements were started 200 seconds after the stress procedure was started. The loading phase up to the first stress step lasted for approximately 250 seconds, which means that large parts the initial elastic strain is not recorded by the strain gauges. Figure 4-17 show the axial and radial strain as function of time. The axial strain is defined positive for compaction, while radial strain is defined positive for expansion.
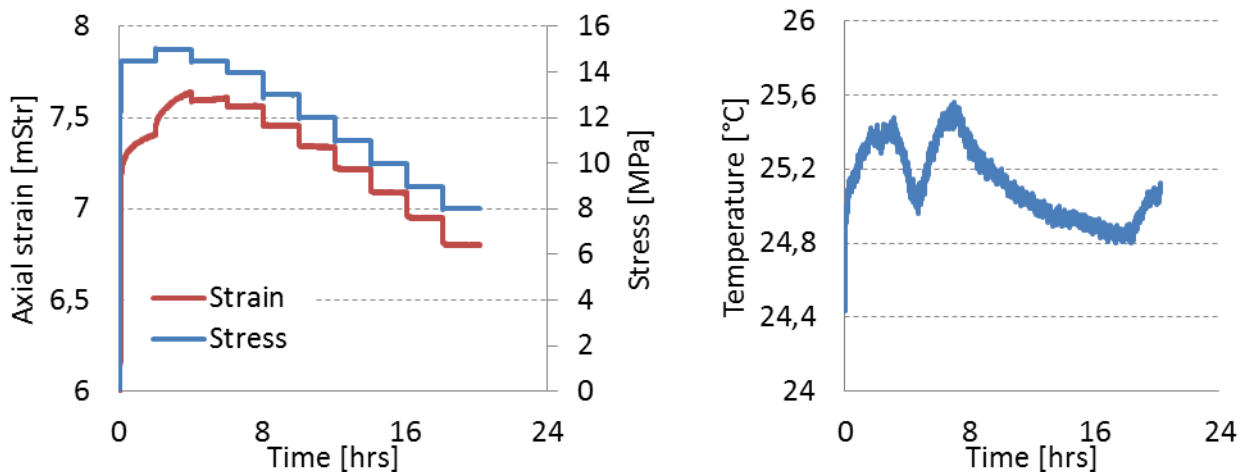
Figure 4-16 Left: Stress and strain paths. Right: Temperature during the experiment

P-wave velocities for the unloading cycles are found from transit times from the transmitter and through the core sample to the receiver. Figure 4-18 show that maximum velocity is reached during the initial loading phase. The P-wave velocity at this stage was 2836 m/s, while the stress was 14.11 MPa. It should also be noted that the P-wave velocity increases during some of the hold periods as a response to decrease in stress. This effect can be seen clearly in Figure IV-XXX and Figure IV-XXXI.
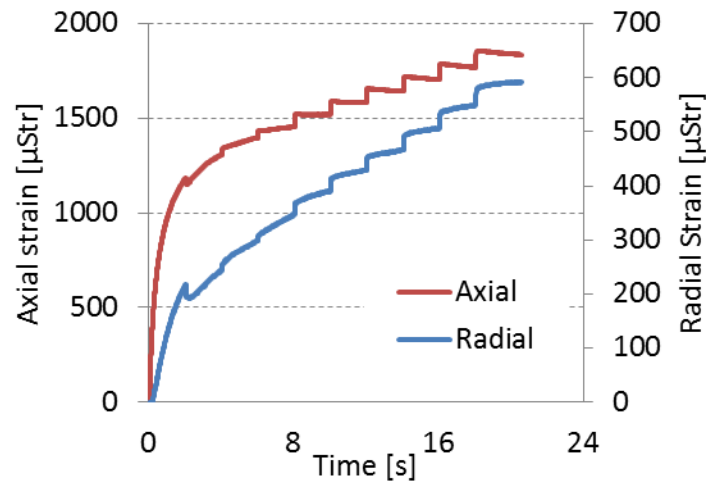
Figure 4-17 Axial and radial strain
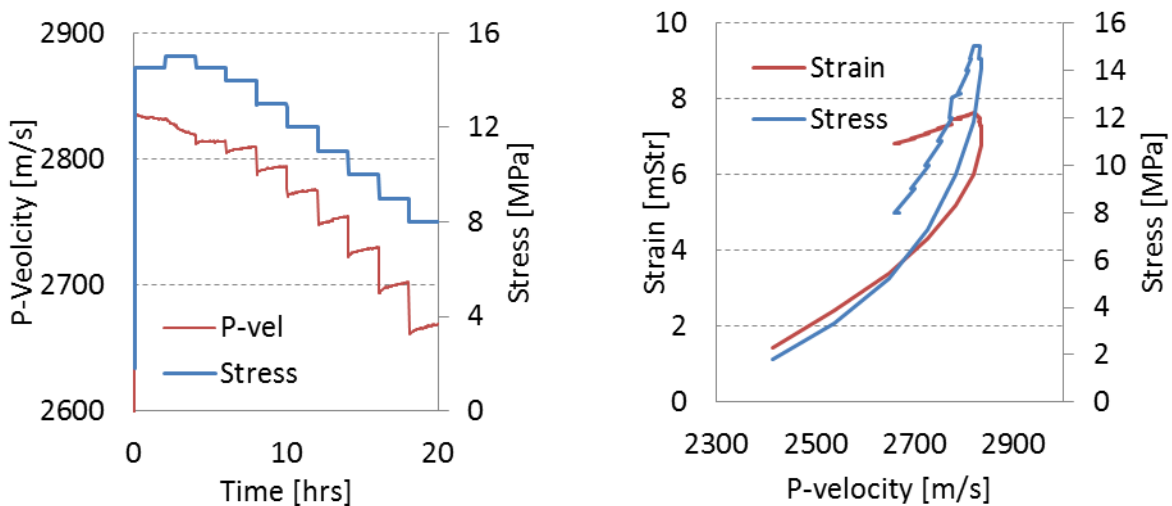
Figure 4-18 Left: Stress and P-wave velocity. Right: Stress & strain vs. P-wave velocity

55

4.6 Core sample 313_02_13

The purpose of the experiment was to load the sample to a sufficient level to induce failure within a period of 24 hours. It was decided that peak stress would be 96 % of the UCS. From Table 3-2 it can be seen that the UCS of the Castlegate samples was 17.09 MPa, giving a suggested stress of 16.40 MPa. The sample was loaded to approximately the intended stress and the stress was held constant until the sample broke after 14.1 minutes. The total strain at this point was 8.23 mStr not including the strain incurred the first 15 seconds before the LVDT recording was started.

The temperature varied with less than 0.4 °C, over the short course of the experiment. From visual observations the temperature variations does not seem to have any large impact on the strain.
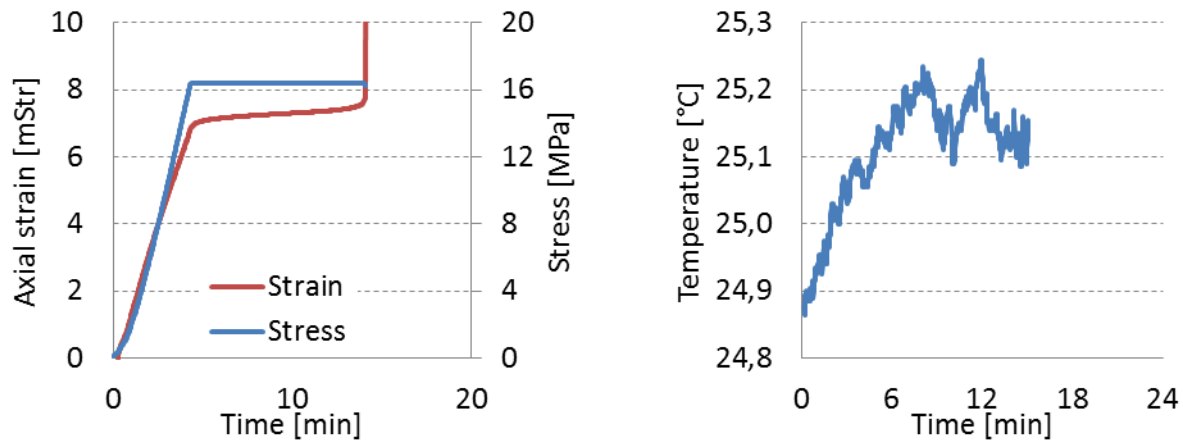
Figure 4-19 Stress, strain and temperature vs timeLeft: Stress and strain paths. Right: Temperature during the experiment

The recording of the strain gauge data was started 100 seconds before the master clock of the load frame. Figure 4-20 shows the strain data obtained from the two strain gauges glued to the core sample. The axial deformation is negative for compaction and the radial deformation is positive for expansion, which is most likely caused by incorrect wiring. When the loading phase ends at around 4 minutes (indicated by the black dotted line) the slope of the deformation changes for both the axial and radial deformation even though the stress is kept constant, which should only happen if the stress is decreased. To the right in Figure 4-20 the absolute value of the axial strain is used, meaning it is positive for compaction. Also the slope of the both the axial and radial strain is inverted after the load phase is ends. This produces strain gauge data which

56

coincides better with the LVDT data. The decrease in strain during the hold period can also be caused by improper gluing, causing the strain gages to detach from the core.

The P-wave recordings was set to sample every 30 seconds and was started 60 seconds before the recordings at the load frame. However the signal was not sufficiently good before 61 seconds into recordings from the load frame. Figure 4-21 show that the P-wave velocity peaks during the loading phase before it starts to decrease. The maximum velocity was 2809 m/s at a stress of 14.36 MPa. Due to the low sampling rate there are only 27 data points for the acoustic data.
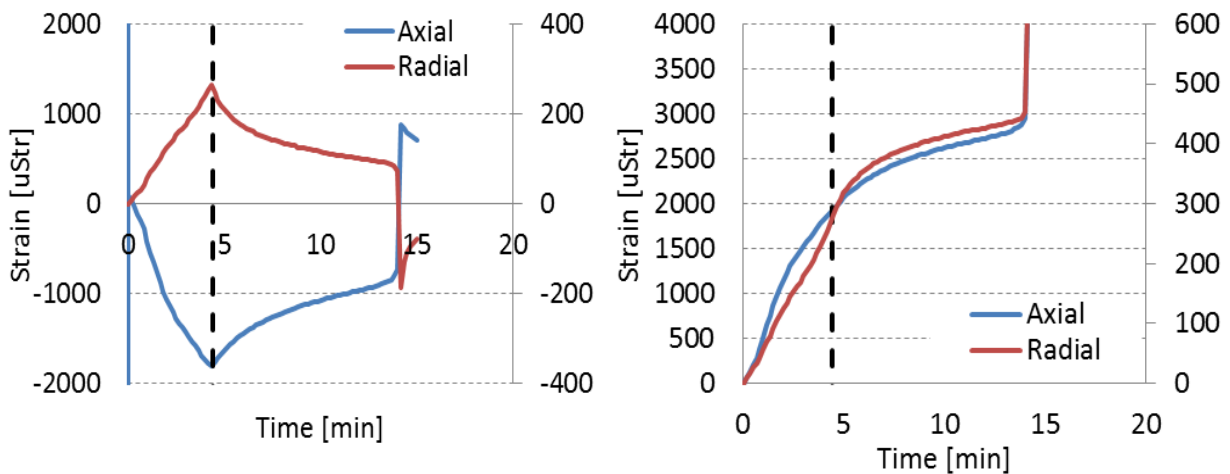
Figure 4-20 Strain gauge data

Left: Unprocessed deformation data from the strain gauges Right: Axial data is positive for compaction and radial data is positive for expansion. The slopes of the curves are inverted after the load period.
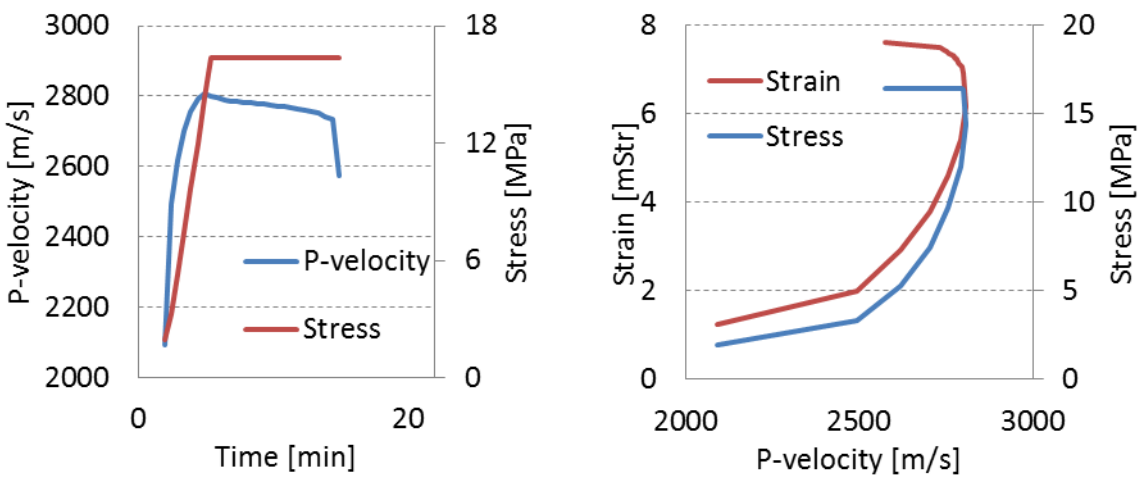
Figure 4-21 Left: Stress and P-wave velocity. Right: Strain and stress as function of P-wave velocity

5 Discussion

In this section several applications of the Burger's model will be tested and discussed to help in the understanding of rocks response to loading and unloading. In addition trends of strain and acoustic data will be identified and discussed.

5.1 Burger's model

5.1.1 Finite difference

The Burger's model is fitted to the measured data as described in chapter 2.3.1.1, 3.5.1 and 3.5.2. If R-squared (explained in chapter 3.5.3) is used as a reference for the precision of the fit, the apparent fit of the model is found to be very good by the use of 1-3 sets of parameters (E_1, E_2, η_1 and η_2), as listed in Table 5-1. One of the sets is used for hold periods after increases and the other set for hold periods following a decrease in stress. For two experiments, three sets of parameters are required to obtain a satisfactory fit, caused by two increases in stress where the rock responded differently.

Figure 5-1 shows an overview of the measured data and the model in the experiment on core sample 313_02_04. It shows that the model fits the entire experiment reasonably well. One set of parameters is used during the first loading phase and the second set of parameters is used for the remainder of the data. The Burger's model has also been fitted to the measured data of the four other experiments, where the fit is equally good if the overview plots and the R-squared values are considered to be good indicators for the precision of the fit. Selected plots for the four experiments can be found in Appendix V, showing the features discussed above. All the parameters used for fitting the Burgers model can be found in Table 5-2.

Figure 5-1 shows the Burger's model fit the measured data quite well when 2 to 3 sets of parameters are used. If only one set of parameters are used and fitted to the first hold period, the model differs significantly from the measured data. Figure 5-2 compares the difference between the measured data and the model, when only one set of parameters is used. The difference between the two curves increases as a function of time, and compared to Figure 5-1 it is obvious that the model falls far outside measured data. The R-squared rated precision of the fit for the model in Figure 5-1 is 0.9957 and -11.37 for the model in Figure 5-2. The negative value for the latter, indicate that a straight line would fit the measured data better than the suggested model.

	R-squared
313_02_04	0.9957
313_02_08	0.9963
313_02_09	0.9893
313_02_12	0.9995
313_02_13	0.9986
Average	0.9959

*Table 5-1 Overview of the R-squared value found from fitting
of the Burger's model by finitediffeerence solver*
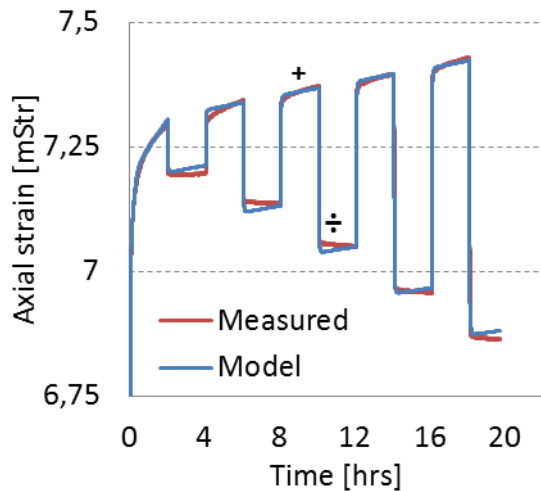
Figure 5-1 The measured deformation compared to the Burger's model on core sample 313_02_04, where + and ÷ represent Increase # 3 and Drop # 3 respectively
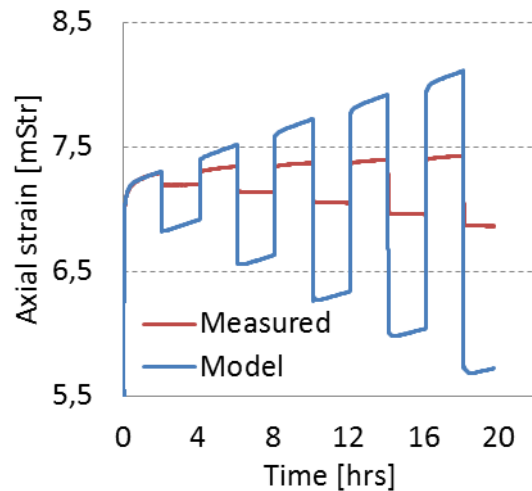
Figure 5-2 Burger's model fitted with one set of parameters

If the hold period following the first increase in stress is included in the interval for prediction, no other hold periods can be included if a good match for the entire interval is desired.

The deformation is consisting of two parts, elastic and plastic, both proportional to stress. For lower stresses the deformation is primarily caused by elastic deformation and some plastic deformation. When stress increase, the ratio of stress caused by plastic deformation increases. For the sake of the argument it is assumed that the ratio of plastic and elastic deformation increase linearly. If one integrate the contribution of the elastic and plastic deformation for the first stress increase and the accompanying hold period, it is likely that the elastic deformation has a larger contribution than the plastic. For a second load phase where the stress increase is occurring at a higher stress it can be presumed that deformation is largely caused by plastic deformation. Consequently the ratio between the elastic and plastic contribution will be different for the first

and the second load stage. If one assumes that the characteristics of the deformation are different for elastic and plastic deformation, it seems reasonable to think that the creep characteristics during the first and second load phase would be different. This would also imply that one set of parameters fitted to the first stress increase would not fit the second phase. Another important aspect when deformation is occurring in the plastic region is the validity of the Burger's model. It can still be fitted to the measured data, but since the model is based on viscoelastic principles it is being used outside its intended scope.

If the data from experiment 313_02_04 is investigated further, it is clear that the model is unable to predict the fine details during hold periods following a stress change. This becomes obvious when the scale of deformation is magnified for each individual hold period. Figure 5-3 shows that the model fits the hold periods after increase in stress relatively well, compared to hold period following a decrease in stress. It should be noted that the second set of parameters is used for both hold periods, the first being used to fit the first hold period.

Additional zoom-ins of the fitted data from experiment 313_02_04 to 313_02_13 is attached in Appendix V. All the zoom-ins are scaled up from the models fitted with up to three sets of parameters. An interesting feature detected from the graphs is that the fit of the model improves for each drop in stress, or as function of increasing time. For the hold period after the first decrease in stress, the model predicts that the strain rate will continue to be positive, meaning that the core will continue to compact. However for most experiments the measured data show that the effect of incremental decreases in stress exceeds the effect of the initial increase in stress. Thus a misfit between the model and the measured data is seen in most for several of the experiments. Also the Burgers model is unable to predict the transient recovery of strain seen for all experiments. One reason for this can be that all steps after the peak stress are fitted with the same parameters.
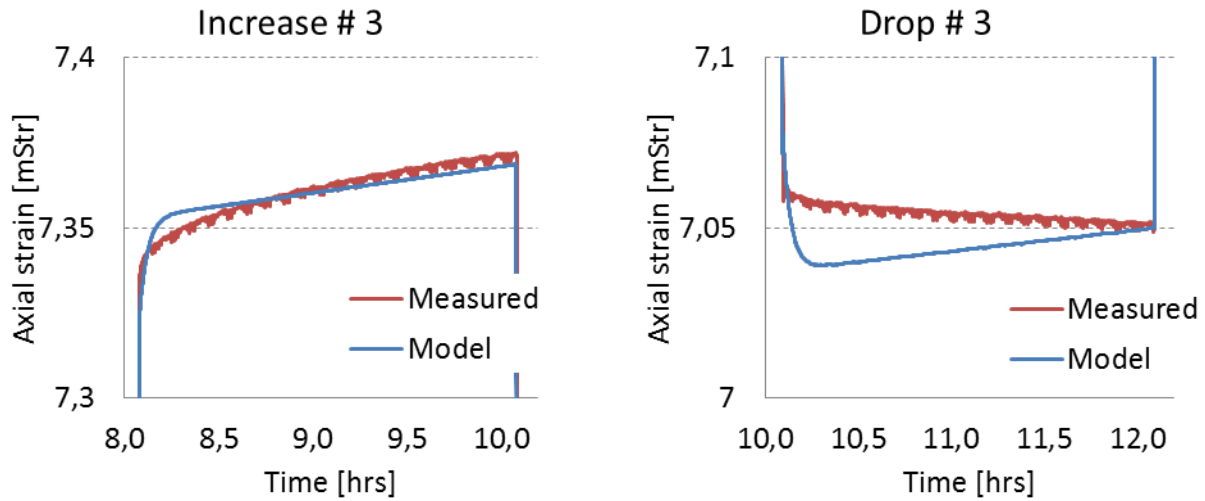
Figure 5-3 Magnification of two hold periods in experiment 313_02_04;
Left: Increase # 3 Right: Drop # 3

The primary goal of the Excel Solver, adjusting the parameters, is to obtain correct values for the instantaneous deformation caused by stress changes, E_2. The reason is that the parameters causes large positive and negative shifts in deformation when it is changed, thus it also has a large impact on the squared difference. And since the conceptual goal of the regression is to minimize the sum of square differences between the measured data and the model, the distance between the curves is the priority as the model is fitted, not the shape of the curve. The zoom-ins in Appendix V show that this is the case for many of the curves. A repeating problem is that the slope of the model is wrong during the hold period, and is in fact crossing the measured data.

Table 5-2 show the parameters used to fit the Burger's model to the measured data. *Inc # 1* is the set of parameters used in the first load phase and the following hold period. For two of the experiments another set of parameters is needed in order to fit a second increase in stress. *Inc # 2* includes this second load stage and the hold stage that follows. All increases and decreases in stress after the peak stress is reached can be fitted using one set of parameters, which is called *Remainder* in the table. Attempts were made to fit the Remainder with the same parameters used in Inc # 2, however this was not possible. An illustration of the interval where the parameters are used can be seen in Figure 5-4.

	Parameter	Inc # 1	Inc # 2	Remainder	Average
313_02_04	E_1	64.85	-	63.95	64.40
	E_2	2.109	-	10.57	6.34
	η_1	10.39	-	2.718	6.556
	η_2	274.1	-	1923	1099
313_02_08	E_1	84.86	-	35.26	60.06
	E_2	2.283	-	6.916	4.60
	η_1	23.04	-	0.459	11.75
	η_2	838.0	-	854.7	846
313_02_09	E_1	83.25	46.48	16.94	48.89
	E_2	2.394	6.182	6.769	5.12
	η_1	10.40	8.575	304.4	107.8
	η_2	191.3	233.3	4588	1671
313_02_12	E_1	61.78	46.65	34.05	47.49
	E_2	2.050	7.872	8.028	5.98
	η_1	6.292	23.87	239.6	89.91
	η_2	274.7	351.3	3611	1412
313_02_13	E_1	15.58	-	-	15.58
	E_2	2.681	-	-	2.68
	η_1	10.30	-	-	10.30
	η_2	492.7	-	-	493
Average	E_1	62.07	46.56	37.55	48.73
	E_2	2.303	7.027	8.070	5.80
	η_1	12.09	16.22	136.79	55.03
	η_2	414.2	292.3	2744.4	1150
Standard deviation	E_1	25.05	0.09	16.88	14.00
	E_2	0.225	0.845	1.521	0.86
	η_1	5.70	7.65	137.13	50.16
	η_2	234.3	59.0	1448.8	581
Relative standard deviation [%]	E_1	40.36	0.18	44.94	28.49
	E_2	9.769	12.03	18.850	13.55
	η_1	47.18	47.15	100.25	64.86
	η_2	56.60	20.20	52.8	43

Table 5-2 Paramters ued to fit the Burger's model to the measured data for all experiment
The units of the parameters are: E_1=GPa, E_2=GPa, η_1=GPa/hr and $_{\eta_2}$=GPa/hr
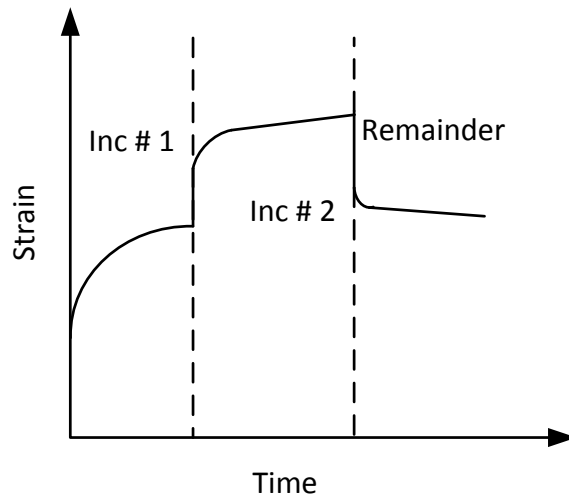
Figure 5-4 Explanation of position of parameter sets

In the bottom of Table 5-2 the average, standard deviation and relative standard deviation of the four different parameters are listed for the three different sets of parameters. In addition to the average of these three sets are listed. The relative standard deviation gives the best premise to compare the precision of the different parameters. One can see that the absolute range of the parameters goes somewhat outside the initially intended range of the parameters obtained from experiment and curve fitting from preceding Specialization Project. The statistical parameters show that the relative standard deviations are smaller for the elastic parameters than for the viscous parameters. However, this does not actually mean the viscous parameters of the model and the rock deviates more than the elastic parameters do. Rather the elastic parameters have the greatest impact of the "position" of the model, relative to the measured data. As seen, E_2 for Inc # 1 is very consistent and the relative standard deviation is small. Also the average value of the parameter is very close to the average of the measured values from the UCS test, of 2.02 GPa. This is a platitude since the only property separating the two parameters is that E_2 is calculated form the entire load phase, while Young's modulus is calculated from a linear tangent.

It should be noted that the population of parameters is small and the uncertainty coupled to the statistical indicators is expected to be high due to this fact. Nevertheless the indicators are included since they can show some initial trends.

5.1.2 Investigation of parameter dependency

When the Burger's model was fitted to the measured data, the elastic parameter of the Maxwell element showed indications of having impact on the precision of the fit. In order to check the influence of the elastic parameter, experiment on core sample 313_02_12 has been chosen to be investigated. The instantaneous elastic parameter of the Maxwell substance, E_2, seemed to be the parameter having the greatest impact between hold periods. Due to this fact the free variables chosen were: E_1, $E_{2 \, Drop \, \# \, 1}$ to $E_{2 \, Drop \, \# \, 8}$, η_1 and η_2. The additional free variables was used was to check whether the shape of the model curve would be improved. Three different cases were tested: three set of parameters, two set of parameters and one set of parameters

In order to obtain a good measure for comparison between the measured data and the model, as well as between experiments, the data was to be normalized. The reference point for the deformation is set at the first indication of transient response (instantaneous elastic response is left out) after the stress is changed. The current deformation in this point is deducted from the time dependent deformation, resetting the deformation. As for the deformation the time is reset at every stress change, on the same line as the deformation is reset.

For the first case the model was fitted to the Remainder (explained in Figure 5-4) with one set of parameters. Figure 5-5 to Figure 5-7 show the results of the fitted models compared to the measured data, the measured data and the model is visualized as solid and dashed line respectively. Emphasizing that the scale of the axis is very small compared to the total strain in the investigated area, 2.4 %[6], the fit of the model is actually very good. In the start the effect of the initial loading overshadows the effect of the first and second drop in stress seen in Figure 5-5, where the stress is increasing. As can be seen the shape of the first curves does not fit particularly well. This misfit becomes smaller for the rest of the hold periods where fit is very good, as seen in Figure 5-6 and Figure 5-7. The parameters used to fit the curves are in Table 5-3. Table 5-4 shows that $E_{2 \, Drop \, \# \, X}$ decreases as function of time, which also implies that the magnitude of the instantaneous strain recovery increases. E_2 is strongly related to Young's modulus, which means that Young's modulus is also decreasing. This coincides with the fact that Young's modulus should decrease as creep progresses.

---

[6]Compared to the range of the strain, [6.80,7.65]

E$_{2 \text{ Drop \# 1}}$	10.416	E$_{2 \text{ Drop \# 5}}$	8.640	E$_1$	46.388
E$_{2 \text{ Drop \# 2}}$	10.416	E$_{2 \text{ Drop \# 6}}$	8.288	E$_2$	10.416
E$_{2 \text{ Drop \# 3}}$	9.358	E$_{2 \text{ Drop \# 7}}$	7.677	η_1	50.842
E$_{2 \text{ Drop \# 4}}$	9.040	E$_{2 \text{ Drop \# 8}}$	7.264	η_2	1555.3

Table 5-3 The parameters used ot fit the the models in Figure 5-5 to Figure 5-7
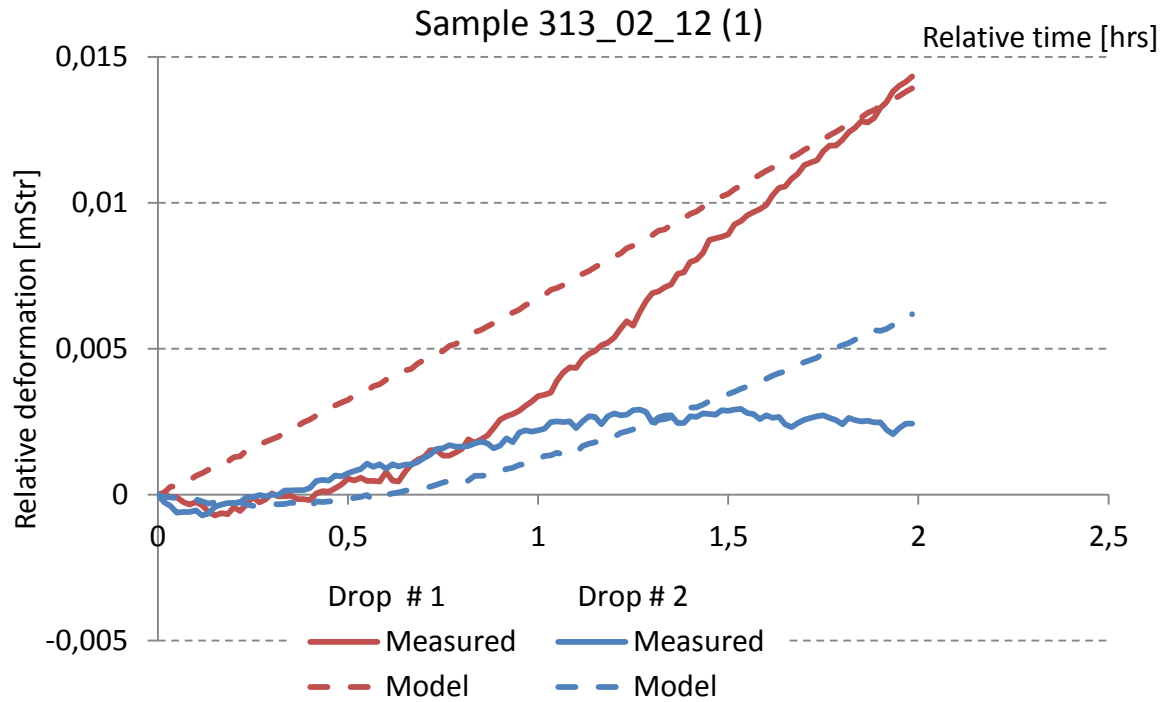
Figure 5-5 Normalized deformation for two hold periods after a decrease in stress
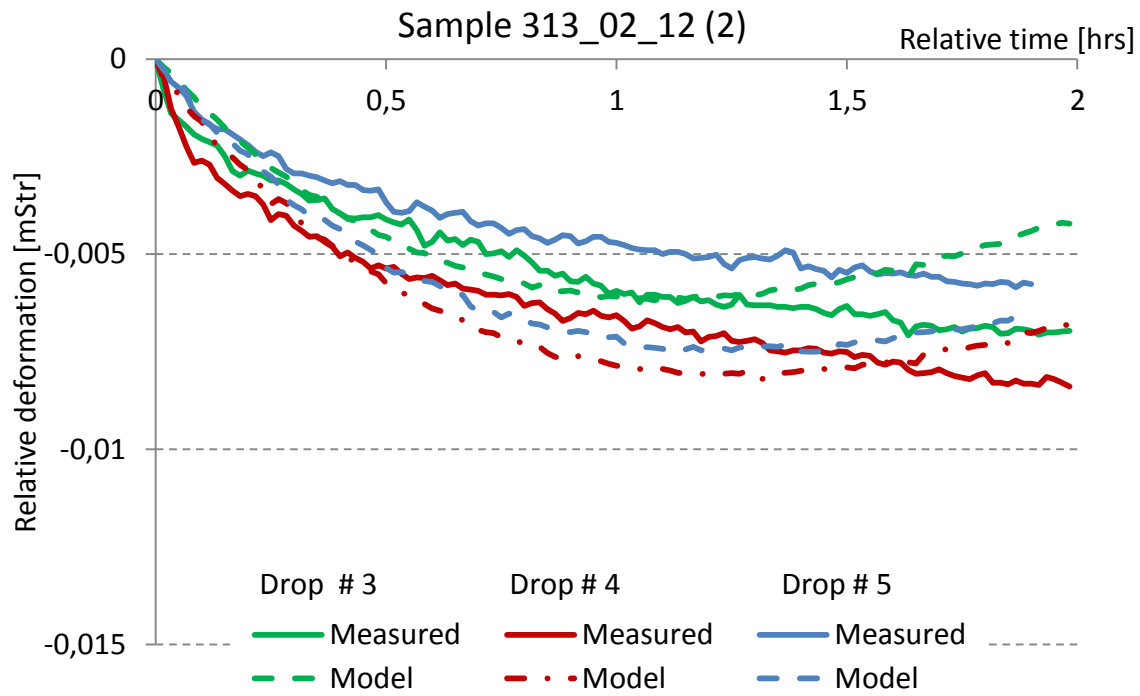
Figure 5-6 Normalized deformation for three hold periods after a decrease in stress
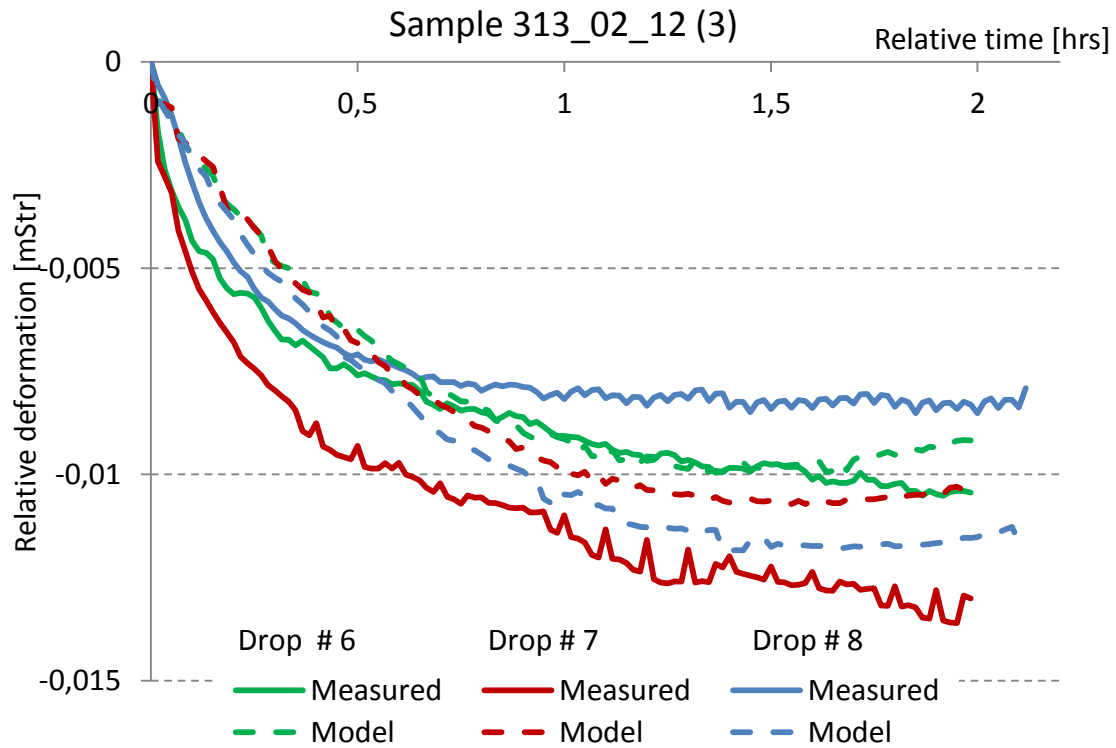
Figure 5-7 Normalized deformation for three hold periods after a decrease in stress

In the second case the set of parameters adjusting the Remainder in the previous case, is also applied to the hold period after the last increase in stress. As for the previous case E_1, $E_{2\,Drop\,\#\,1}$ to $E_{2\,Drop\,\#\,8}$, η_1 and η_2 are set as free variables, but in this case $E_{2\,Inc\,\#\,2}$ was also included. Figure 5-8 to Figure 5-10 shows that the model still fit the measured data reasonably well, although not as well as for the previous case. Considering the scale of the graphs being very small, the fit is very good if the whole interval is considered at the same time. Table 5-4 show the parameters used to fit the model for the second case. Comparing the parameters for the second and first case, the same trends can be seen for E_2.

$E_{2\,Drop\,\#\,1}$	10.680	$E_{2\,Drop\,\#\,5}$	8.887	E_1	37.019
$E_{2\,Drop\,\#\,2}$	10.695	$E_{2\,Drop\,\#\,6}$	8.535	$E_{2,0}$	10.695
$E_{2\,Drop\,\#\,3}$	9.545	$E_{2\,Drop\,\#\,7}$	7.890	η_1	26.982
$E_{2\,Drop\,\#\,4}$	9.336	$E_{2\,Drop\,\#\,8}$	7.467	η_2	1348.0

Table 5-4 The parameters used ot fit the the model in Figure 5-8 to Figure 5-10
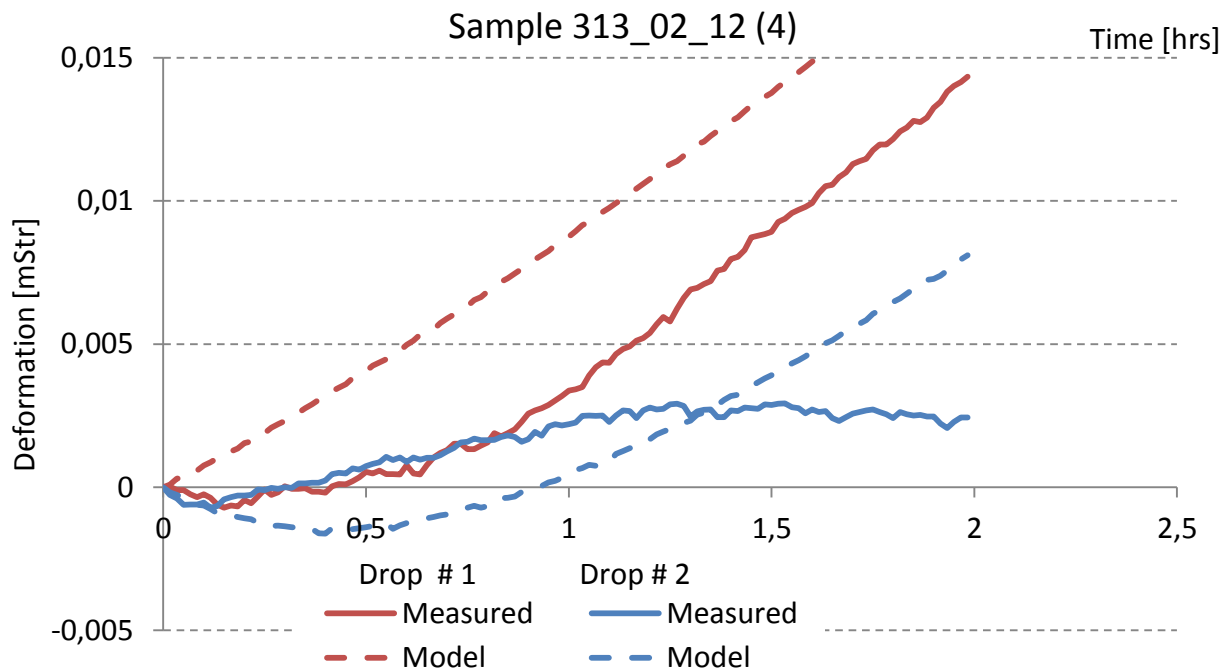
Figure 5-8 Normalized deformation for two hold periods after a decrease in stress
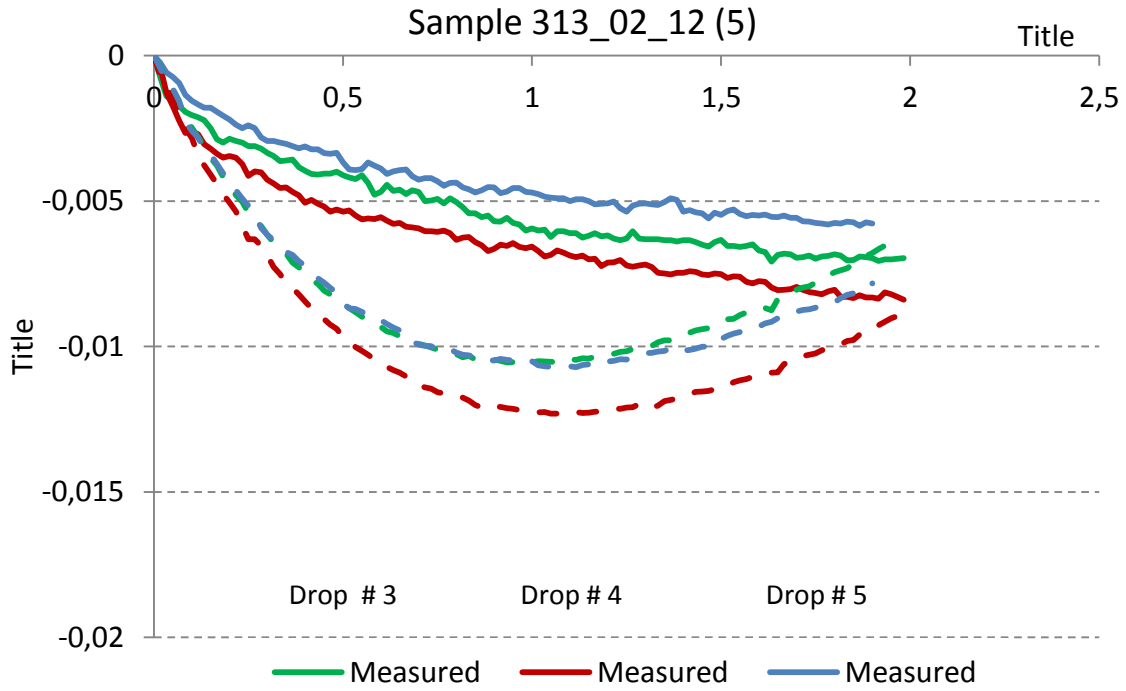
Figure 5-9 Normalized deformation for three hold periods after a decrease in stress
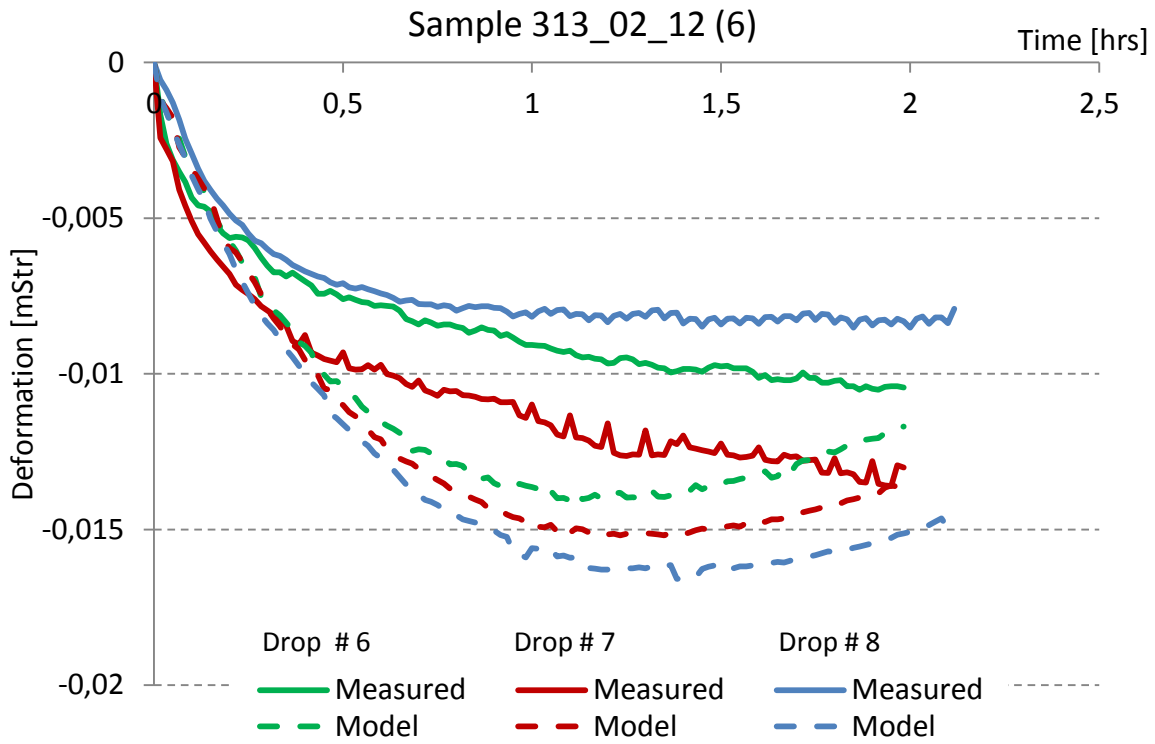
Figure 5-10 Normalized deformation for three hold periods after a decrease in stress

The third case was tested with one set of parameters (E_1, η_1 and η_2) for all hold period, while E_2 was different between hold periods. The resulting model using these set of criteria does not fit the measured data as well as the two previous cases, which is natural since there are fewer free parameters. The resulting plot of the measured data vs. the model can be seen in Figure 5-11 and the parameters used can be seen in Table 5-5. The figure shows that the model falls relatively far off from the measured data.
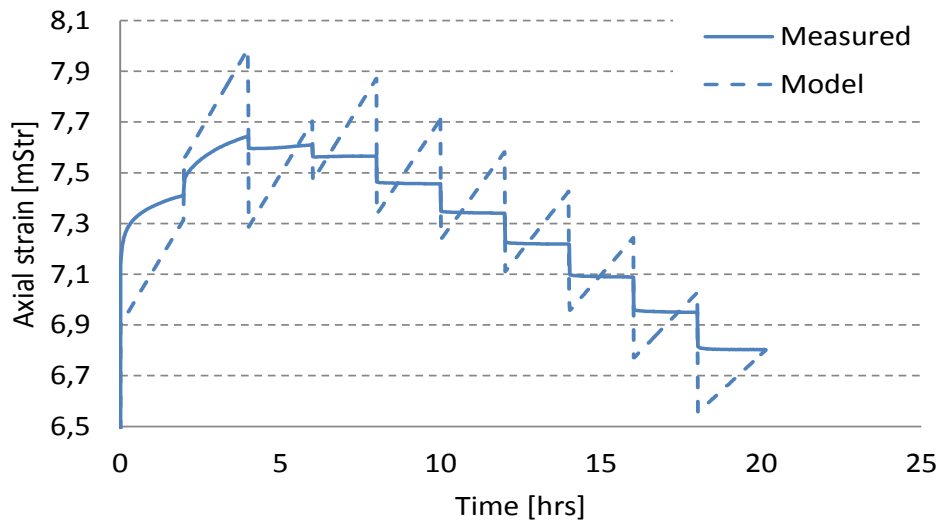
Figure 5-11Comparison of measured data and model when one set of parameters (E_1, η_1 and η_2) is used for the entire experiment. E_2 is varying between hold periods

$E_{2\ Drop\ \#\ 1}$	1.388	$E_{2\ Drop\ \#\ 5}$	0.000	E_1	0.0001
$E_{2\ Drop\ \#\ 2}$	0.000	$E_{2\ Drop\ \#\ 6}$	0.000	$E_{2,0}$	2.1019
$E_{2\ Drop\ \#\ 3}$	0.242	$E_{2\ Drop\ \#\ 7}$	0.000	η_1	72.252
$E_{2\ Drop\ \#\ 4}$	0.000	$E_{2\ Drop\ \#\ 8}$	0.000	η_2	1511.6

Table 5-5 The parameters used ot fit the the model in Figure 5-11

5.1.3 Boltzmann Superposition

During the early stages of the thesis an alternate solution to the Burger's model was derived by the use of combinations of the analytical solutions to the Burger's model. The principle was to combine each stress increment to make up the full model. By doing this it is possible to test several combinations of the active area of which the set of parameters is adjusted to.

As opposed to the finite difference method the Boltzmann Superposition principle makes it possible to test two different sets of parameters on positive and negative contributor of the model, mentioned in chapter 2.3.1.2. Since the method is somewhat cumbersome to implement in Excel only one of the experiments will be examined; 313_02_12.

Several different combination and configurations was tested to check whether the Superposition principle was able to predict the deformation better than the regular finite difference method. One of the solutions was obtained using different parameters for ε_+ and ε_-, described in chapter 2.3.1.2. The model obtained from this does not fit the measured data particularly well compared to the model fitted by the use of the finite difference method. The model fitted to the measured data is seen in Figure 5-12. The figure shows that the transient response during the hold period does not fit the measured data.

No other combinations using the same or higher number of free variables yielded any better results than what is presented in Figure 5-12. Due to this, the Boltzmann Superposition will not be discussed further.
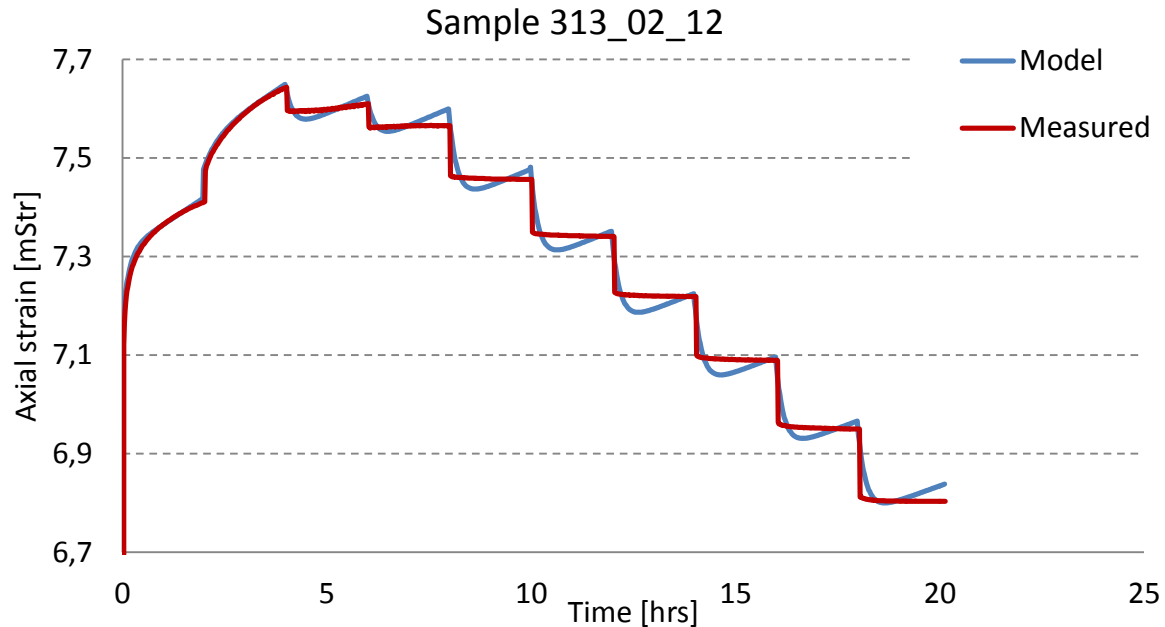
Figure 5-12 Burger's model fitted by the use of Boltzmanns Superpoistion principle

5.1.4 Summary

The Burger's model is able to produce good overall predictions for deformation if several sets of parameters are used. Fine details during transient recovery in hold periods following unloading cannot be reproduced using only one set of parameters for the entire interval. If E_2 is set as a free variable, changing between hold periods, a good fit can be produced.

If one set of parameters is used to predict the entire interval, the model falls far off the measured data after the first hold period. This is believed to be related to varying plastic contribution between the intervals. Even though the Burger's model is able to predict rock behavior under certain conditions, the extensive use of free variables, suggest that model is not fit for predicting creep in Castlegate. Another disproving argument is that the model is being used outside its physical range of validity, which is to predict the behavior of a substance obeying viscoelastic principles.

5.2 FORMEL model

The current FORMEL model has not been developed to model unloading of stress to this data. Due to this the FORMEL model has only been fitted to the first hold period of the measured data. Nor was the model able to predict the stress during the loading period, using the finite difference method. Therefore the model has only been fitted to the transient and steady state intervals. Values for E* and q was obtained from the experiments, and were 2.02 GPa and 105 Str^{-1} respectively. Only three free variables was used when the model was fitted.

The parameters used for fitting the FORMEL have been summarized in Table 5-6. The table shows that the parameters are relatively consistent compared to the results from the Specialization course, found in Appendix VI. None of the parameters are more than 65.2 % off, if relative standard deviations are used as a measure. Compared to the Burgers' model the FORMEL model is fitted using fewer free variables. On the other side the FORMEL model is only fitted to the first interval.

	τ	n	der
313_02_04	6,37E-05	0,66	2,64E-05
313_02_08	8,10E-05	0,72	1,05E-05
313_02_09	2,66E-05	0,82	1,97E-05
313_02_12	2,47E-07	1,25	2,29E-05
313_02_12	4,46E-05	0,86	1,02E-05
Average	4,32E-05	0,86	1,79E-05
std.dev	2,82E-05	0,21	6,54E-06
Relative std.dev	65,17	23,86	36,49

Table 5-6 Overview of parameters used to fit the FORMEL model

5.3 P-wave velocities

5.3.1 Instantaneous changes

As described in the theory the P-wave velocity is depending on the Young's modulus of the rock, which in turn is depending on crack density described by equation 2-5. The crack density is depending on stress, and cracks tend to close as stress is applied. Thus when stress is applied the P-wave velocity is expected to increase, while it will decrease when stress is removed. This instant effect can be observed for almost all stress increases and decreases. However unexpected responses are seen in Figure 4-14 and Figure 4-18, when the stress is increased from 14-15 MPa and 14.5-15 MPa in experiment 313_02_09 and 313_02_12 respectively. For these two stress changes the P-wave velocities remain more or less constant. This may have been caused by pure elastic response, where no cracks are either being closed or created. Or a mix of cracks being created and closing at the same rate during the short period where the stress is increased.

If the response of the P-wave velocity during the period of loading is investigated, one can see that the instant elastic response changes between drops in stress. The magnitude of change in P-wave velocity increases for every cycle. This coincides with the observation of the instant strain recovery for experiment 313_02_12, where the magnitude of the strain recovery increases for every drop in stress. The variations in instant strain recovery for experiment 313_02_12 are seen in Table 5-8. The strain recovery increases for every step, while the stress decrease is constant for all steps. Consquently the Young's modulus decreases for each drop in stress. This coincides with the parameters found in the case study for the Burger's model, where the static Young's modulus decreased. If Young's modulus is used to explain the increasing change in P-wave velocity, it would have to increase. However the Young's modulus related to P-waves is the dynamic modulus, explained in chapter 2.2.3.

	ΔVp [m/s]		ΔVp [m/s]
Drop 1	8.00	Drop 5	27.0
Drop 2	10.0	Drop 6	32.0
Drop 3	23.0	Drop 7	36.5
Drop 4	23.0	Drop 8	41.0

Table 5-7 Instant decrease in P-wave velocity caused by deacrease in stress for experiment 313_02_12

	Δd [mStr]		Δd [mStr]
Drop 1	0.043	Drop 5	0.115
Drop 2	0.05	Drop 6	0.125
Drop 3	0.105	Drop 7	0.13
Drop 4	0.107	Drop 8	0.15

*Table 5-8 Instant decrease in strain (expansion) caused
by deacrease in stress for experiment 313_02_12*

5.3.2 Time dependent effects

During hold periods following an increase in stress the P-wave velocity is expected to decrease as a function of increasing strain, as mentioned in chapter 2.2.2. This effect is seen for most experiments visualized in Figure 5-13, where the velocities decrease as a function of increasing strain. The same effect was observed by Fjær (2006). A possible explanation for the decrease in P-wave velocity can be that new cracks are formed, which is also one of the root causes of the induced strain.

Figure 5-14 show that the P-wave velocities during the reloading cycles of experiment 313_02_04 does coincide with the previously mentioned observations. The P-wave velocity increases as strain increases, which is the exact opposite of the previously mentioned observations. However, distinguishing factors separates these reloading cycles from the mentioned hold periods; the stress applied does not exceed the stress level applied during the first hold period. Since the wave velocity is increasing during the hold periods following a reloading of the sample, an increase in Young's modulus can also be assumed. If one assumes that cracks density is the factor changing the elastic moduli, the cracks have to close during the hold period. During the first period the wave velocity is decreasing, which would imply that the crack density increases, if the same line of argumentation is used here. One hypothesis that may explain this observation is that cracks are forming during the first hold period, while a transient process of closing these cracks can be occurring during the reloading cycles.
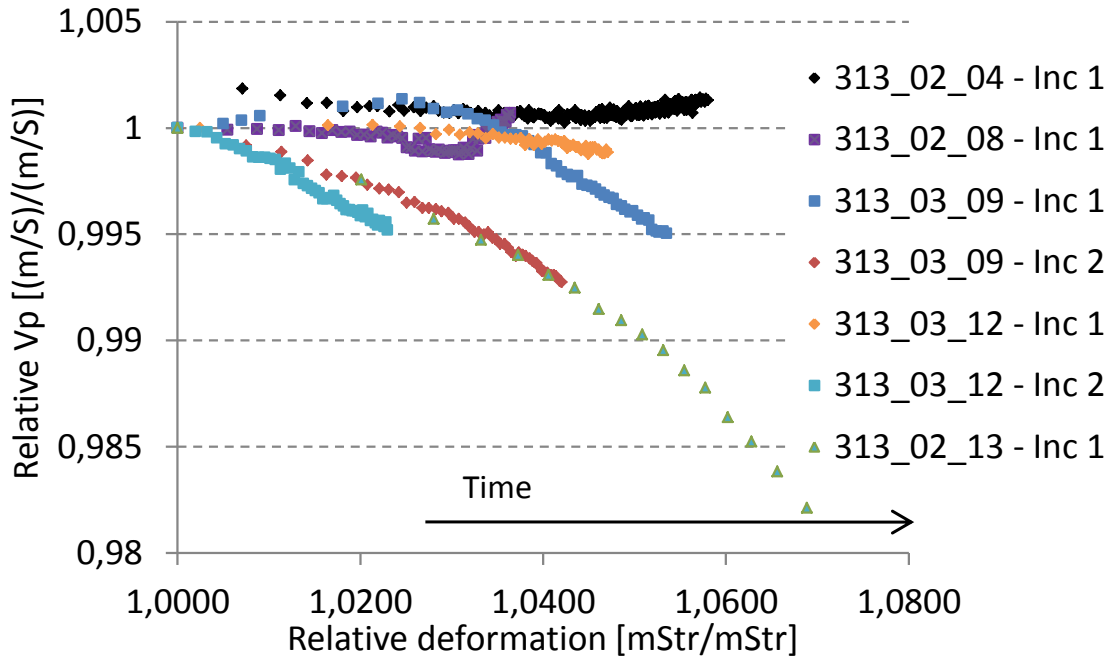
Figure 5-13 Relative velocity and deformation for the first hold period for 5 experiments
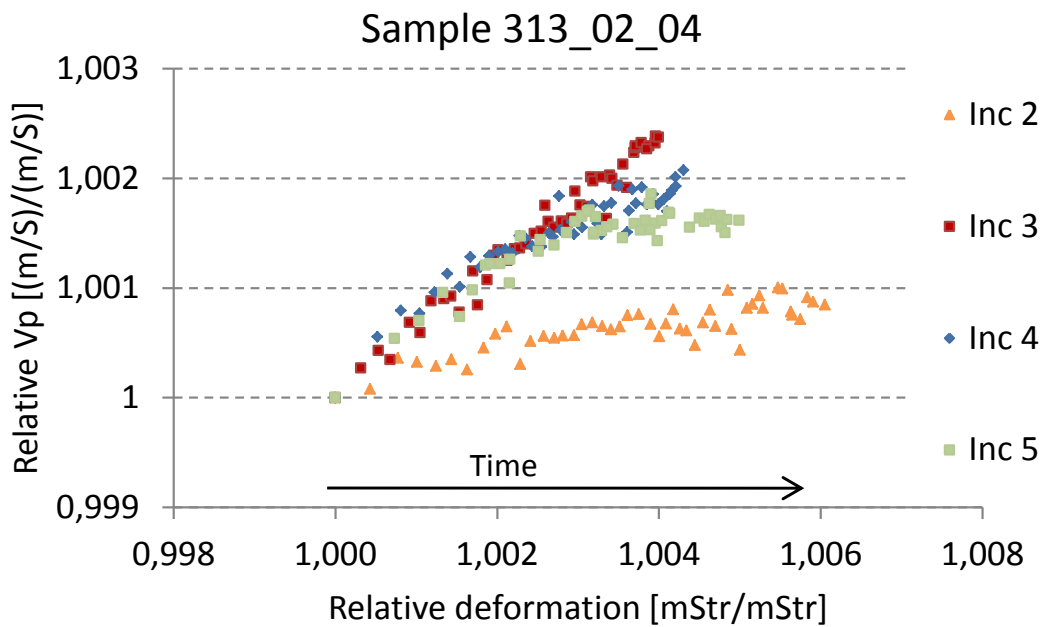
Figure 5-14 Relative velocity and strain for the hold periods following increases in stress

Figure 5-15 show the relative P-wave velocities plotted against the relative deformation during the hold periods following the 6 last decreases in stress for experiment 313_02_12. Since the stress has been reduced before the hold periods, the deformation is decreasing, meaning that the core is expanding. This means that the "time" is progressing in the opposite direction compared to Figure 5-13, as indicated by the arrows in the figures. If the two figures are compared, it is clear that the points from both plots follow the same trend. This would also suggest that the same mechanisms are active in the process, only occurring in reverse direction. Although only experiment 313_02_012 has been highlighted in this paragraph, the same trends can also be observed for the rest of the experiments. These plots have been attached in Appendix IV, and can be found under the "Acoustic" section of each individual experiment.
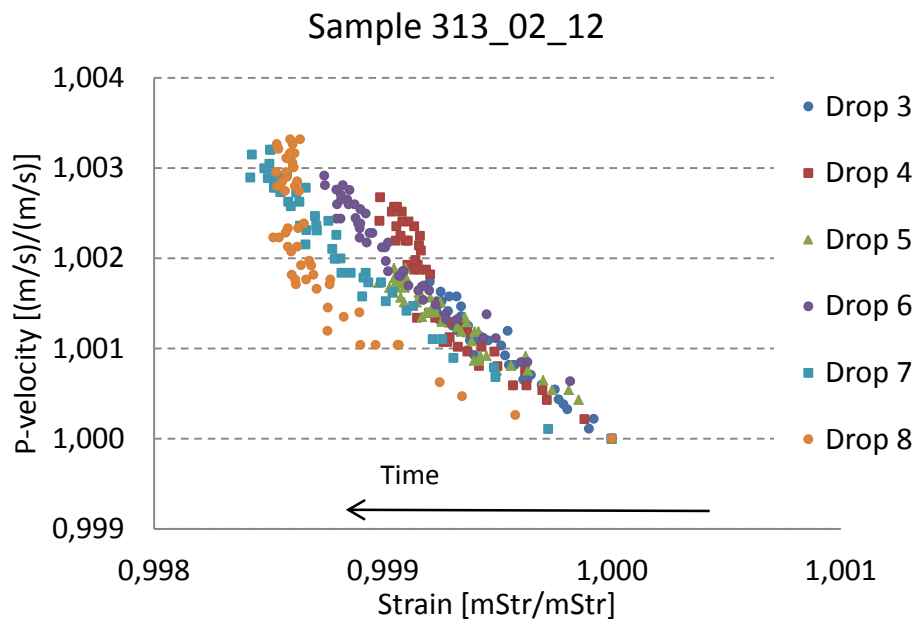
Figure 5-15 Relative velocity and strain for the hold periods following increases in stress

When the stress is decreased the cracks laying normal to the load direction will open immediately as a "spring". Trying to explain the effects seen when the crack density is increased a theory has been made:

In order to explain the effects of the P-wave velocities, a thought experiment has been suggested:

- A uniaxial load is applied to a core sample, which creates local shear forces within the rock, caused by the nature of heterogenic matrix of the rock
- Wing cracks are created when shear stresses along slip surface overcome the static friction between the two surfaces. In the end of each crack a wing crack will be created. If the shear sliding occurs along the vertical axis of the core sample, wing cracks would open perpendicular to this direction. This means that a new crack has been opened perpendicular to the direction of the P-wave propagation, thus reducing the P-wave velocity.

Unloading of the rock

- All or some of the load is removed from the sample which causes the rock to expand and local shear forces will be created within the rock, also along the surfaces where slip occurred during unloading. However, the stress could be distributed in another way at unloading compared to loading
- The distribution of the shear stress is time-dependent and certain local stress concentrations build up, which means that the shear stress is not directly transferred to the slip surfaces where slip occurred during the loading phase
- Shear stress builds up along the slip surface in the opposite direction compared to the unloading phase. Eventually the force acting along the slip surface exceeds the static friction and the surfaces move back to the original place (as oposed to before the first loading cycle)
- The motion of the slip surfaces causes the wing cracks to close which means that the crack density decreases
- This should lead to an increase in the P-wave velocity which could explain the increase in wave velocity after the sample is unloaded

5.4 Sources of error

5.4.1 Temperature effects

In the series of experiments performed in the preceding "Specialization Project", the temperature had a large impact on the deformation data. The reason behind this effect was not known in detail, but probably caused by a mix of reason, amongst them; stress changes caused by thermal expansion, large variations in temperature caused by nearby air-condition and temperature dependency of the LVDT's. Due to this fact the new series of experiment was performed in another room, with another load frame and different LVDT sensor. The combined effect of this resulted in high quality measurements without temperature interferences. The maximum temperature variation during one experiment was 0.9 ° C.

5.4.2 Parallelism of the core sample

If the surfaces between the plug and the load frame are not parallel, the stress transmitted through the plug will not be evenly distributed. This can lead to increased local stresses in parts of the samples leading to higher creep in these areas. In turn this can lead to early collapse of the sample if one side of the sample is subjected to higher stress concentration than the rest of the sample.

Furthermore non parallel surfaces can lead to dissimilar readings of the two LVDT's. If the sides of the core are not parallel the initial recorded deformation can yield totally different values. In order to correct for this, the values of the two deformation reading can be averaged. If extra LVDT's where installed the average would be more likely to represent the true value of the deformation.

5.4.3 Noise from the LVDT

The precision of the LVDT is listed to be unlimited. However the axial displacement caused by the stress changes is very small. For many of the stress steps the magnitude of the transient displacement response is only 0.01 mStr, which is about 0.5 µm. The raw data contains noise of a magnitude higher than the total transient displacement response. The sample rate of the LVDT is 5 Hz for all the experiments. Since the sample rate is very high, averaging the raw measured data was used. This was done by forward-backward averaging, which cancelled out the noise and showed clear consisted trends for the deformation data.

5.4.4 Surface area

Loads are applied to the core sample, causing an axial compaction, leading to higher density. Another effect is that the core expands circumferentially. This means that the surface are of the core is increased, which means that the stress applied will be reduced, assuming the surface of the core can expand freely along the surface of the piston. This might not be the case since friction between the core and the piston is acting against this motion.

5.5 Future work

When the core sample is reloaded to the initial peak stress the P-wave velocity increase as a function of both time and strain. This stands in contrast to what is seen for the initial loading where the P-wave velocity drops as a function of strain. The drop in P-wave velocity can be explained by the formation of new micro cracks or re-opening of existing cracks. In order to further investigate the effect seen in experiment 313_02_04, it would be interesting seeing whether the wave velocity would drop in hold periods after reloading if the stress is held for a longer period. For future experiments the number of AE at the top of a stress cycles should be recorded to find any cause explaining the increase in P-wave velocity, when the stress is reloaded to 15 MPa.

6 Conclusion

A series of experiments have successfully been performed using different stress paths and peak loads, resulting in 5 data sets of high quality. Based on the experimental data and creep related models the following finding and deductions have been made:

- The Burger's model is able to produce good overall predictions for deformation if a sufficient number of free variable are used.

- If only one set of parameters is used, the Burger's model is unable to predict deformation of experiments using stress paths with loading, unloading and reloading.

- The use of Boltzmann superposition principle does not provide any further application to the Burger's model compared to finite difference

- It has been confirmed that the P-wave velocity decreases as a function of increasing strain (compaction) in periods of constant stress, after an increase in stress.

- The P-wave velocity has been found to increases as a function of decreasing strain (expansion), in periods of constant stress, following a decrease in stress. This means that the processes occurring can be similar, and occurring in the opposite direction depending on the stress change.

- The recovery of the deformation when stress is unloaded does not match the elastic and transient response predicted but the viscosity model. The elastic recovery is smaller and the transient recovery is smaller than expected or absent.

Bibliography

Abell, B., & Pyrak-Nolte, L. (2014). Elastic waves that propagate along fracture intersections. *Geomechanics Symposium* . Minneapolis,MN USA: ARMA.

Applied Measurements. (No data). *How LVDTs Work*. Retrieved November 18, 2014, from http://www.lvdt.co.uk/how-lvdts-work/

Atkinson, B. (1982). Subcratical crack propagation in rocks: experimental results and applications. *Journal of Structural Geology Vol. 4 No. 1*, 41-56.

Bart, J., Kenter, C., & Munster, H. (2001). Core-based determination of in-situ magnitudes. *Rock Mechanics in the National Interest*, 1353-1360.

Charit, I., & Murty, K. (2008). Creep behavior of niobium-modified zirconium alloys. *Journal of Nuclear Marericals 374*, 354-363.

Chester, J., Lenz, S., Chester, F., & Lang, R. (2004). Mechanisms of compaction of quartz sand at diagenetic conditions. *Earth and Planetary Science Letters 220*, 435-451.

Dusseault et al. (2004b). Drilling Trhough Salt: Constitutive Behaviour and Drilling Strategies. *ARMA/NARMS 04-608*.

Eberhard, E., Stead, D., & Morrison, T. (2007). Rock Mechanics: Meeting Society's Challenges and Demands, Two Volume Set. *Proceedings of the 1st Canada-US Rock Mechanics Symposium* (p. 1712). Vancouver: CRC Press.

Fintland, T. (2011). *Measurements of Young's Modulus on Rock Samples at Small Amplitude and Low Frequency*. Trondheim: NTNU.

Fjær, E. (1999). Static and dynamic moduli for weak sandstones. *Rock Mechanics for Industry, Amadei, Kranz, Scoot & Smealie*, 675-681.

Fjær, E. (2006). Modeling the stress dependence of elastic wave velocities in soft rocks. *The 41st U.S. Symposium on Rock Mechanics (USRMS): "50 Years of Rock Mechanics - Landmarks and Future Challenges"*. Golden, CO: ARMA.

Fjær, E., Holt, R., Horsrud, P., Raaen, A., & Risnes, R. (2008). *Petroleum Related Rock Mechanics 2nd edt.* Oxford: Elsevier B.V.

Fjær, E., Holt, R., Horsrud, P., Raaen, A., & Risnes, R. (2008). *Petroleum Related Rock Mechanics 2nd edt.* Oxford: Elsevier B.V.

Fjær, E., Larsen, I., Holt, R., & Bauer, A. (2014). A creepy model for creep. *ARMA-14-7398*.

Günther, R., Salzer, K., & Popp, T. (2010). Advanced Strain – Hardening Approach Constitutive model for rock salt describing transient, stationary and accelerated creep and dilatancy. *44 th - US Rock Mechanics Symposium.* Salt Lake City: ARMA.

Günther, R.-M., Salzer, K., & Popp, T. (2010). Advanced Strain – Hardening Approach. *US Rock Mechanics Symposium.* Salt Lake city: ARMA.

Heap, M. (2009). Creep: Time-dependent bittle deformatin in rocks. London: University Colledge.

Heiland, H., & Flor, M. (2006). Influence of Rock Failure Characteristics on Sanding Behaviour: Analysis of Reservoir Sandstones From the Norwegian Sea. *SPE International Symposium and Exhibition on Formation Damage Control.* Lafayette, LA: SPE 98315.

Hoek, P., Kooijman, A., Bree, P., Kenter, C., Zheng, Z., & Khodaverdian, M. (2000). Horizontal-Wellbore Stability and Sand. *SPE Drill. & Completion 15*, 274-283.

Holt, R., Brignoli, M., Fjær, E., Unander, T., & Kenter, C. (1994). Core damage effects on compaction behaviour. *Rock Mechanics in Petroleum Engineering Conference* (pp. 55-62). Delft: SPE.

Holt, R., Pestman, B., & Kenter, C. (2001). Use of a discrete model to assess feasibility of core based stress determination. *Rock Mechanics in the National Interest*, 1361-1366.

Hudson, J., & Harrison, J. (2000). *ENGINEERING ROCK MECHANICS - AN INTRODUCTION TO THE PRINCIPLES.* Oxford: Elsevier.

Jaeger, J., Cook, N., & Zimmerman, R. (2007). *Fundamentals of Rock Mechanics 4th ed.* Malden, Mass.: Blackwell.

84

King, M. (1969). Static And Dynamic Elastic Moduli of Rocks under Pressure. *The 11th U.S. Symposium on Rock Mechanics (USRMS)* (pp. 329-351). Berkeley, California: ARMA.

Kristensen, V. (2013). *Visco-elastic response of thermoplastics.* Trondheim: NTNU.

Macro sensors. (2014, March 11). *Macro sensors blog*. Retrieved November 18, 2014, from http://macrosensors.com/blog/view-entry/Consider-These-Temperature-Effects-When-Specifying/48/#.VGsdb_mG8-M

Maranini, E., & Brignoli, M. (1999). Creep behaviour of a week rock: experimental characterization. *International Journal of Rock Mechanics and Mining Science 36*, 127-138.

Montmayeur, H., & Graves, R. (1985). Prediction of Static Elastic/Mechanical Properties of and Unconsolidated Sands From Acoustic Measurements: Basic Measurements. *e 60fh Annual Technical Conference and Exhibitionof the Society of Petroleum Engineers* (pp. 1-12). Las Vegas: SPE.

Montmayeur, H., & Graves, R. (1986). Prediction of Static Elastic/Mechanical Properties of and Unconsolidated Sands From Acoustic Measurements: Correlations. *e 61st Annual Technical Conference and Exhibitionof the Society of Petroleum Engineers* (pp. 1-12). New Orleans: SPE.

MTS Systems Corporation. (No Date). *MTS Insight Material Testing Systems Product Information.* Eden Prairie, MN: MTS Systems Corporation.

Olsen, J. R. (2014). Creep investigation: Experiments and Model Fitting. Trondheim.

Omega. (2015, March 21). *Omega*. Retrieved from Strain Gauges: http://www.omega.com/prodinfo/straingages.html

Physics forum. (2009, September 25). *Physics forum*. Retrieved from https://www.physicsforums.com/threads/crack-nucleation.340384/

Pico Technology Limited. (2005). *USB TC-08 Temperature Logger User's Guide.* Retrieved from Pico Technology: http://www.picotech.com/document/pdf/usbtc08.en-7.pdf

Plona, T., & Cook, J. (1995). Effects of stress cycles on static and dynamic Young's moduli in Castlegate. *The 35th U.S. Symposium on Rock Mechanics (USRMS)* (pp. 155-160). Reno, Nevada: ARMA.

Raaen, A., Hovem, K., Jøranson, H., & Fjær, E. (1996). FORMEL: A Step Forward in Strength Logging. *SPE Annual Technical Conference and Exhibition* (pp. 439-445). Denver: SPE.

Roylance, D. (2001). *ENGINEERING VISCOELASTICITY*. Cambridge: Department of Materials Science and Engineering Massachusetts Institute of Technology.

Shen, B., & Rinne, M. (2007). A Fracture Mechanics Code For Modelling Sub-critical Crack Growth And Time Dependency. *Unknown* (pp. 1-8). Unknown: ARMA.

Stroisz, A., & Fjær, E. (2011). Nonlinear elastic wave propagation in Castlegate sandstone. *45th US Rock Mechanics/Geomechanics Symposium.* San Fransisco, CA: ARMA.

Tropea, C., Yarin, A., & Foss, J. (2007). *Springer Handbook of Experimental Fluid Mechanics.* Berlin, Heidelberg: Springer.

University of Minnesota. (2000, March 13). *Long term performance of polymers.* Retrieved from University of Minnesota: http://www.me.umn.edu/labs/composites/Projects/Polymer%20Heat%20Exchanger/Creep%20description.pdf

University of Nottingham. (n.d.). Polymer Engineering. *Viscoelasticity*. Retrieved from The University of Nottingham: http://www.nottingham.ac.uk/~eazacl/MM3POE/Viscoelasticity.pdf

Vishay Micro-Measurements. (2003, September 3). Data Book - Precision Strain Gauges.

Vishay Precision Group. (2015, March 21). *VPG | Performance Through Precision.* Retrieved from Vishay Precision Group: http://www.vishaypg.com/docs/11230/125ut.pdf

VPG & Micro-Measurements. (2010, Novemeber 14). The Three-Wire Quarter-Bridge Circuit. *Application Note TT-612*.

Appendix I. Derivation of strain equation for Burger's substance

Assuming the Maxwell and Kelvin-Voigt substances are two independent systems, meaning that the differential equation for the whole system can be divided into two systems and added using superposition. Some of the equations have already been presented in the main part, but will be repeated to provide a better overview.

Derivation from $0 < t < t_c$:

Maxwell

Boundary condition: $\varepsilon = \sigma/E \ for \ t = 0$

$$\frac{d\varepsilon}{dt} = \frac{\sigma}{\eta_1} + \frac{1}{E_1}\frac{d\sigma}{dt} \qquad \text{I-I}$$

$$\int d\varepsilon = \frac{1}{E_1}\int \frac{d\sigma}{dt}dt + \frac{\sigma}{\eta_1}\int dt \xrightarrow{yields} \varepsilon = \frac{\sigma}{E_1} + \frac{\sigma}{\eta_1}t + C \qquad \text{I-II}$$

Applying BC:

$$\frac{\sigma}{E_1} = \frac{\sigma}{E_1} + \frac{\sigma}{\eta_1} \times 0 + C = 0 \xrightarrow{yields} \boldsymbol{\varepsilon_M = \frac{\sigma}{E_1} + \frac{\sigma}{\eta_1}t} \qquad \text{I-III}$$

Kelvin-Voigt

Boundary condition: $\varepsilon = 0 \ for \ t = 0$

$$\sigma_0 = E_2\epsilon + \eta_2\frac{d\varepsilon}{dt} \qquad \text{I-IV}$$

$$\frac{1}{\eta_2}\int dt = \int \frac{d\varepsilon}{\sigma_0 - E_2\epsilon} \xrightarrow{yields} \varepsilon = \frac{\sigma_0}{E_2} - \frac{C}{E_2}e^{-\frac{E_2}{\eta_2}t}, \qquad \text{I-V}$$

Applying BC:

$$\frac{\sigma_0}{E_2} - \frac{C}{E_2} \times 1 = 0 \xrightarrow{yields} C = \sigma_0 \xrightarrow{yields} \boldsymbol{\varepsilon_{K-V} = \frac{\sigma_0}{E_2}\left(1 - e^{-\frac{E_2}{\eta_2}t}\right)} \qquad \text{I-VI}$$

Adding the bold expression in equation I- and I- yield:

$$\varepsilon_B = \varepsilon_M + \varepsilon_{K-V} = \frac{\sigma}{E_1} + \frac{\sigma_0}{E_2}\left(1 - e^{-\frac{E_2}{\eta_2}t}\right) + \frac{\sigma}{\eta_1}t \ ^7 \qquad \text{I-VII}$$

---

[7] B: Burgers – M:Maxwell – K-V: Kelvin-Voigt

Derivation from $t > t_c$:

<u>Maxwell</u>

Assuming the elastic deformation is reset the strain in the Maxwell substance is:

$$\varepsilon_M = \frac{\sigma}{\eta_1}t_c \; for \; t > t_c \qquad\qquad \text{I-VIII}$$

<u>Kelvin-Voigt</u>

Boundary condition: For $t = t_c, \varepsilon_{K-V} = \frac{\sigma_0}{E_2}\left(1 - e^{-\frac{E_2}{\eta_2}t_c}\right)$

$$0 = E_2\varepsilon_{K-V} + \eta_2\frac{d\varepsilon_{K-V}}{dt} \qquad\qquad \text{I-IX}$$

$$-\frac{E_2}{\eta_2}\int dt = \int\frac{d\varepsilon_{K-V}}{\varepsilon_{K-V}} \xrightarrow{yields} \varepsilon_{K-V} = Ce^{-\frac{E_2}{\eta_2}t}, \qquad\qquad \text{I-X}$$

Applying BC:

$$\varepsilon_{K-V}(t_c) = Ce^{-\frac{E_2}{\eta_2}t_c} = \frac{\sigma_0}{E_2}\left(1 - e^{-\frac{E_2}{\eta_2}t_c}\right) \div e^{-\frac{E_2}{\eta_2}t_c} \xrightarrow{yields} C = \frac{\sigma_0}{E_2}\left(e^{\frac{E_2}{\eta_2}t_c} - 1\right) \qquad \text{I-XI}$$

which giving the following expression for Kelvin-Voigt recovery:

$$\boldsymbol{\varepsilon_{K-V} = \frac{\sigma_0}{E_2}\left(e^{\frac{E_2}{\eta_2}t_c} - 1\right)e^{-\frac{E_2}{\eta_2}t} \; for \; t > t_c} \qquad\qquad \text{I-XII}$$

Adding the bold expression in equation I- and I-I- yield:

$$\boldsymbol{\varepsilon_B = \varepsilon_M + \varepsilon_{K-V} = \frac{\sigma}{E_1} + \frac{\sigma_0}{E_2}\left(e^{\frac{E_2}{\eta_2}t_c} - 1\right)e^{-\frac{E_2}{\eta_2}t} + \frac{\sigma}{\eta_1}t} \; [8] \qquad \text{I-XIII}$$

---

[8] B: Burgers – M:Maxwell – K-V: Kelvin-Voigt

II

Appendix II. Calibration of LVDT and core data
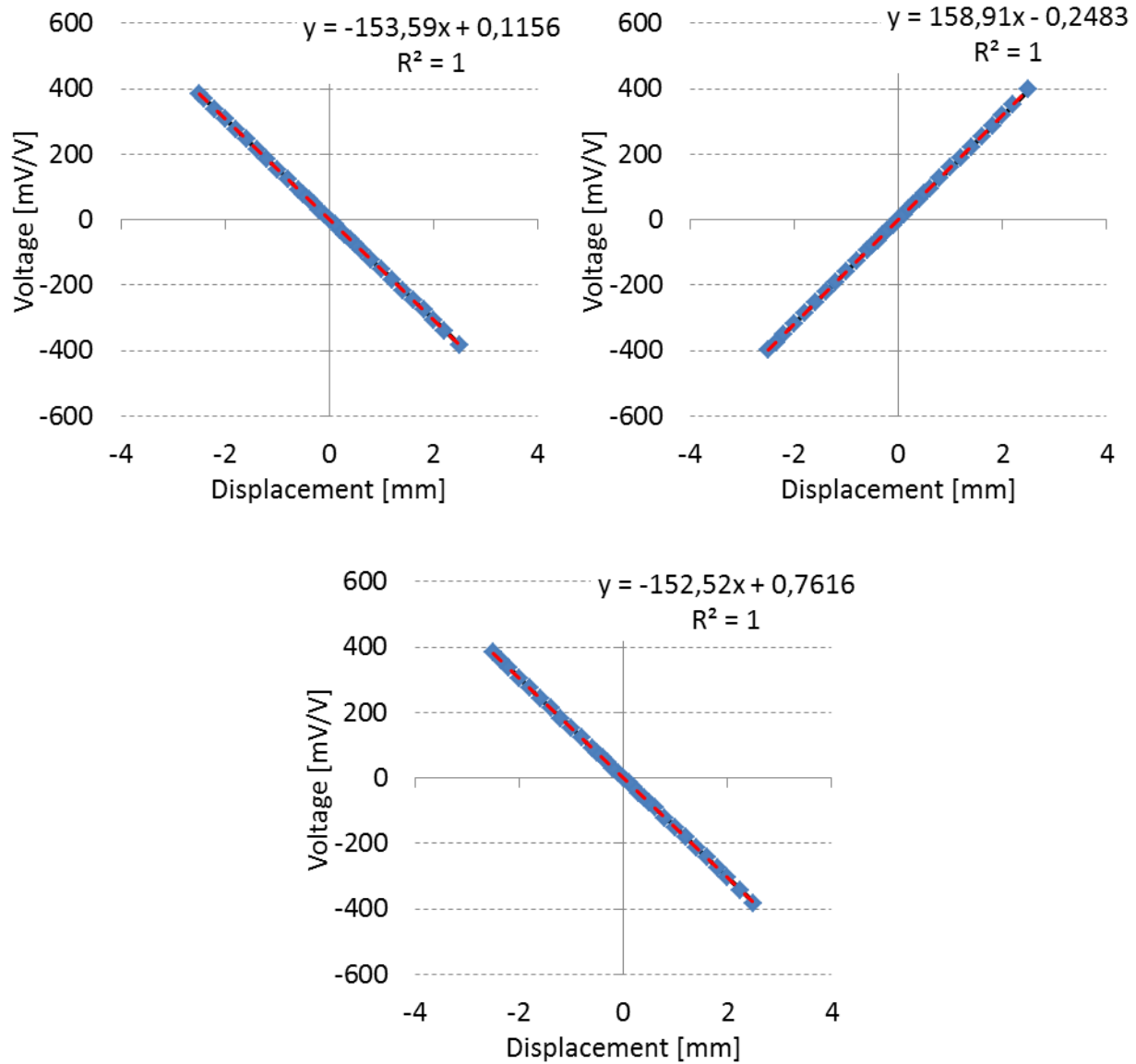
Figure II-I – Plot of the calibration of the

Appendix III. Equipment and Core data

Sample	Mass	L1	L2	L avg	L std.dev	D1	D2	D3	D4	D avg	D std.dev	Density
[#]	[g]	[mm]	[mm]	[mm]	[mm]	[mm]	[mm]	[mm]	[mm]	[mm]	[mm]	[g/cm3]
313_02_01	48,896	51,8	52,07	51,94	0,19	25,05	25,03	25,02	25,02	25,03	0,01	1,9103
313_02_02	48,882	51,83	51,96	51,90	0,09	25,02	25,01	25,01	24,99	25,01	0,01	1,9158
313_02_03	48,898	51,82	51,84	51,83	0,01	24,99	25,01	25,01	25,01	25,01	0,01	1,9235
313_02_04	48,728	51,82	51,83	51,83	0,01	24,98	25	25,01	25	25,00	0,01	1,9185
313_02_05	48,855	51,83	51,82	51,83	0,01	25,01	25,02	25	24,99	25,01	0,01	1,9189
313_02_06	48,945	51,86	51,86	51,86	0,00	24,98	24,98	24,95	25	24,98	0,02	1,9258
313_02_07	48,631	51,64	51,64	51,64	0,00	25,01	25,01	25,01	25,02	25,01	0,00	1,9169
313_02_08	48,819	51,78	51,78	51,78	0,00	25,01	25,02	25	25,01	25,01	0,01	1,9192
313_02_09	48,72	51,64	51,64	51,64	0,00	25,02	25,03	25,02	25,03	25,03	0,01	1,9189
313_02_10	48,273	51,23	51,22	51,23	0,01	24,94	24,95	24,94	24,95	24,95	0,00	1,9290
313_02_11	48,708	51,86	51,86	51,86	0,00	24,96	24,97	24,98	24,98	24,97	0,01	1,9195
313_02_12	49,077	51,94	51,97	51,96	0,02	25,01	25	25	25,01	25,01	0,01	1,9228
313_02_13	48,876	51,74	51,73	51,74	0,01	25,01	25	25,01	25,01	25,01	0,00	1,9231

Table III-I Sample measurements for Castlegate core samples

Sample	Mass	L1	L2	L avg	L std.dev	D1	D2	D3	D4	D avg	D std.dev	Density
[#]	[g]	[mm]	[mm]	[mm]	[mm]	[mm]	[mm]	[mm]	[mm]	[mm]	[mm]	[g/cm3]
Average	48,79	51,75	51,79	51,77	0,03	25,00	25,00	25,00	25,00	25,00	0,01	1,9202
STDEV	0,1877	0,1712	0,2015	0,1829	0,05	0,03	0,02	0,02	0,02	0,02	0,00	0,0046
Max	49,08	51,94	52,07	51,96	0,19	25,05	25,03	25,02	25,03	25,03	0,02	1,9290
Min	48,27	51,23	51,22	51,23	0,00	24,94	24,95	24,94	24,95	24,95	0,00	1,9103
Diff max min	0,804	0,710	0,850	0,730	0,191	0,11	0,08	0,08	0,08	0,08	0,01	0,0187

Table III-II Statistic figures comparing the different core samples

Figure III-I Strain Gauge specifications

CALCULATION OF THERMAL OUTPUT
FOR STRAIN GAGES

The thermal output of the gages contained in this package can be calculated from the following polynomial expression

$$a0 + a1*T + a2*T^2 + a3*T^3 + a4*T^4$$

where aN are the coefficients and T^N is temperature to the Nth power.

The coefficients for both Celsius and Fahrenheit temperature scales are provided on the data label affixed to this package for strain gages.

A-Alloy, D-Alloy, and E-Alloy will generally use all five coefficients (a0 to a4) but K-Alloy will generally use only the first four coefficients (a0 to a3) with the fifth (a4) being zero.

Figure III-II Thermal output of the strain gauges
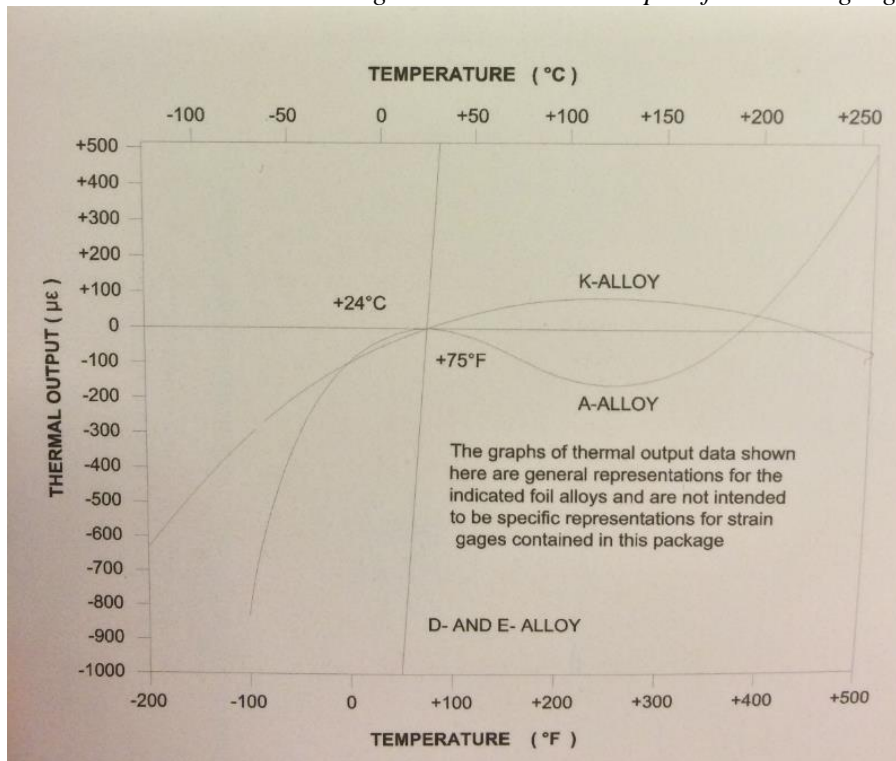
Figure III-III The graph of the thermal output

VI
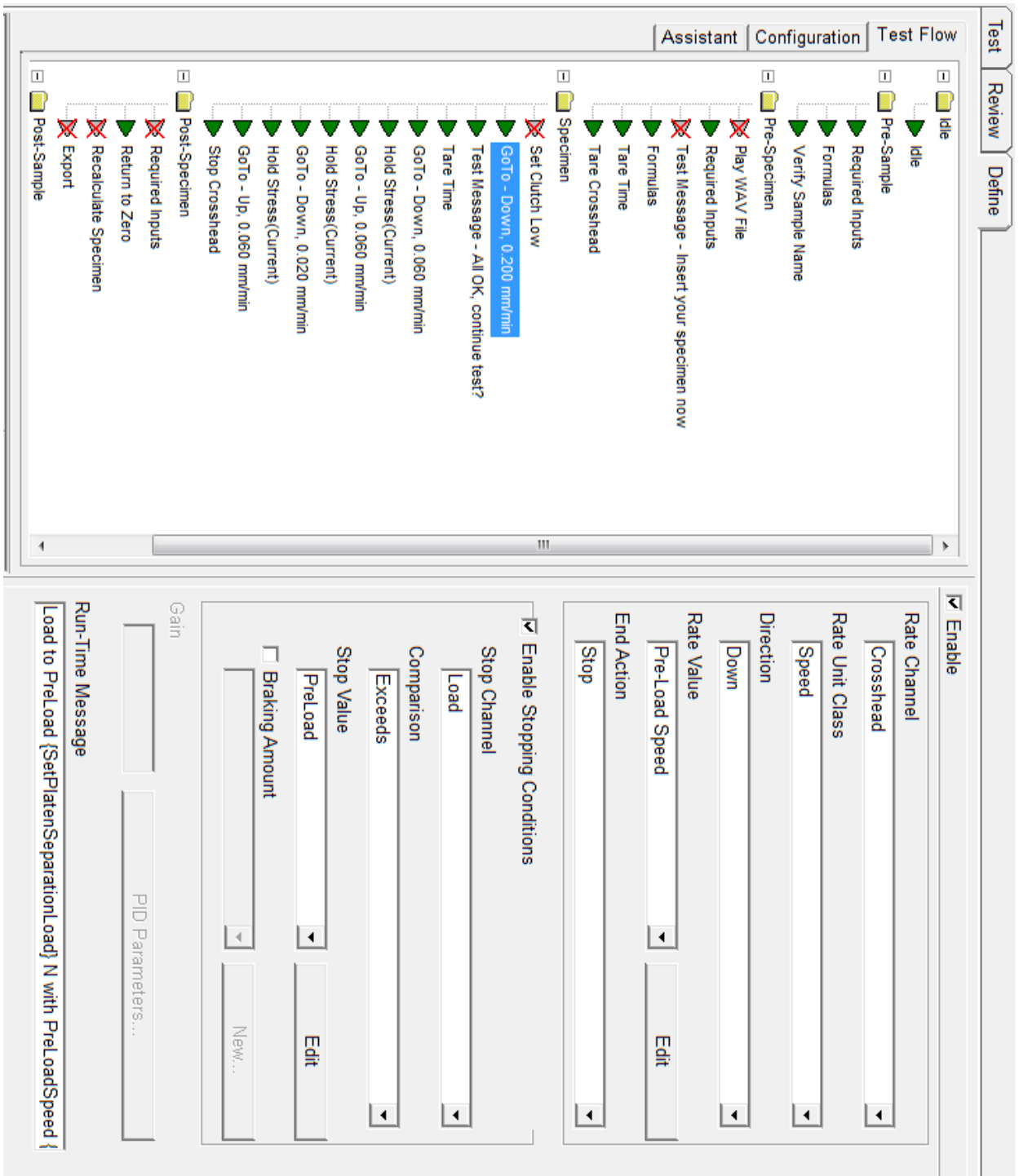
Figure III-IV An A screenshot of the procedure defintion function in TestWorks

Appendix IV. Results from Thesis

IV.I   Core sample 313_02_04

IV.I.I   LVDT
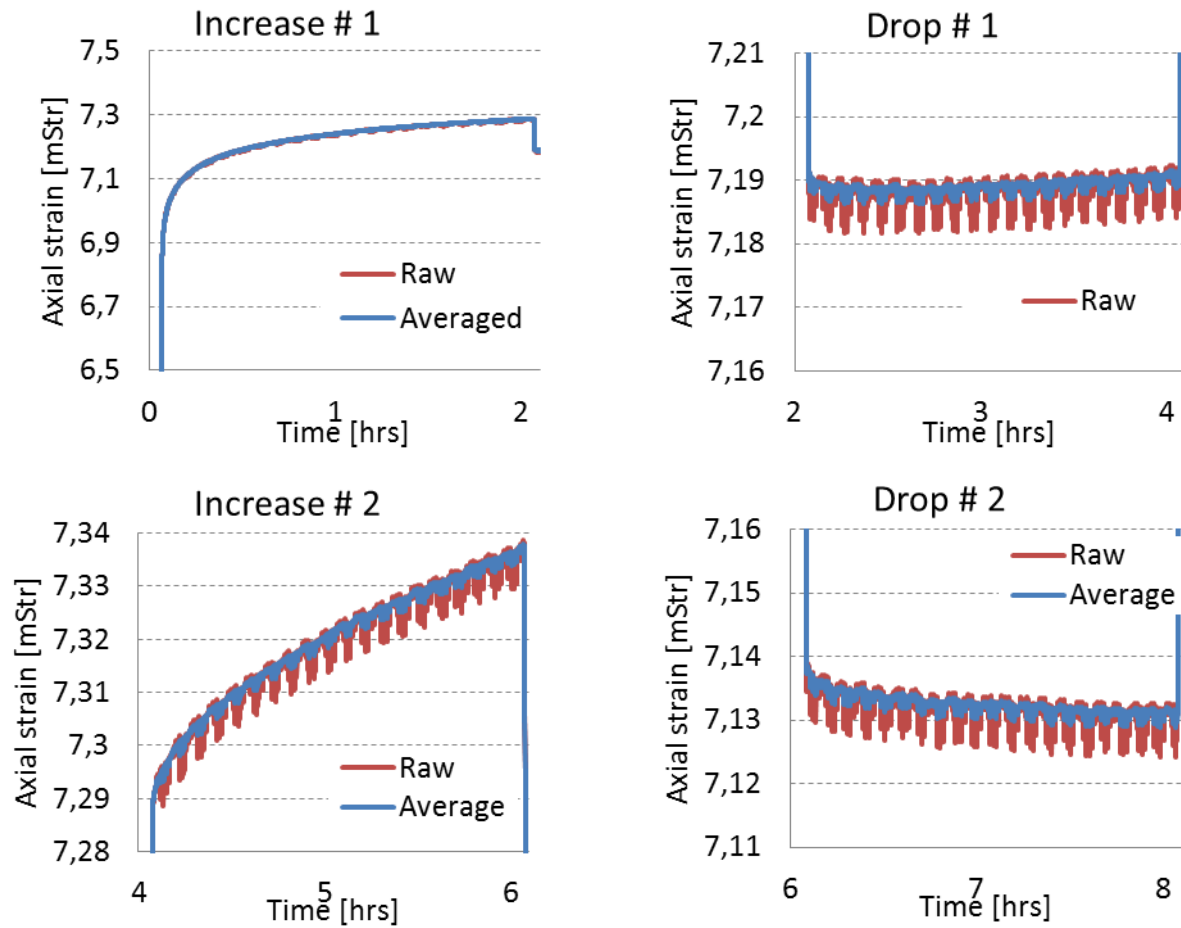
Figure IV-I LVDT measurements for the four first stress steps including two full cycles of loading and unloading
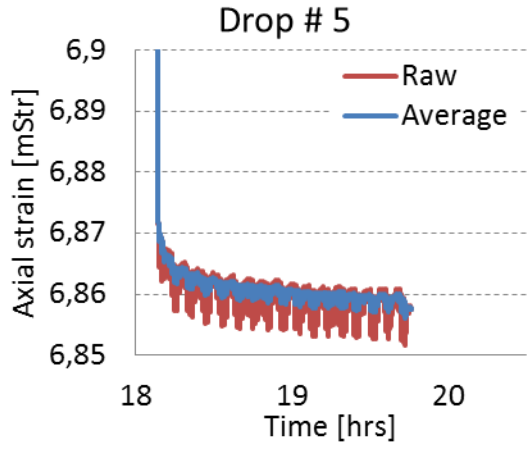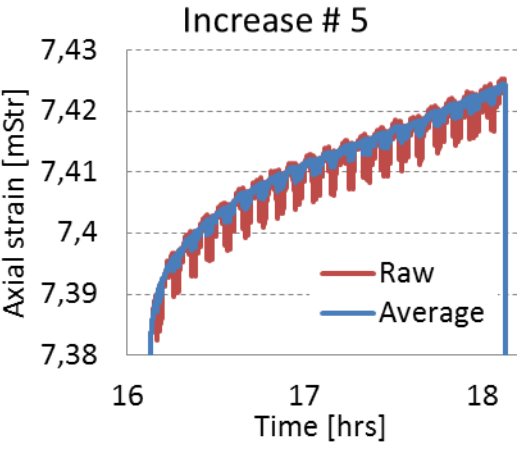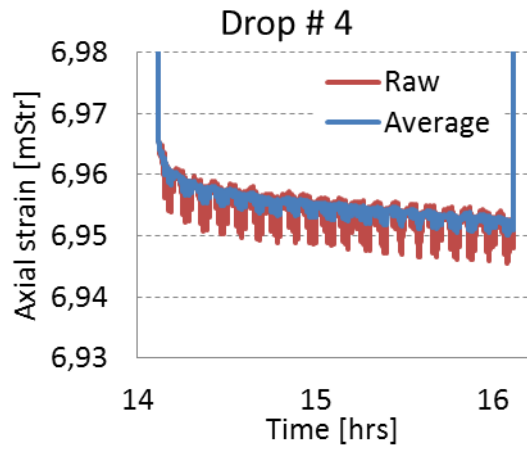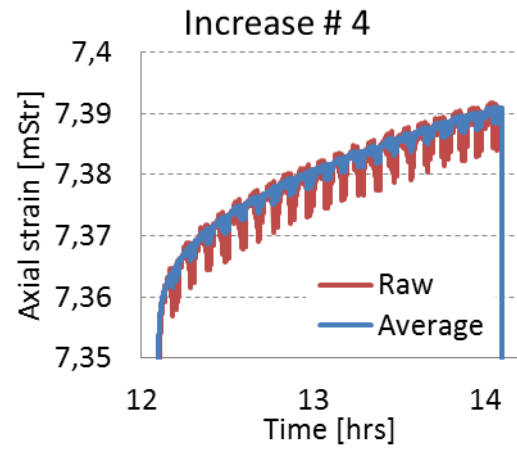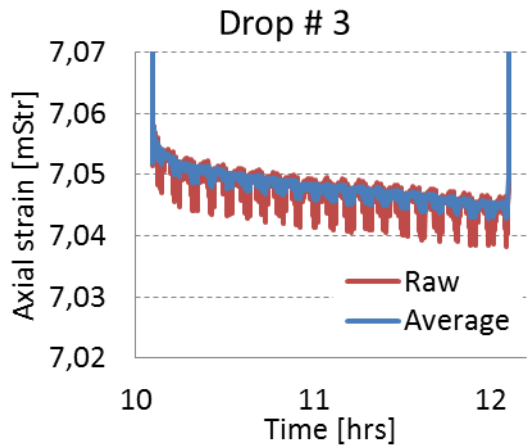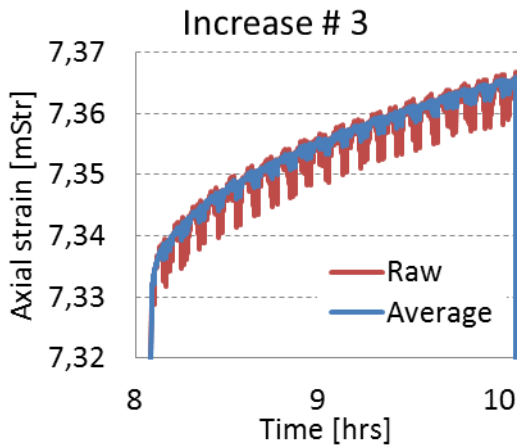
Figure IV-II LVDT measurements for the six last stress steps including three full cycles of loading and unloading

IV.I.II   Strain Gauge
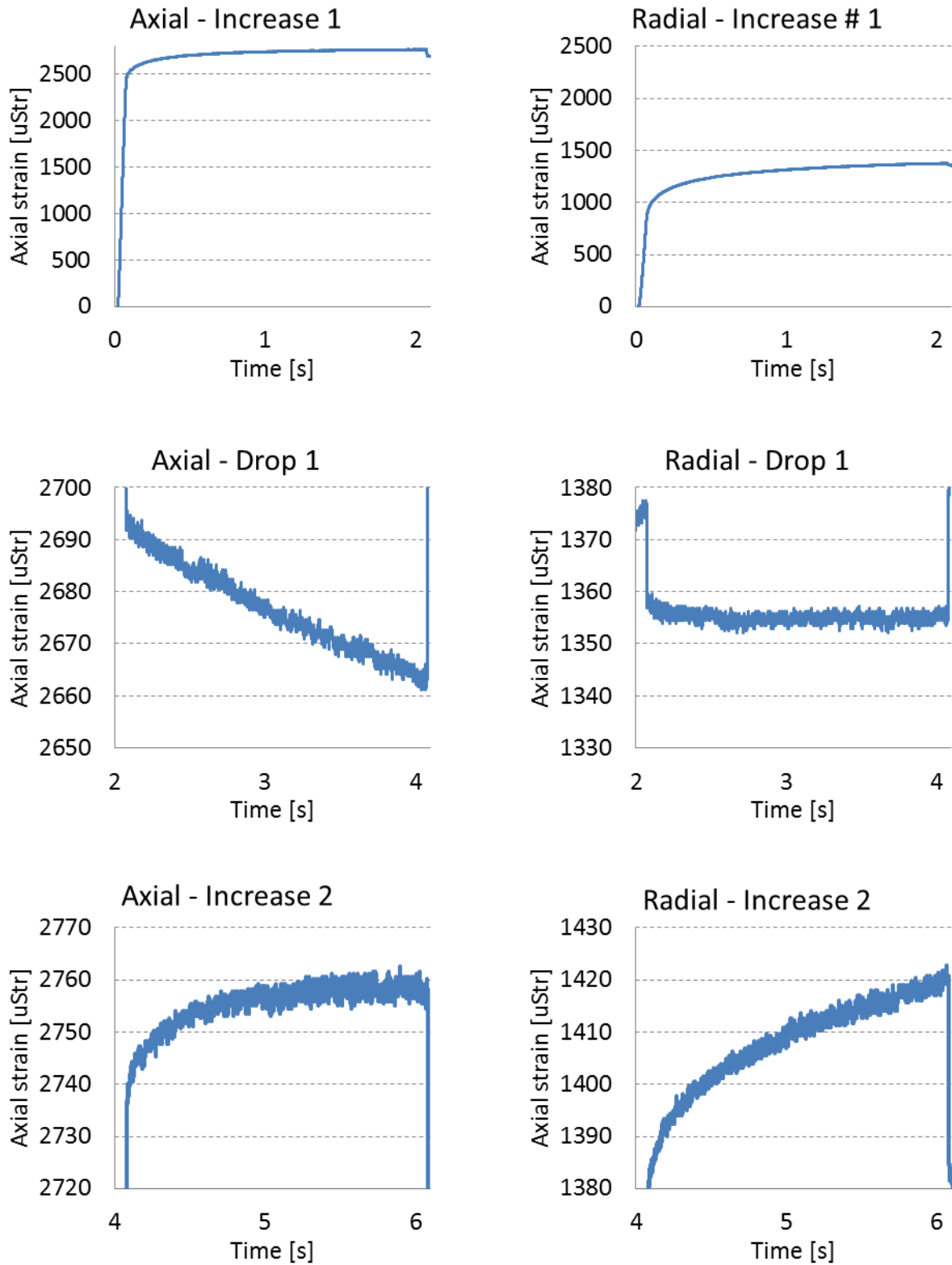
Figure IV-III Strain gauge measurements of the axial and radial response to the three first stress steps
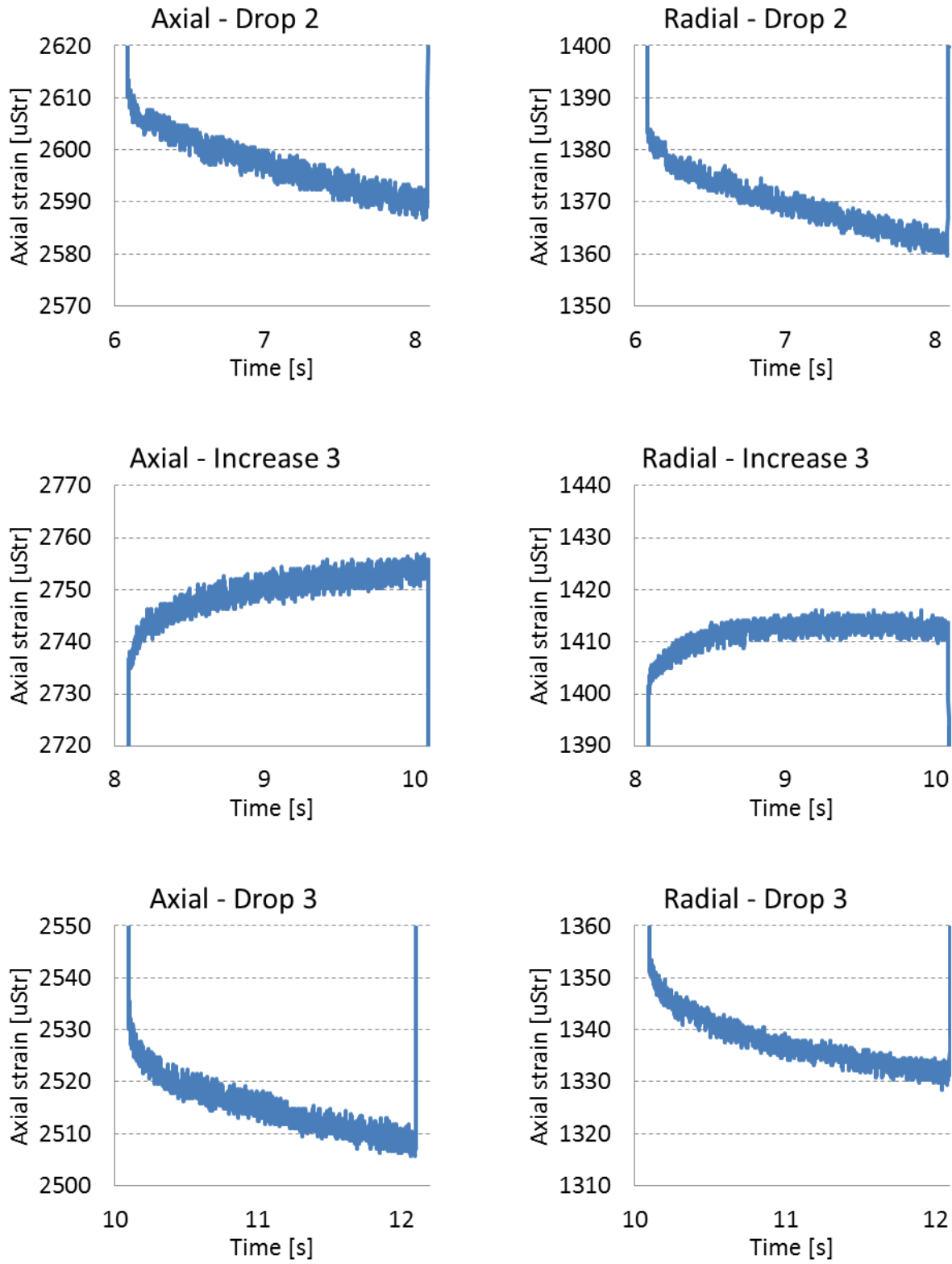
Figure IV-IV Strain gauge measurements of the axial and radial response to the 4th, 5th and 6th stress step
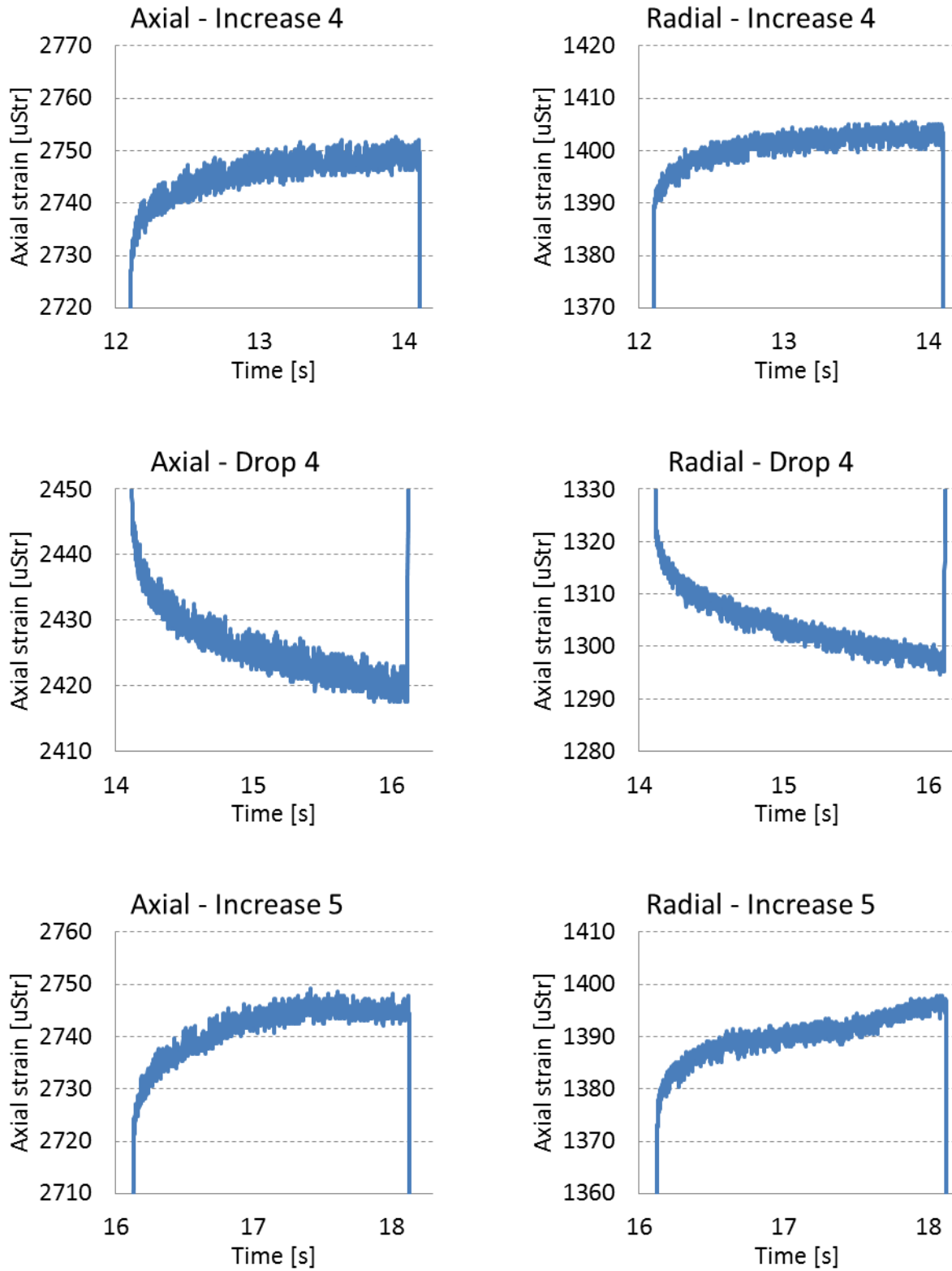
Figure IV-V Strain gauge measurements of the axial and radial response to the 7th, 8th and 9th stress step

XII
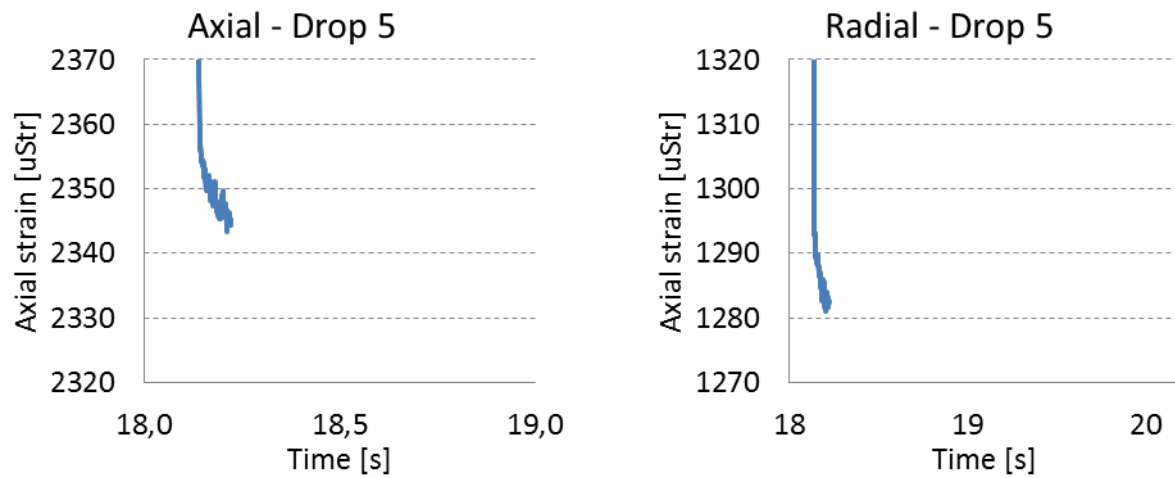
Figure IV-VI Strain gauge measurements of the axial and radial response to the 10th, 11th and 12th stress step

IV.I.III Acoustic
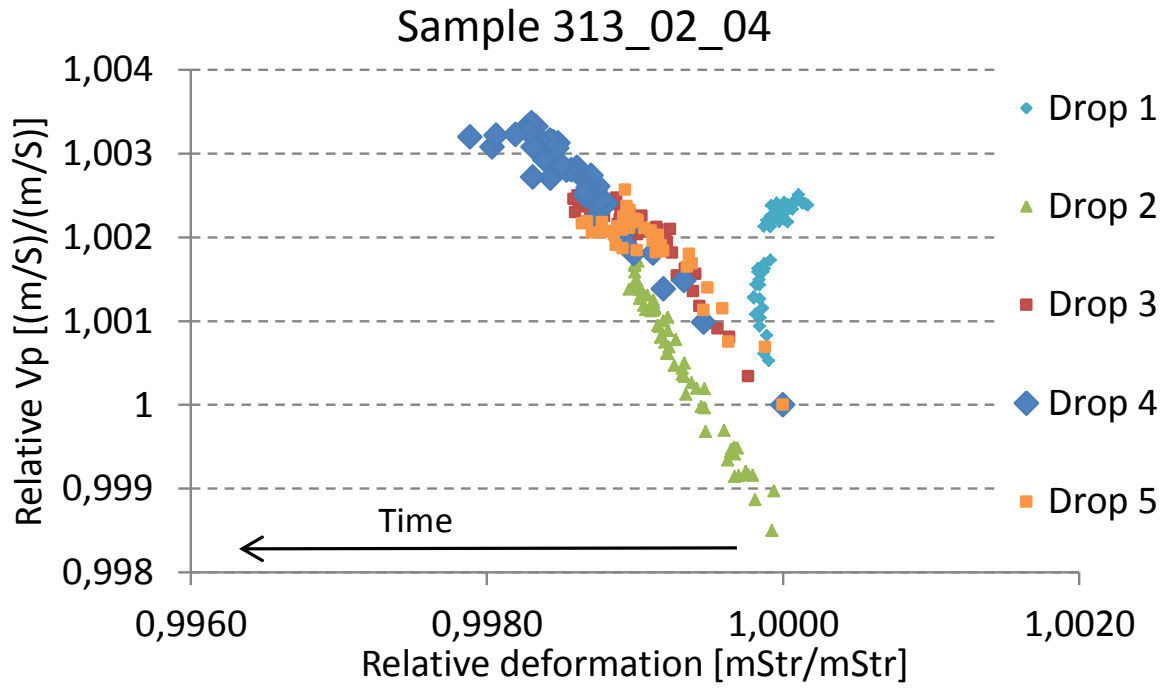
Figure IV-VII Relative velocity and deformation for the hold periods following increases in stress
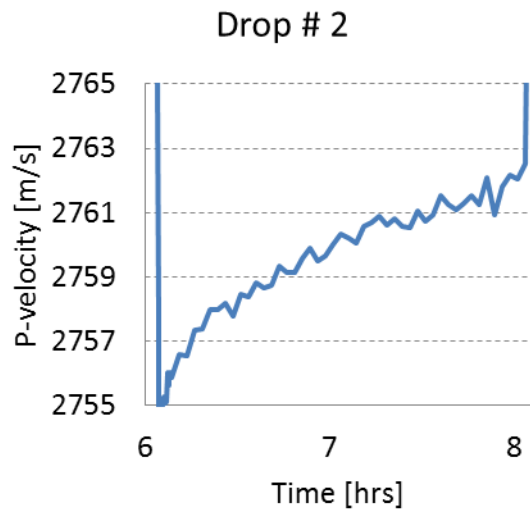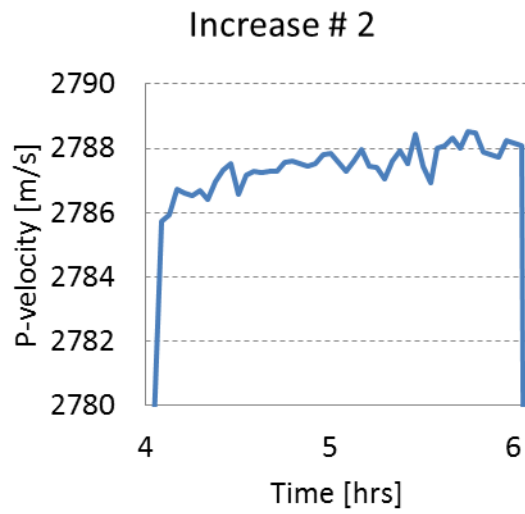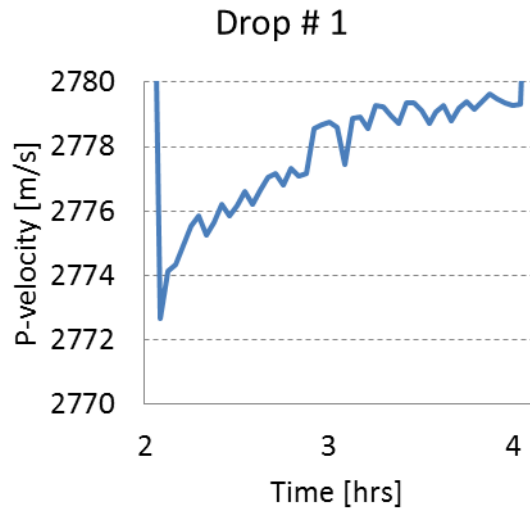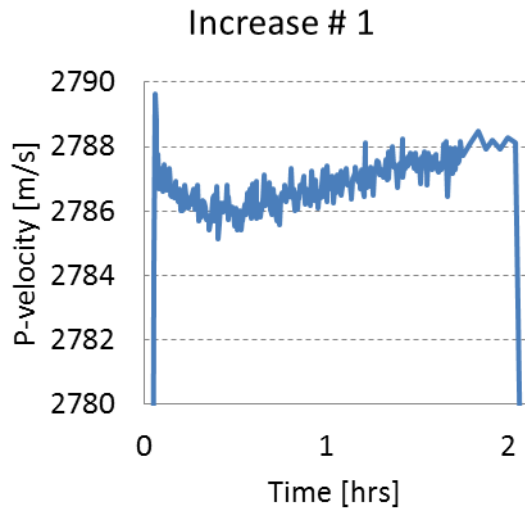
Figure IV-VIII Zoom-in of the P-wave velocity of the four first stress steps
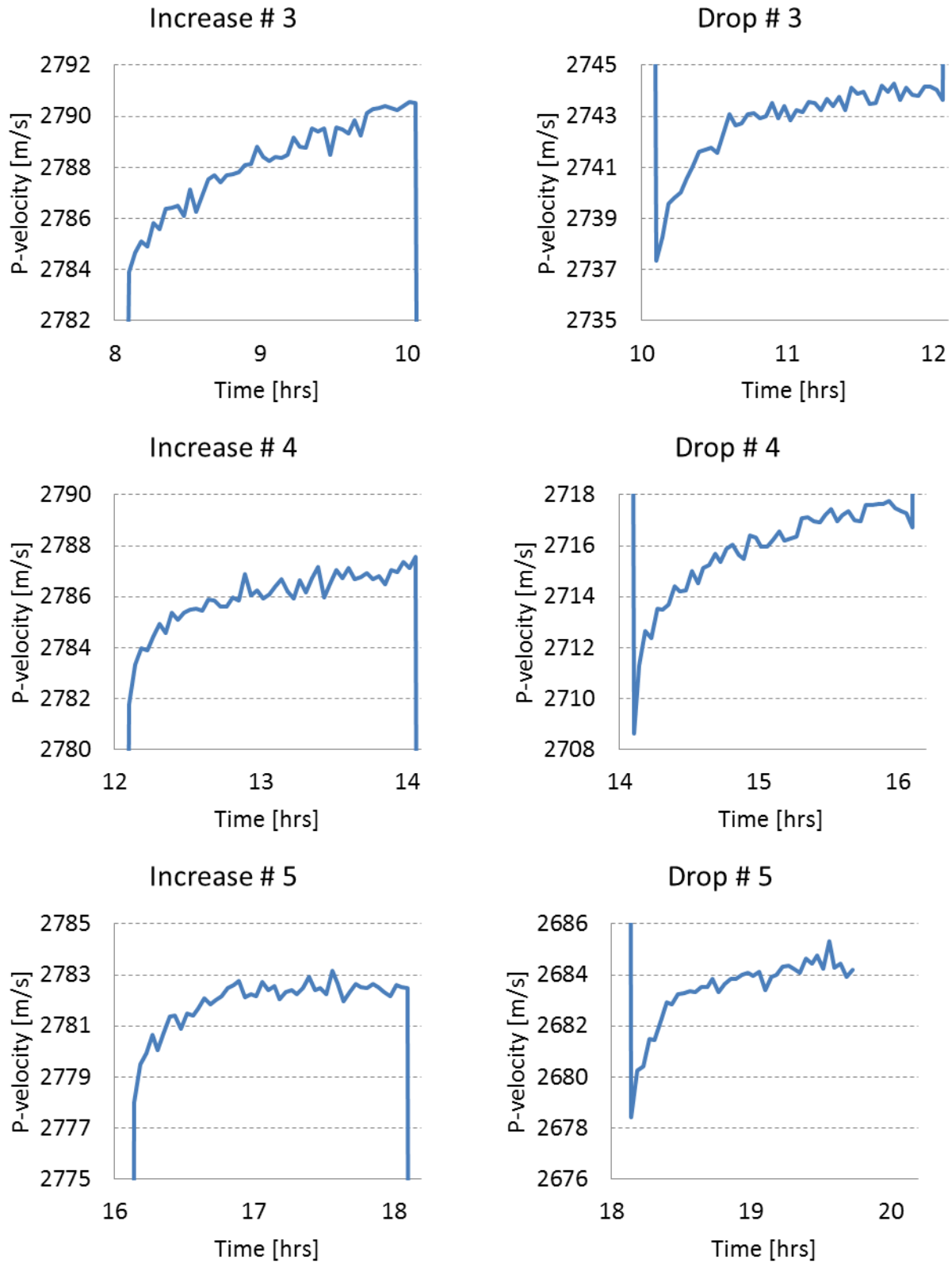
Figure IV-IX Zoom-in of the P-wave velocity of the is first stress steps

IV.II Core sample 313_02_08

IV.II.I LVDT
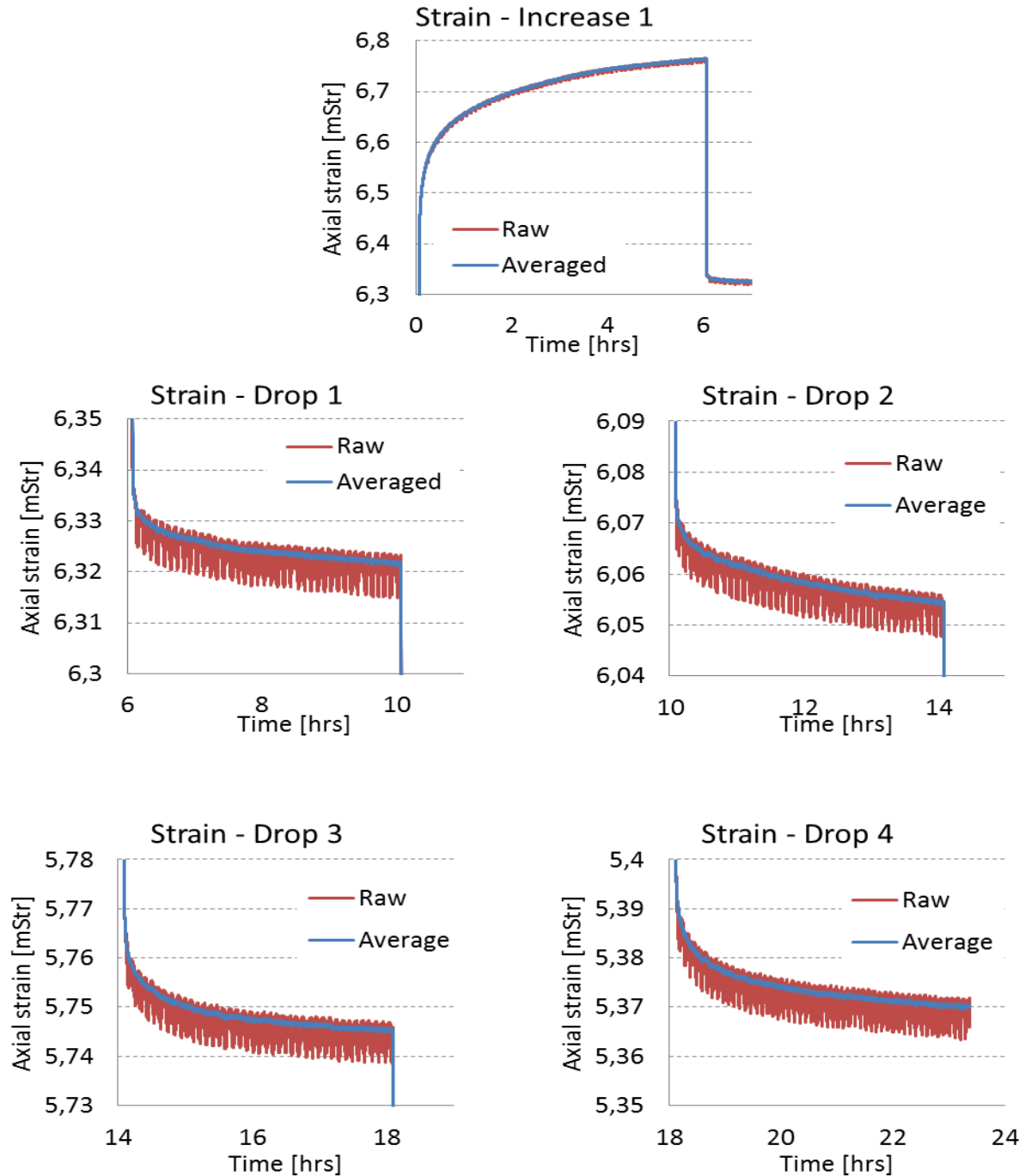
Figure IV-X A zoom of the five stress levels region where the time-dependent change in the strain are visible. In total there are one loading and four unloading levels.
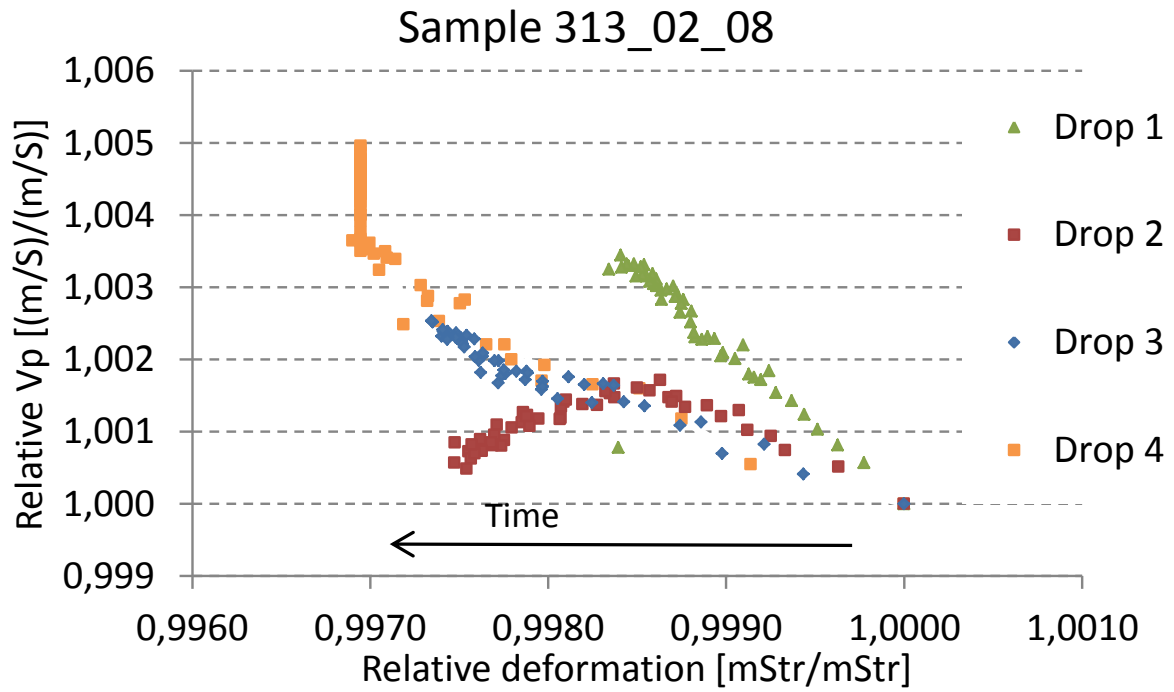
Figure IV-XI Relative velocity and deformation for the hold periods following increases in stress
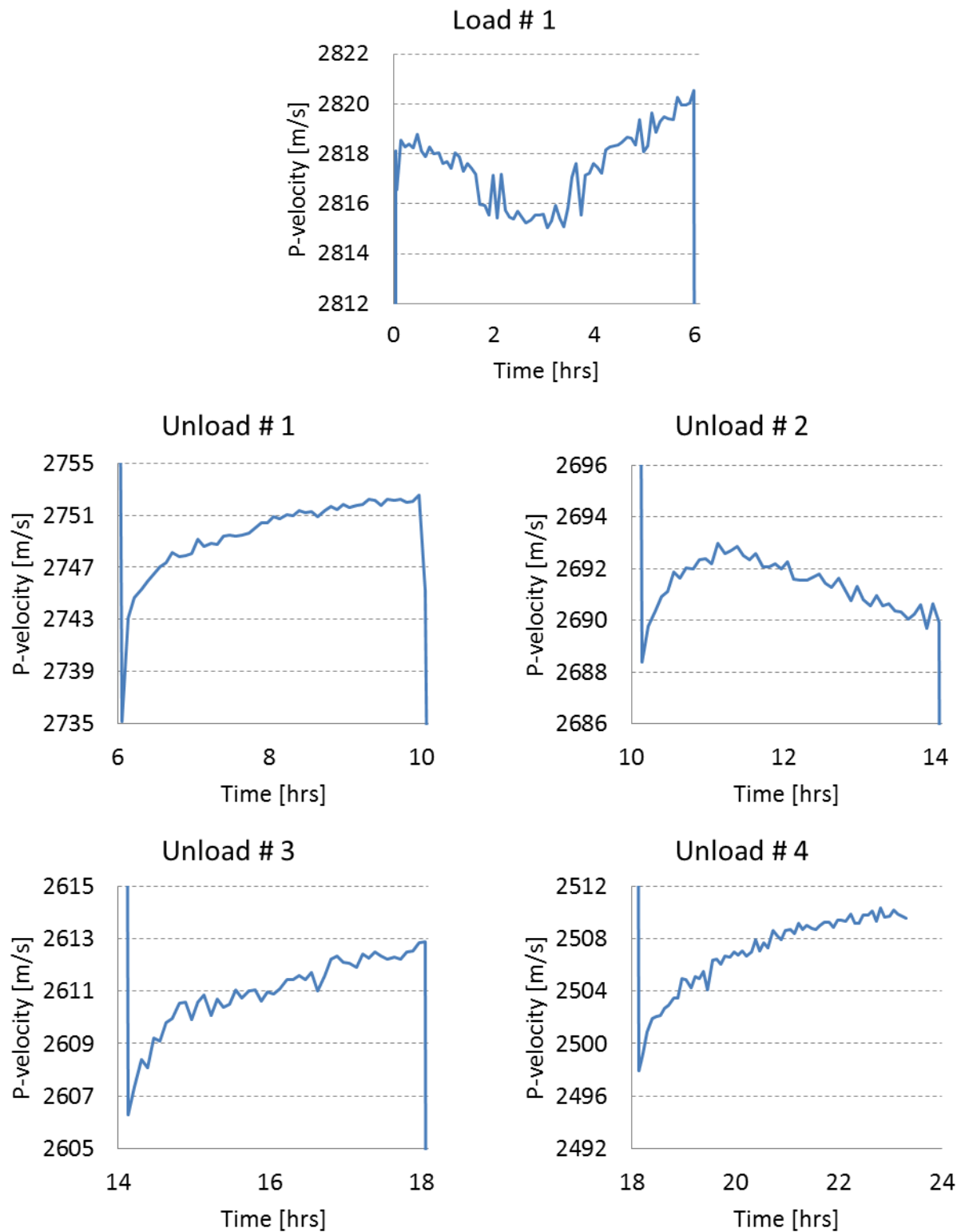
Figure IV-XII A zoom of the five stress levels region where the time-dependent change in the P-Velocity are visible. In total there are one loading and four unloading levels.

IV.III Core sample 313_02_09

IV.III.I LVDT
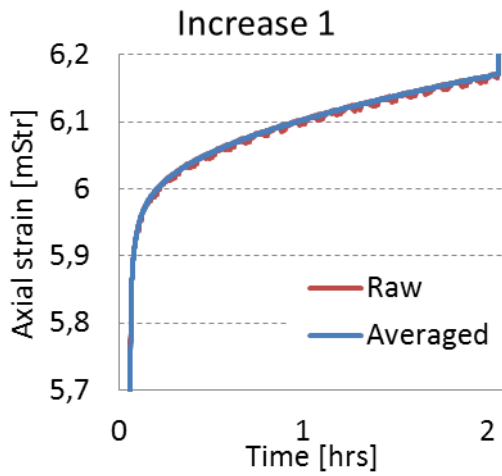
Figure IV-XIII First stress step, where the stress was increased from 0-14 MPa
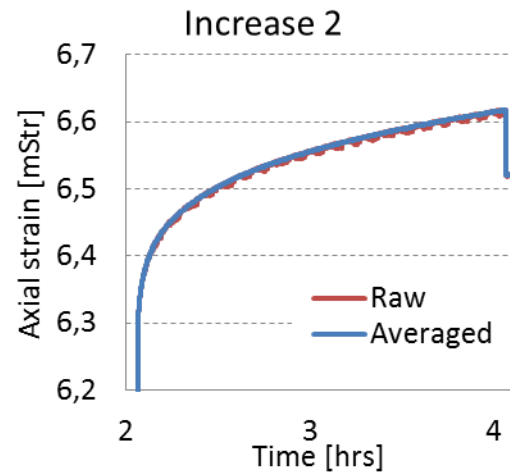
Figure IV-XIV Second stress step, where the stress was increased from 14-15MPa
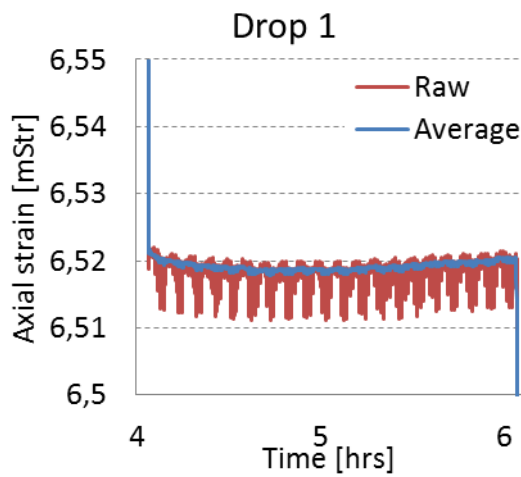
Figure IV-XV Zoom in of the first decrease in stress, 15 MPa → 14 MPa
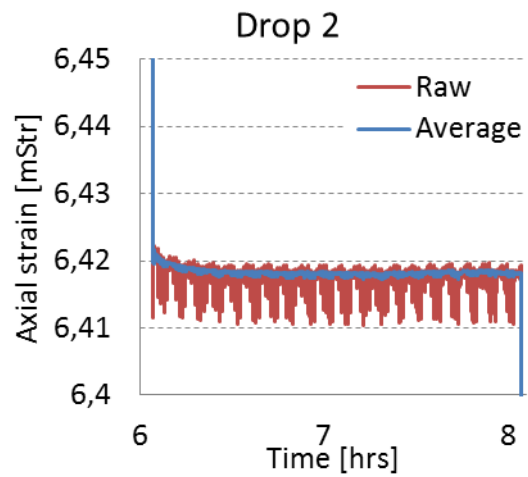
Figure IV-XVI Zoom in of the second decrease in stress, 14 MPa → 13 MPa
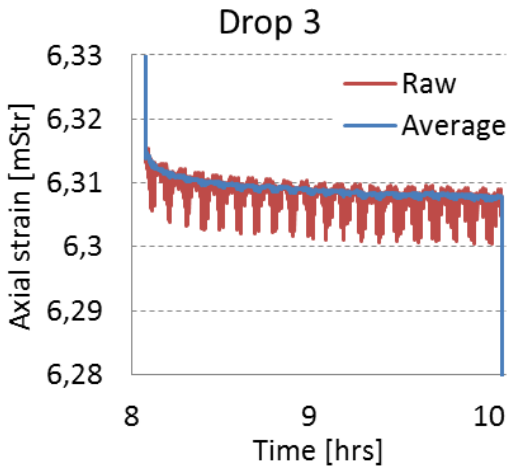
Figure IV-XVII Zoom in of the second decrease in stress, 13 MPa → 12 MPa
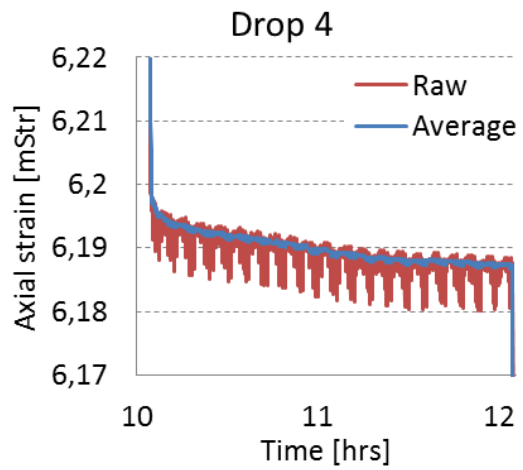
Figure IV-XVIII Zoom in of the second decrease in stress, 12 MPa → 11 MPa
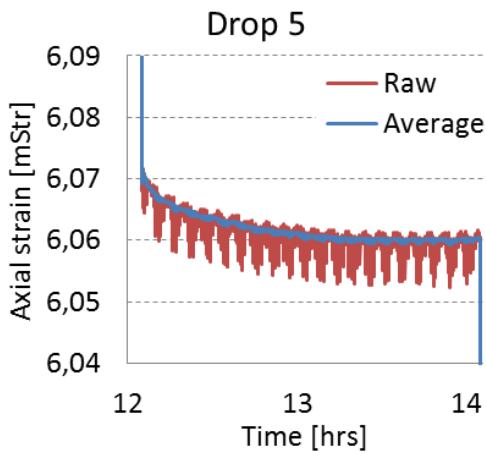
Figure IV-XIX Zoom in of the second decrease in stress, 11 MPa → 10 MPa
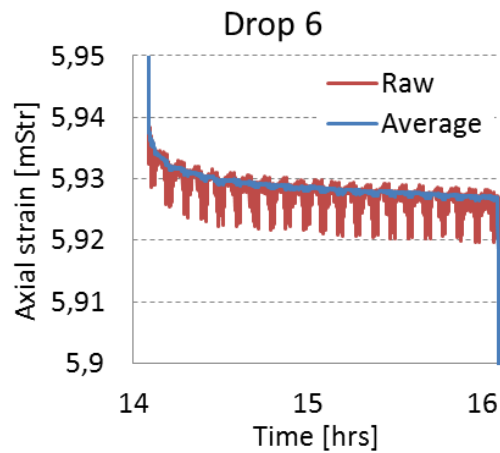
Figure IV-XX Zoom in of the second decrease in stress, 10 MPa → 9 MPa
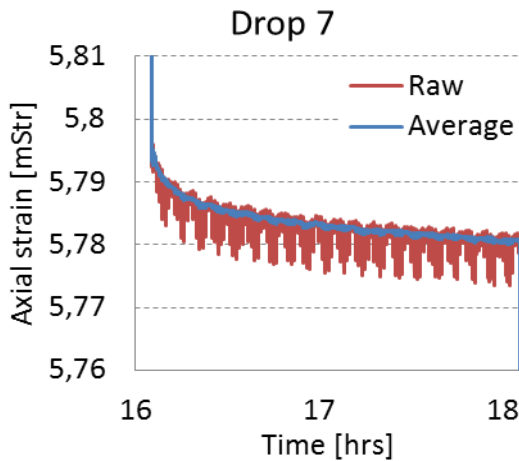
Figure IV-XXI Zoom in of the second decrease in stress, 9 MPa → 8 MPa
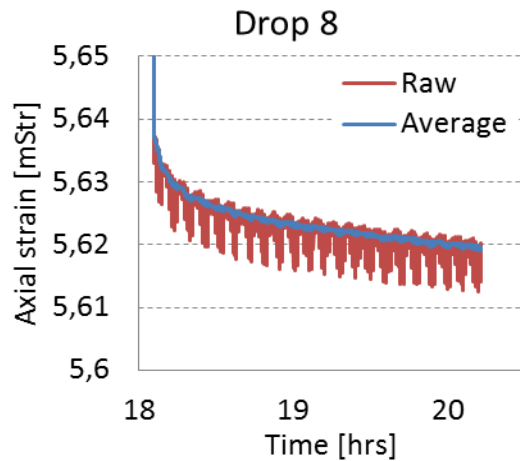
Figure IV-XXII Zoom in of the second decrease in stress, 8 MPa → 7 MPa

IV.III.II Acoustic
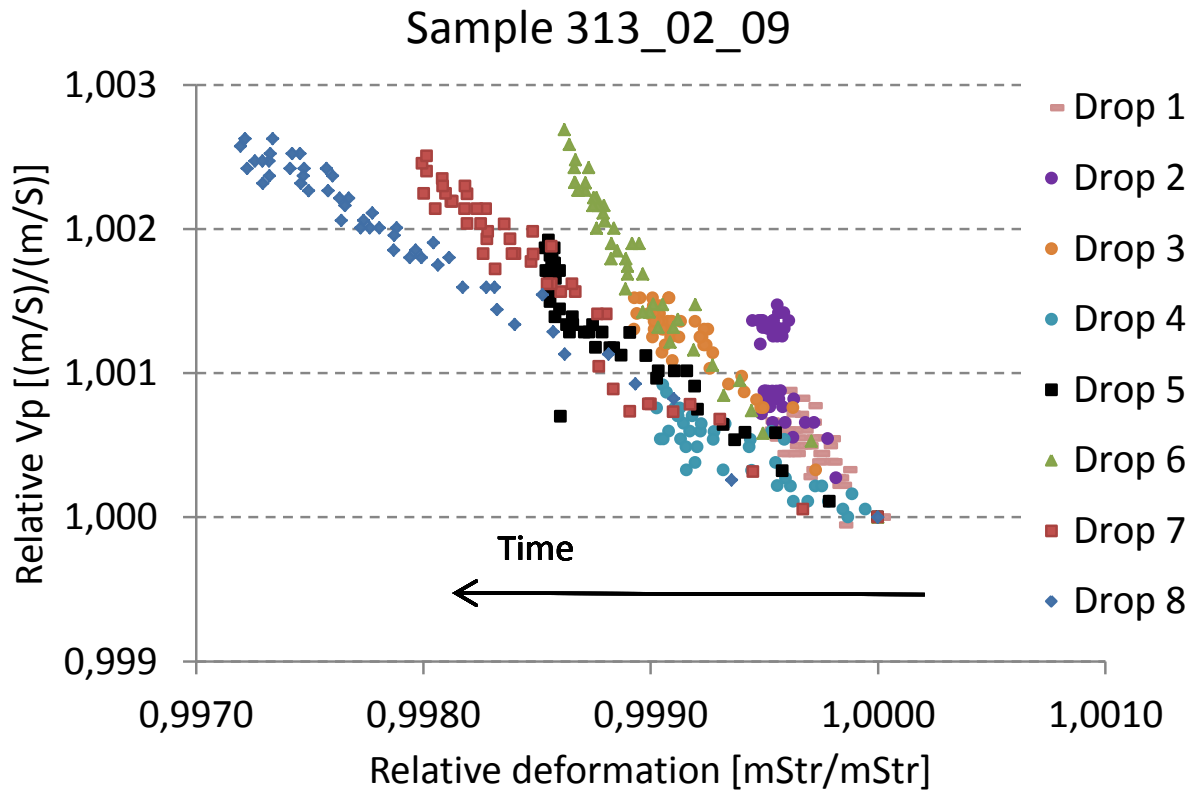
Figure IV-XXIII Relative velocity and deformation for the hold periods following increases in stress
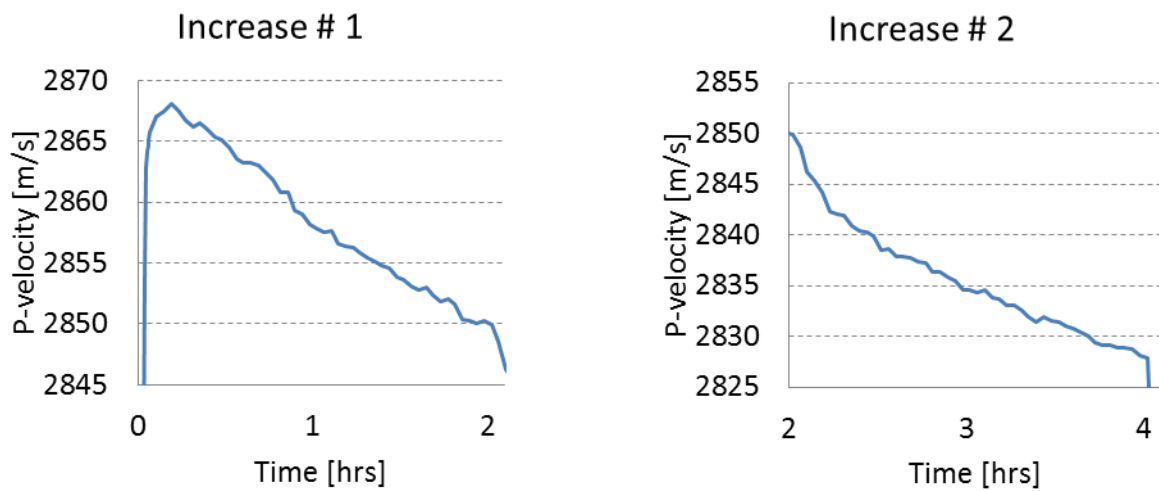
Figure IV-XXIV Zoom in of the P-wave Velocity for the two increases in stress
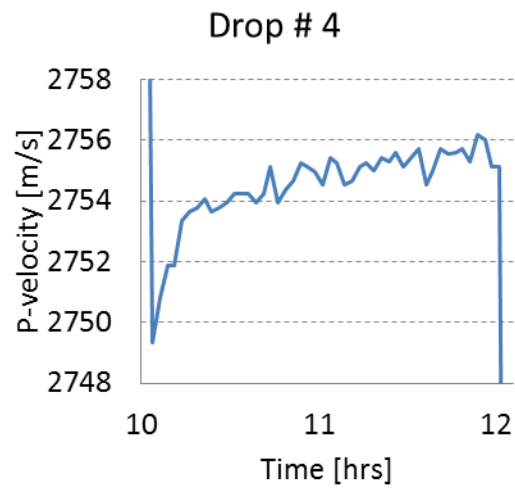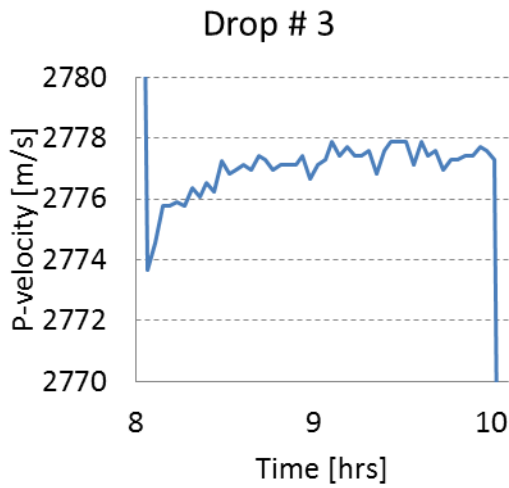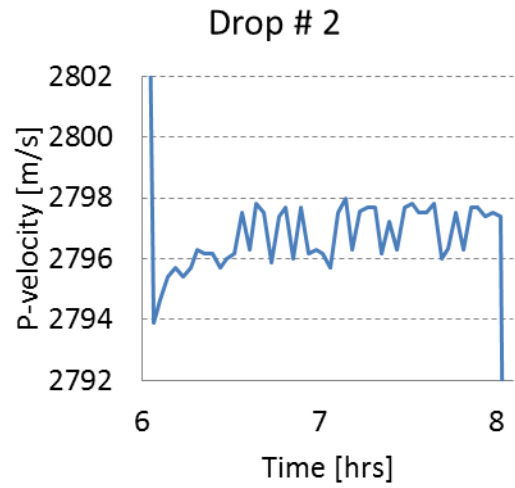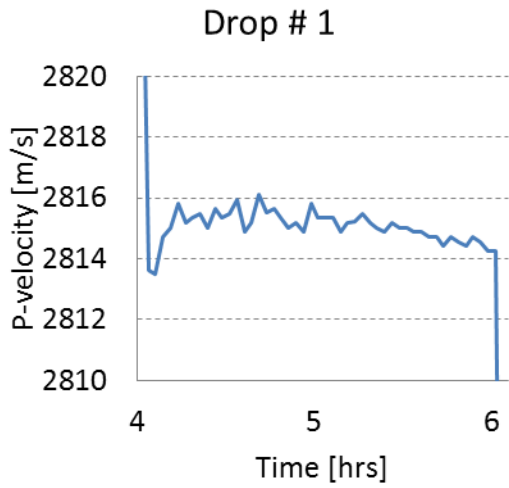
Figure IV-XXV Zoom in of the P-wave Velocity for the four first drops in stress
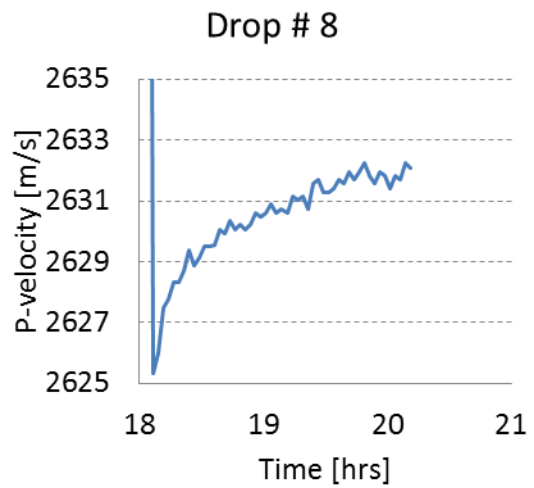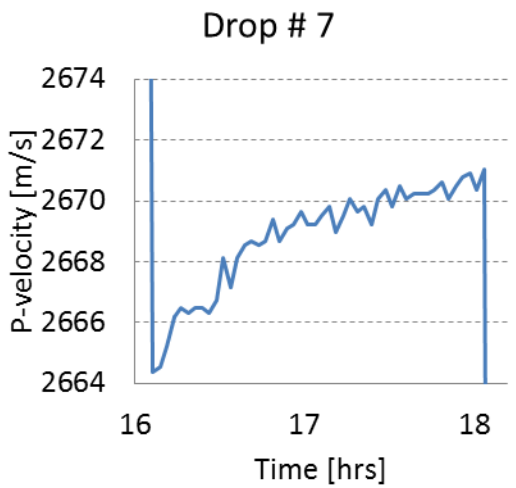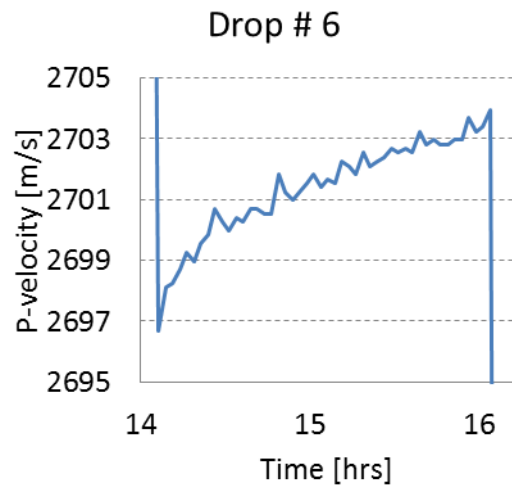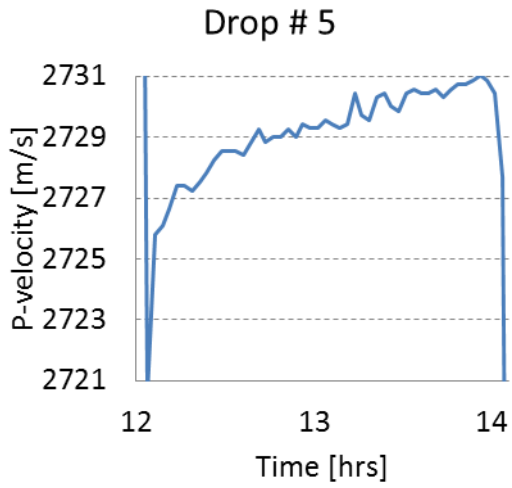
Figure IV-XXVI Zoom in of the P-wave Velocity of the four last drops in stress

IV.IV   Core sample 313_02_12

IV.IV.I   LVDT
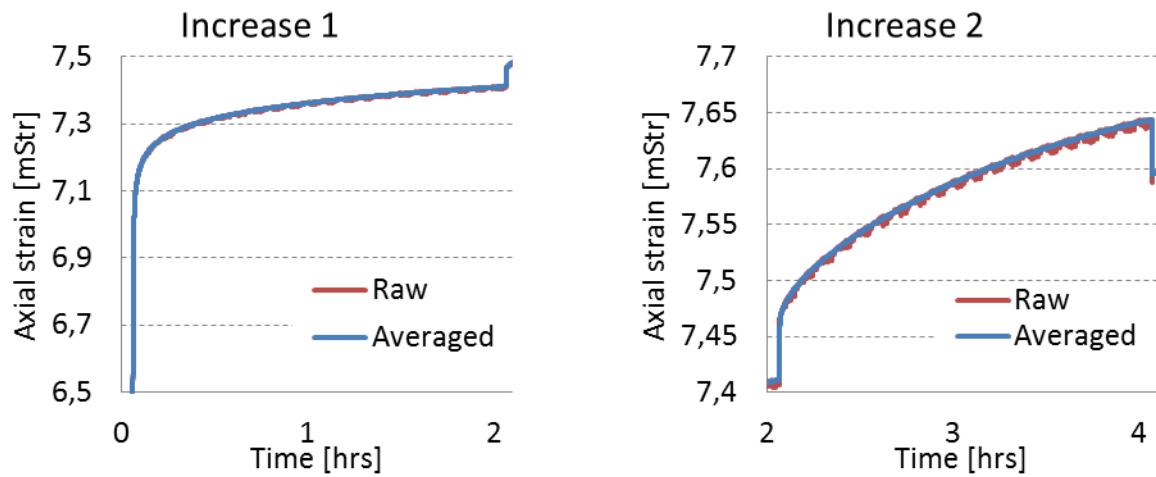
Figure IV-XXVII The two first stress steps where the stress is increased from 0-14.5 MPa for the plot on the left and from 14.5-15 MPa for the plot on the right
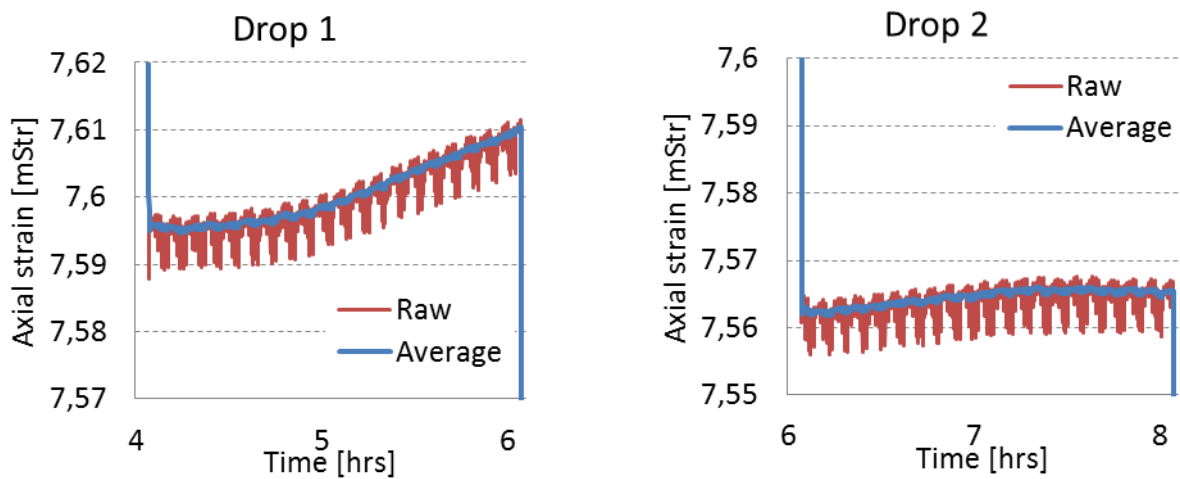
Figure IV-XXVIII The two first stress steps where the stress first drops from 15.0-14.5 MPa for the plot on the left and from1 14.5-14.0 MPa for the plot on the right
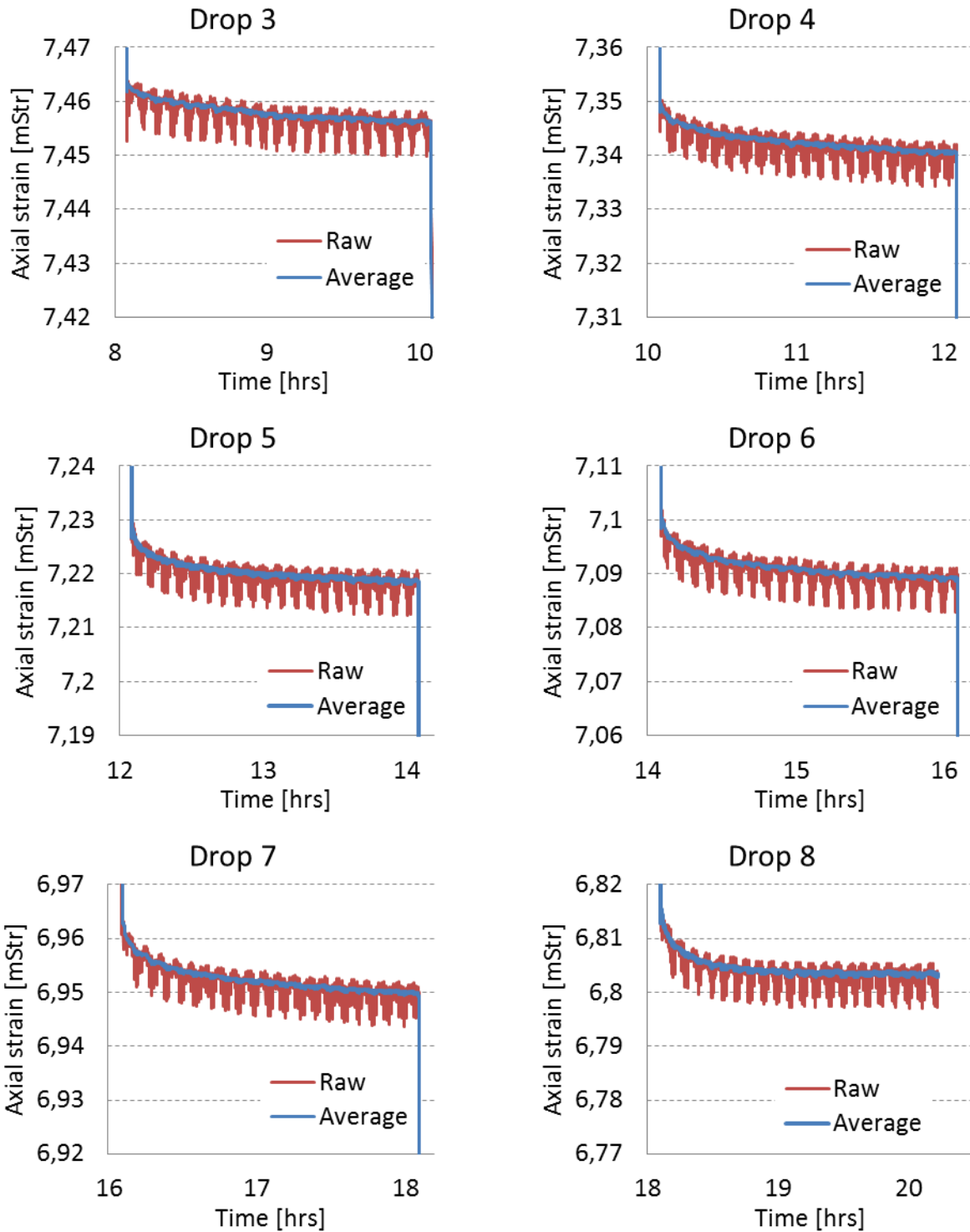
Figure IV-XXIX The six last stress steps where the stress continues to drop 1.0 MPa for each step

IV.IV.II Strain gauge

Axial - Drop 5

Radial - Drop 5

Axial - Drop 6

Radial - Drop 6

XXX
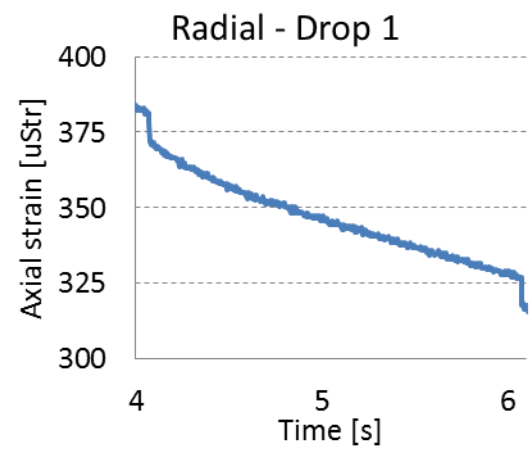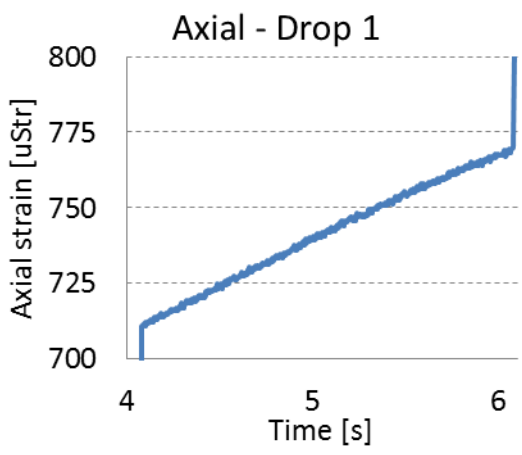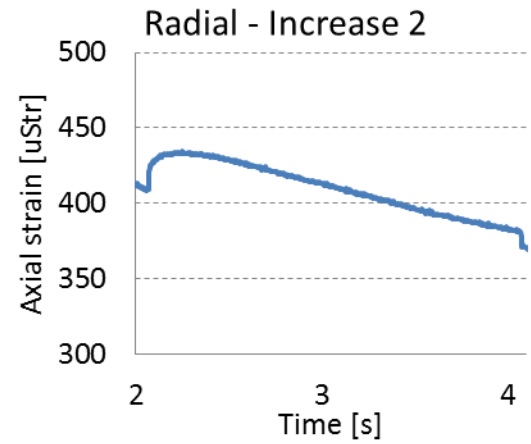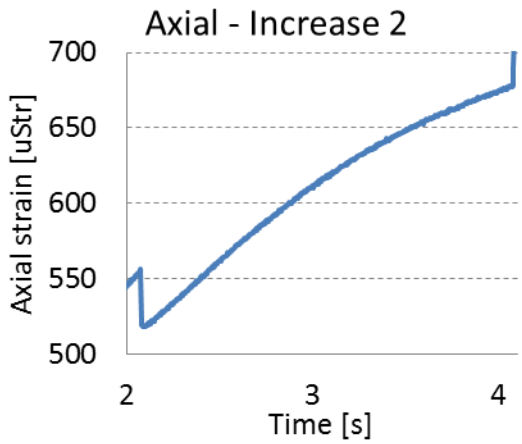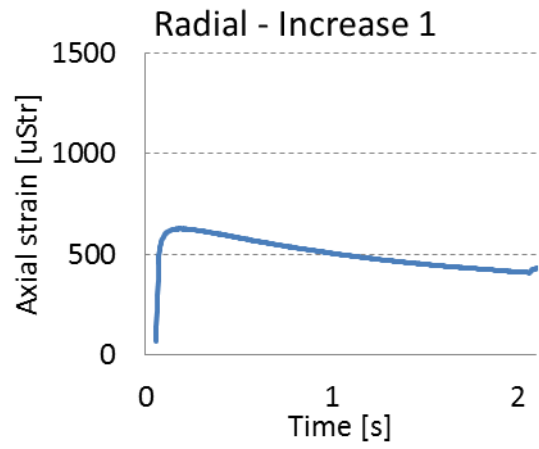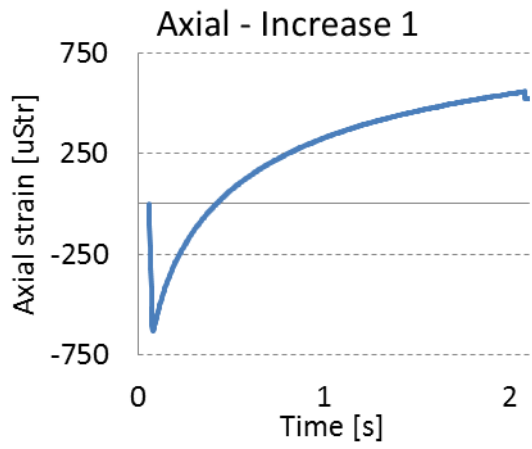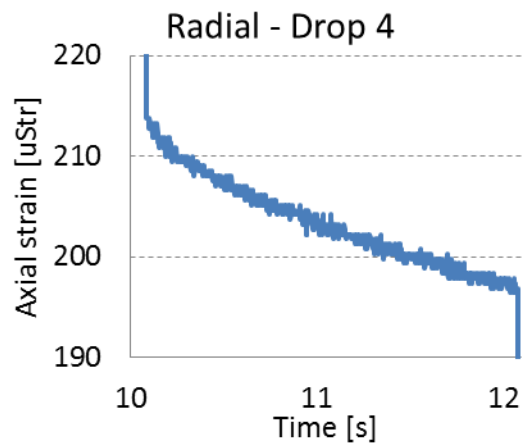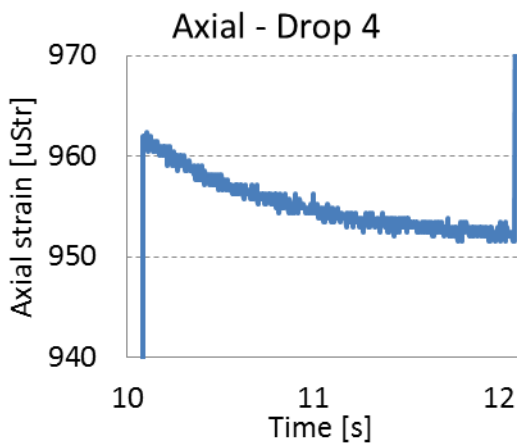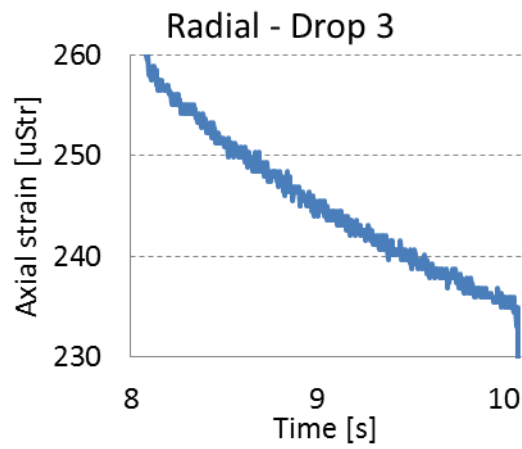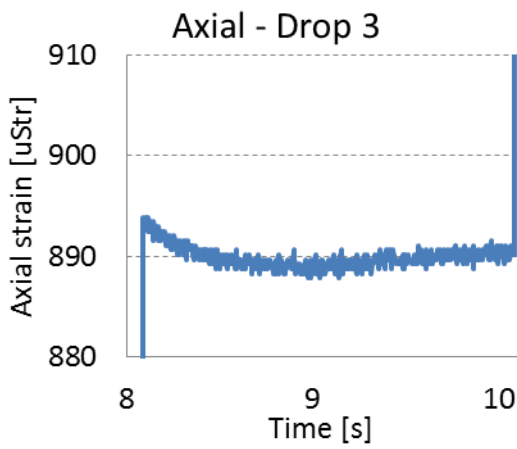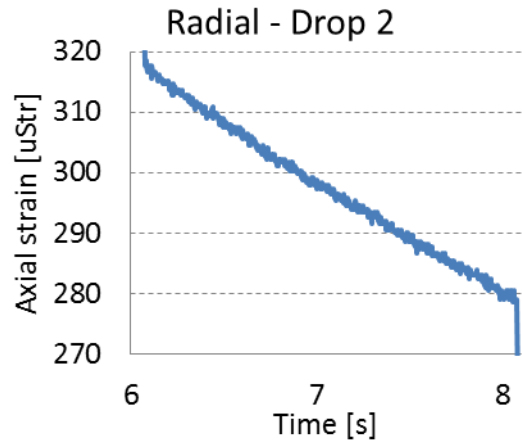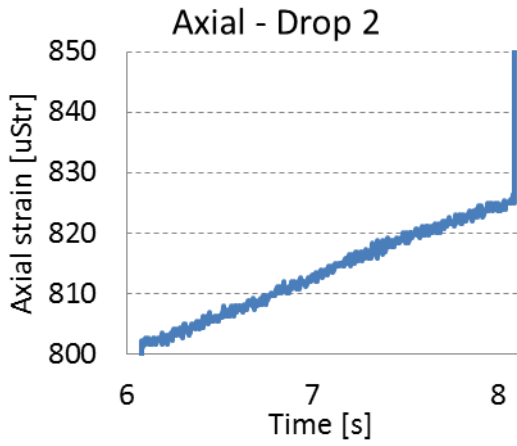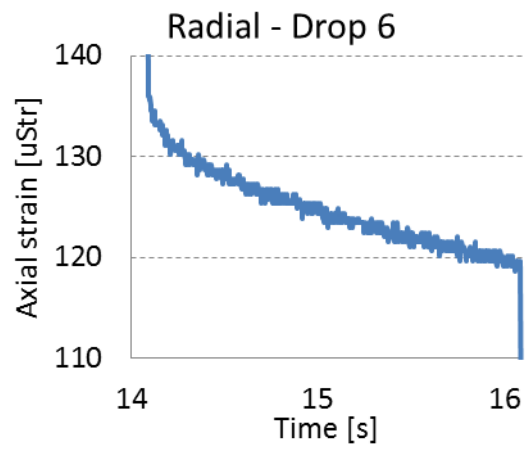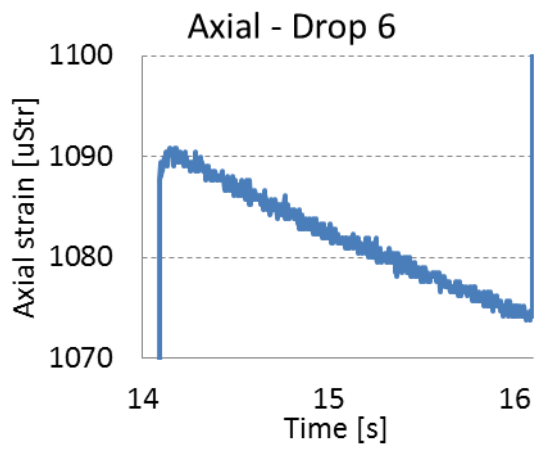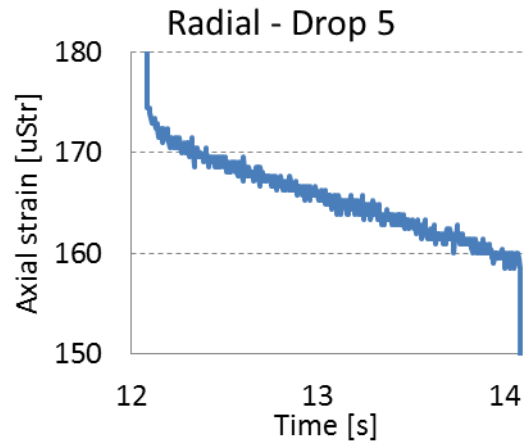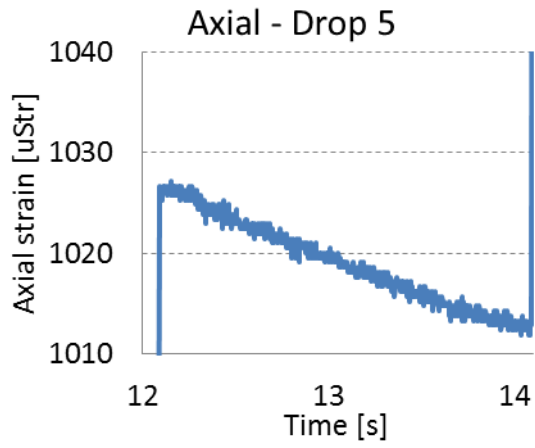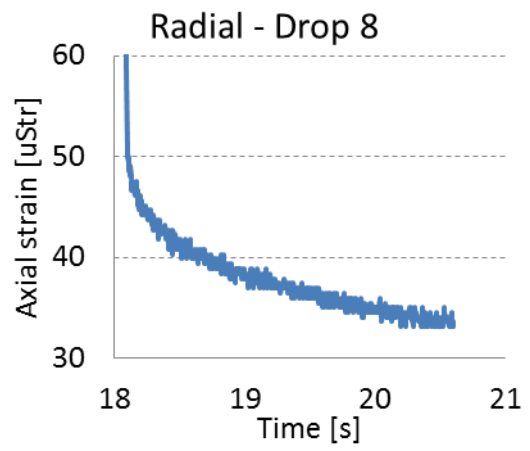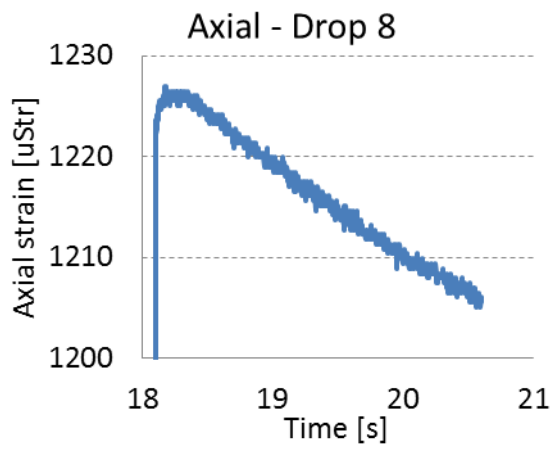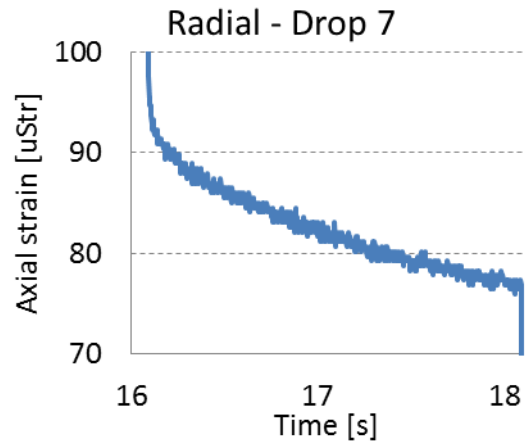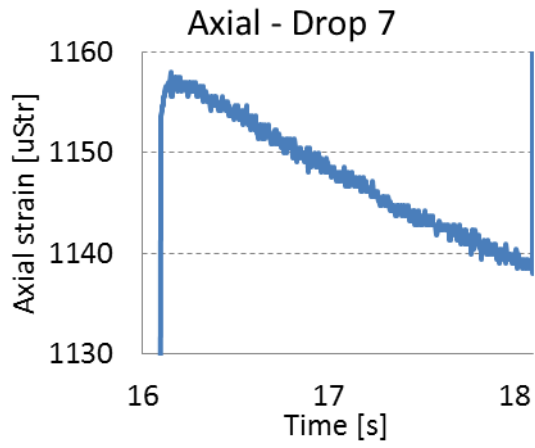
IV.IV.III Acoustic
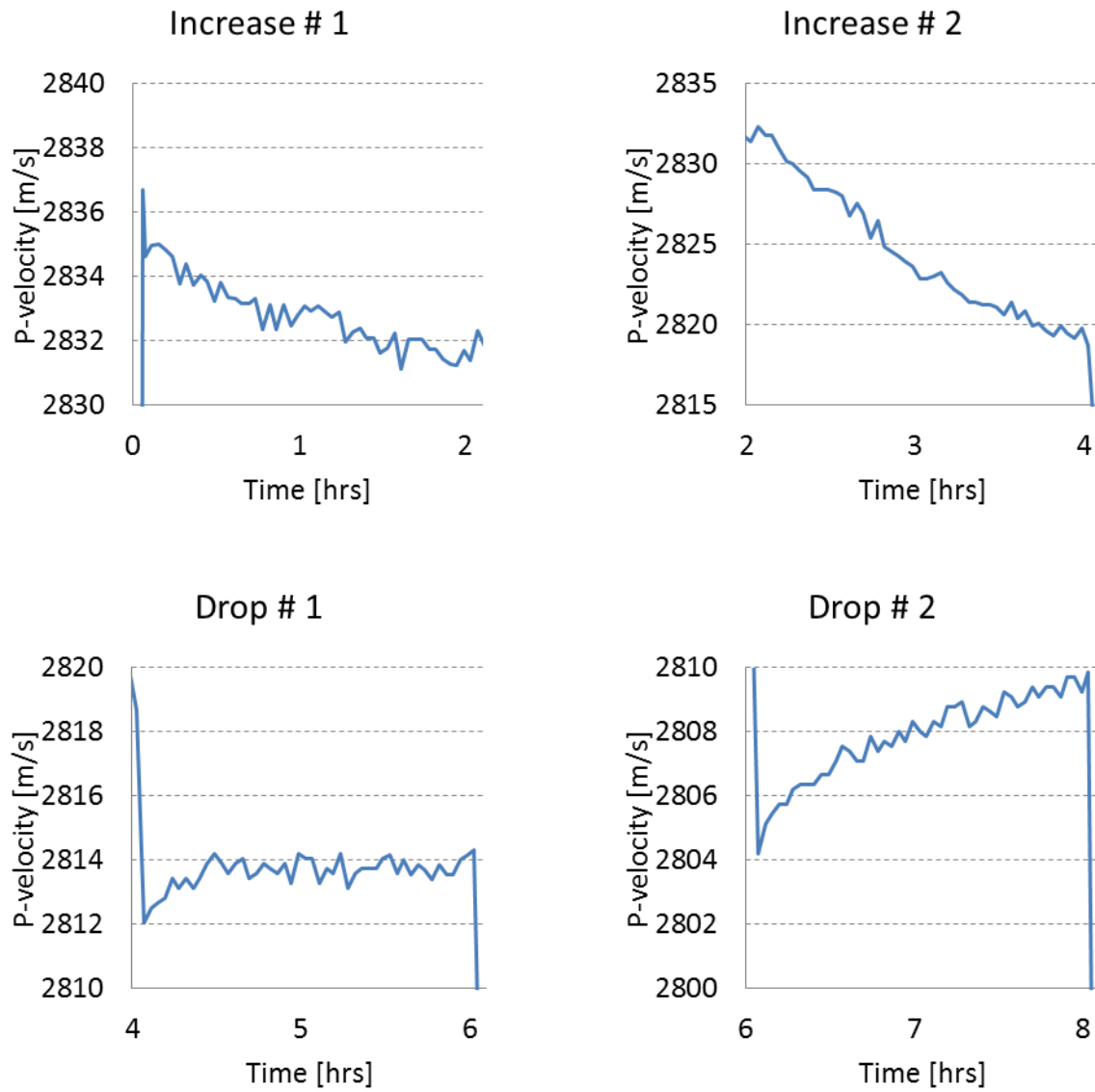
Figure IV-XXX The transient response of the P-wave velocity during the four first stress steps
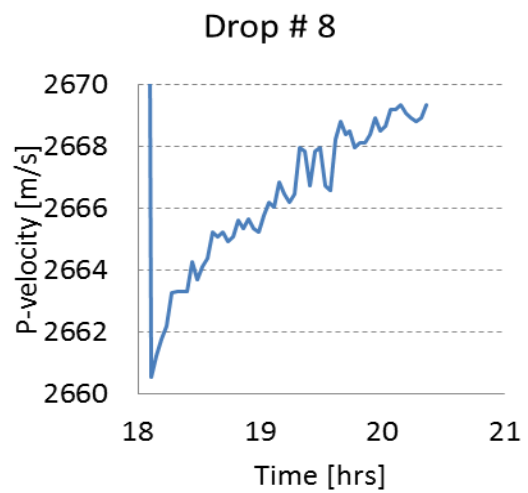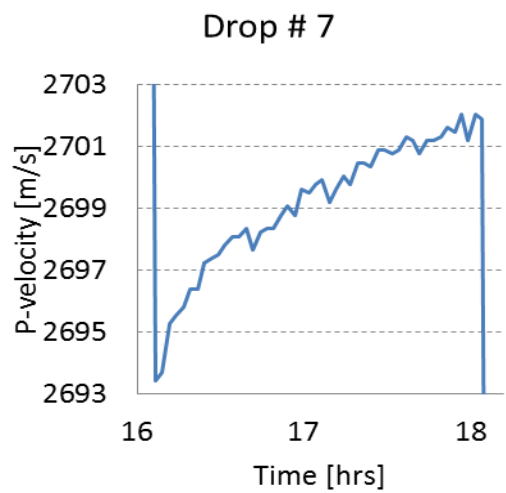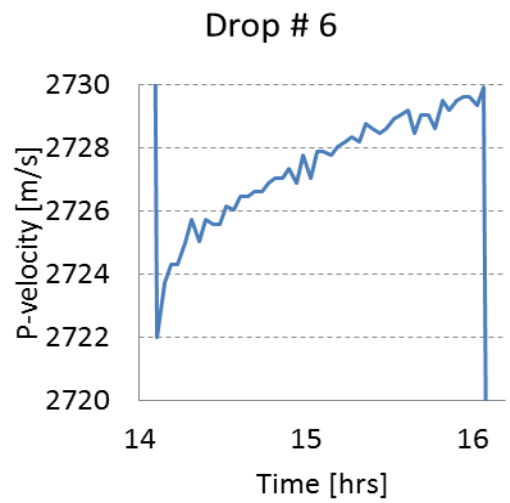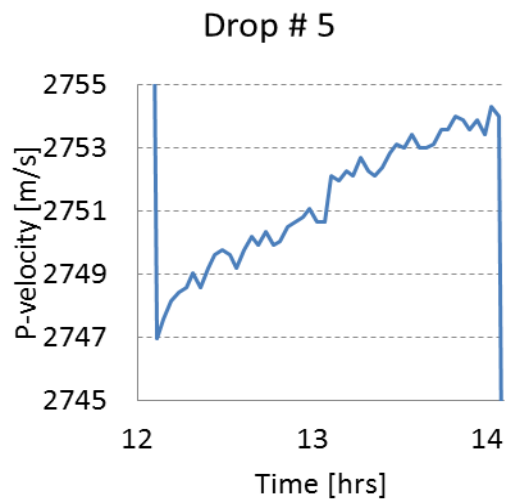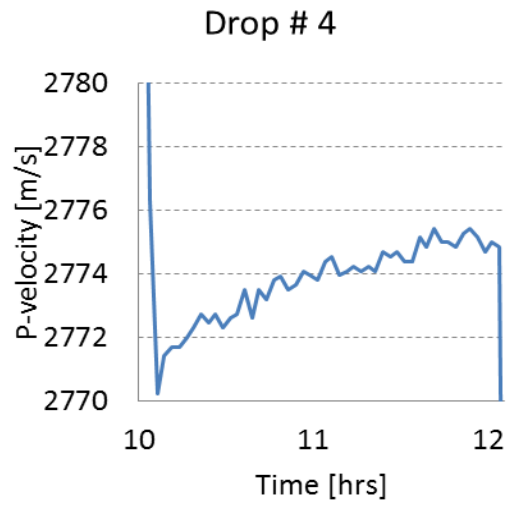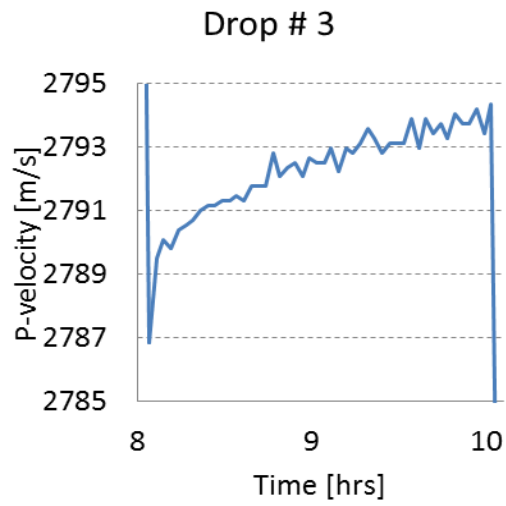
Figure IV-XXXI The transient response of the P-wave velocity during the six last stress steps

XXXII

Appendix V. Models fitted to measured data

The labeling "Increase" means hold period following an increase in stress, and "drop" means hold period following a decrease in stress

V.I Burgers Model – Finite difference

V.I.I 313_02_04
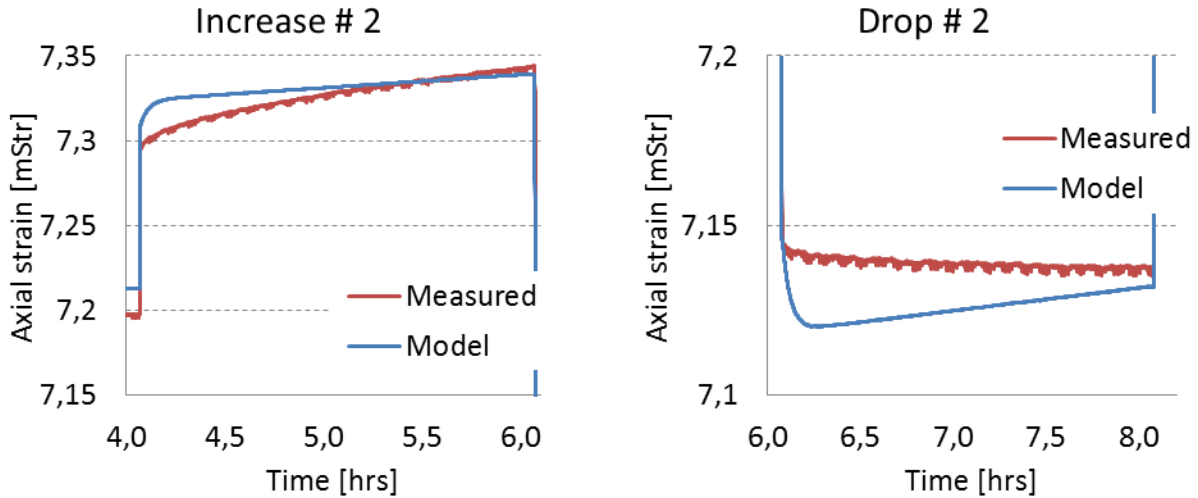
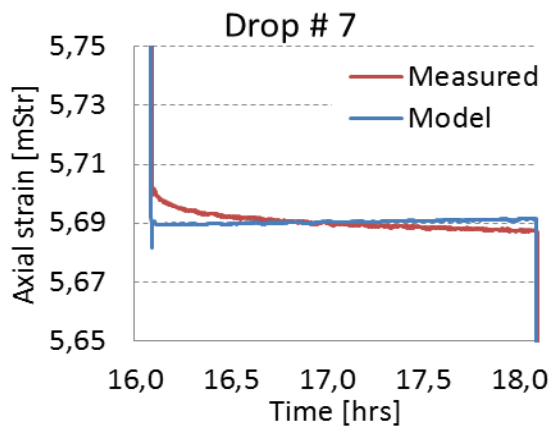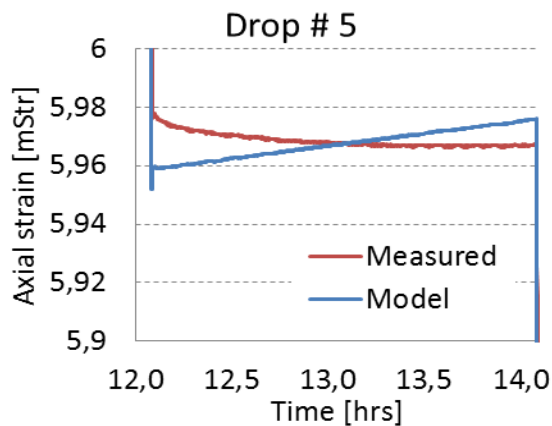
Figure V-I Left: Zoom-in of Increase #2 Right: Zoom-in of Drop # 2
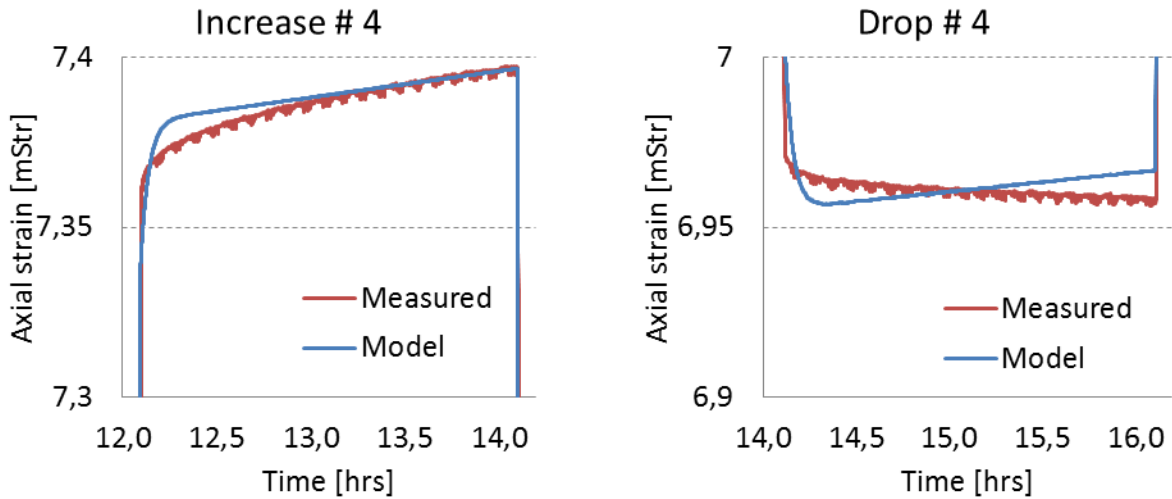
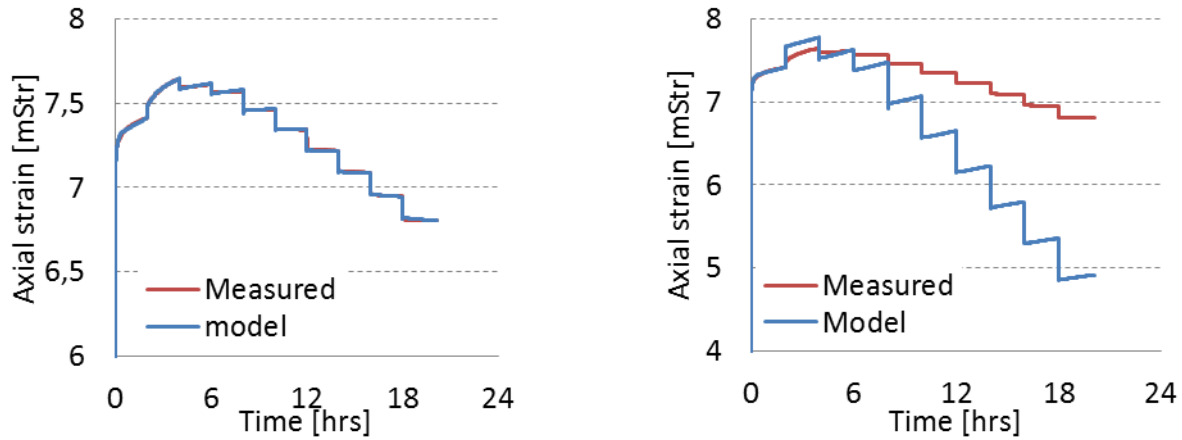*Figure V-II Left: Zoom-in of Increase # 4 Right: Zoom-in of Drop # 4*
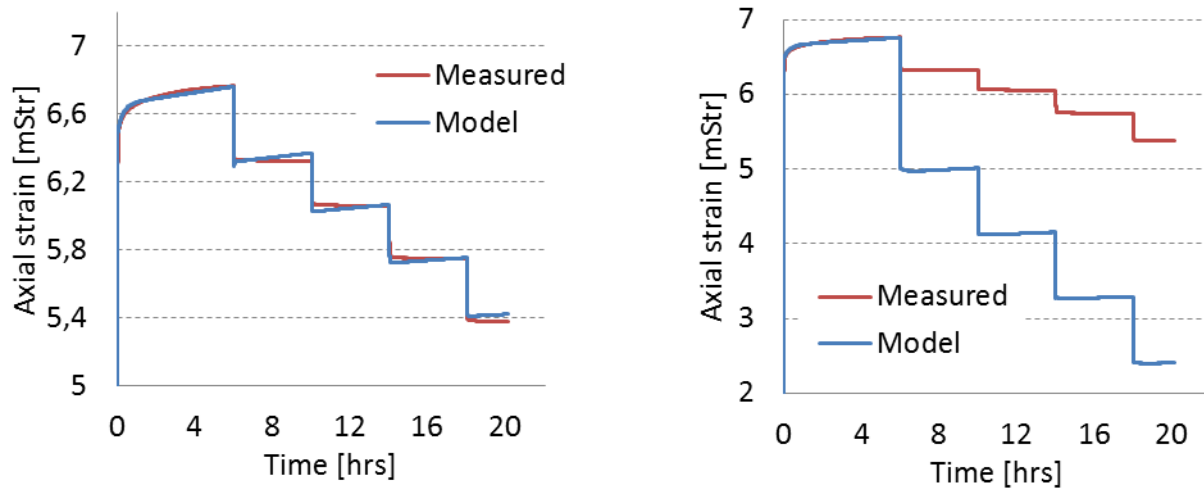
Figure V-III Burgers model fitted to measured data; Left: 2 set of parameters, Right: 1 set of paramters fitted to the first increase
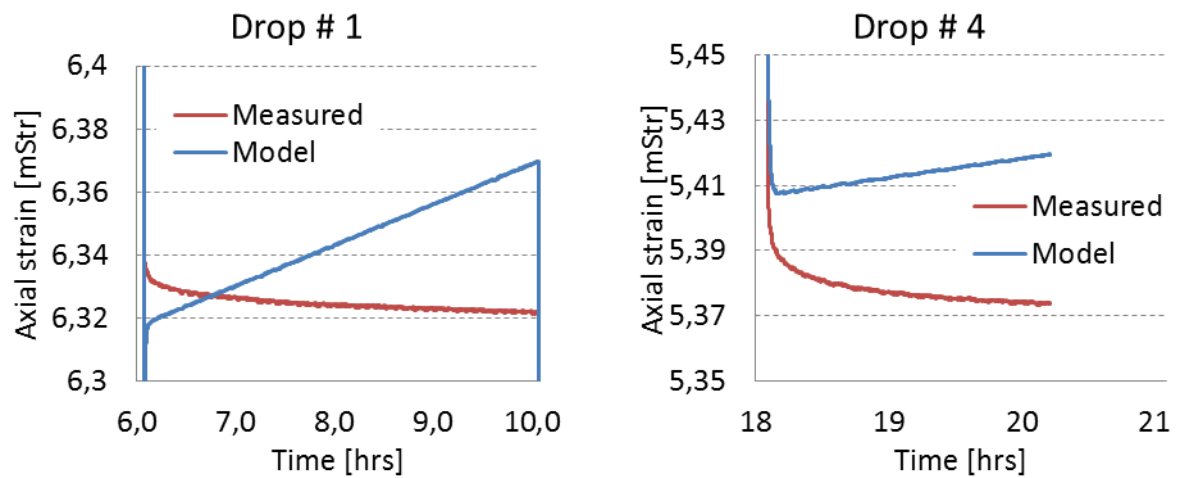
Figure V-IV Left: Magnification of the first hold period after the first drop in stree; Right: Magnification of the hold period after the fourth drop in stress
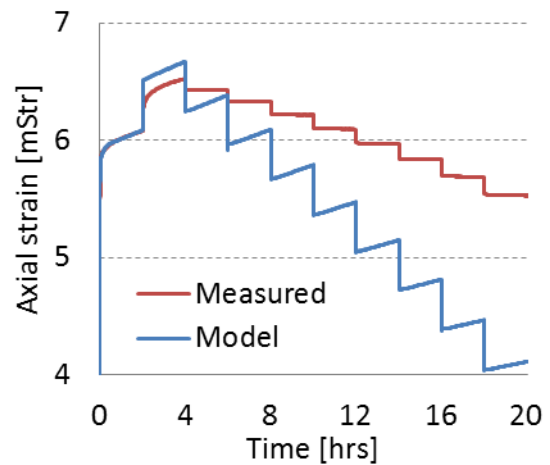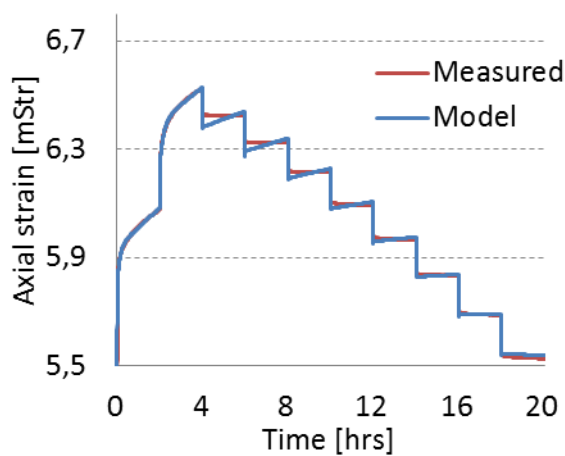
Figure V-V Burgers model fitted to measured data; Left: 3 set of parameters,
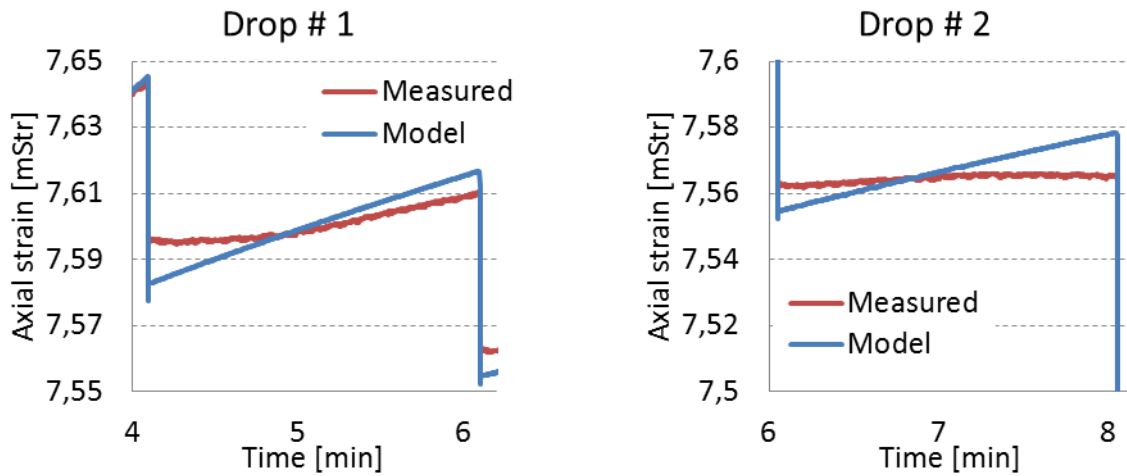*Right: 1 set of paramters fitted to the first increase*
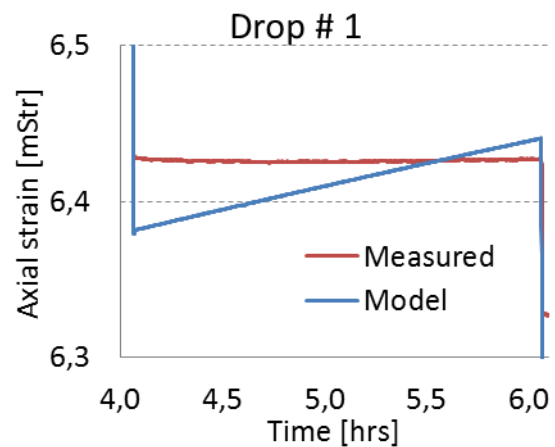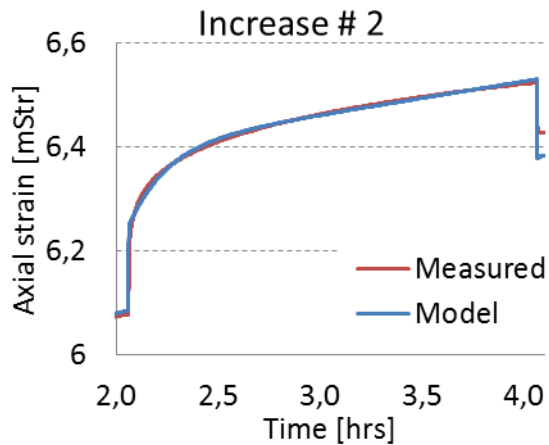
Figure V-VI Left: Zoom-in of Increase #2 Right: Zoom-in of Drop # 1

Figure V-VII Left: Zoom-in of Drop # 5 Right: Zoom-in of Drop # 7

V.I.IV   313_02_12

Figure V-VIII Burgers model fitted to measured data; Left: 3 set of parameters, Right: 1 set of paramters fitted to the first increase

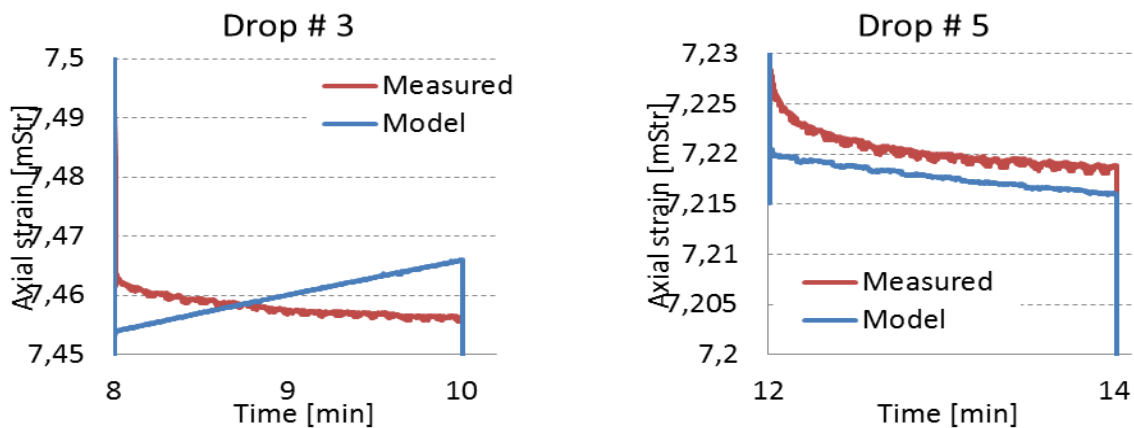*Figure V-IX Left: Zoom-in of Drop # 1 Right: Zoom-in of Drop # 2*

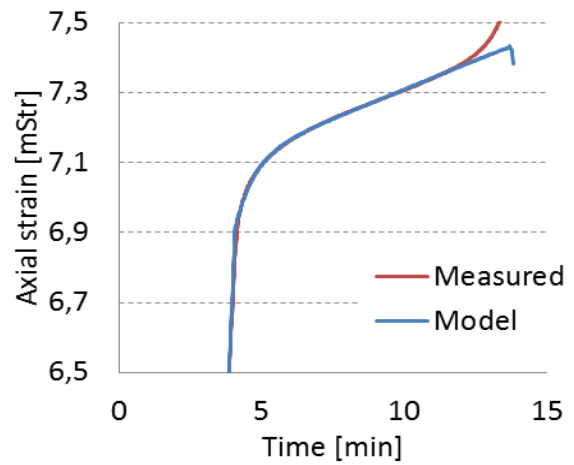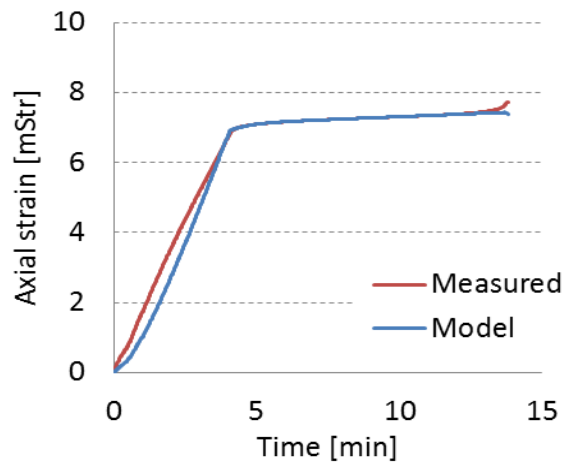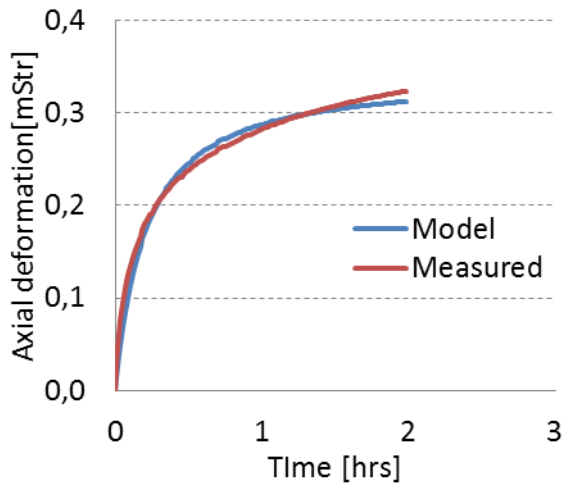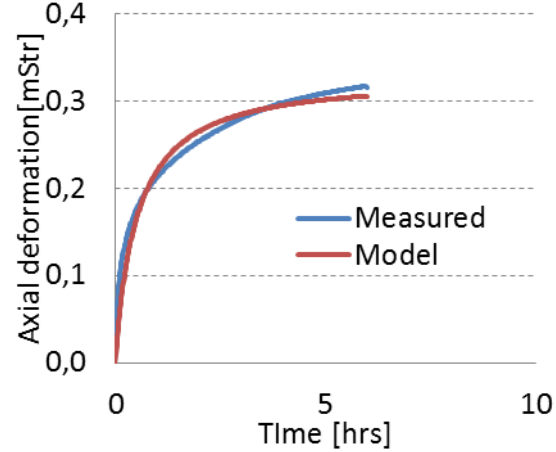*Figure V-X Left: Zoom-in of Drop # 3 Right: Zoom-in of Drop # 5*

V.I.V 313_02_13

*Figure V-XI Left: Overview comparison of the measured data and modeled data;
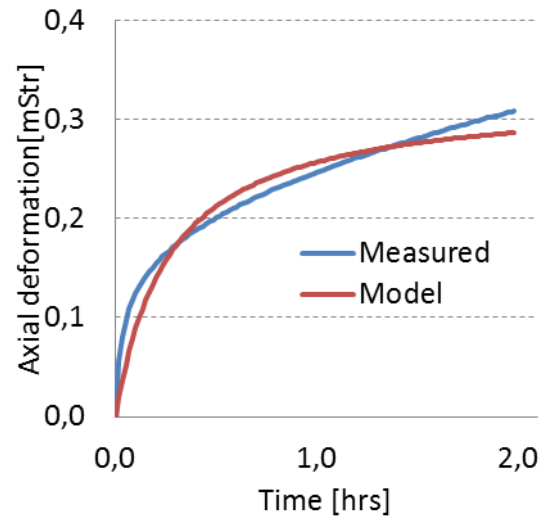Right: Zoom-in of the deformation occurring after the load period.*
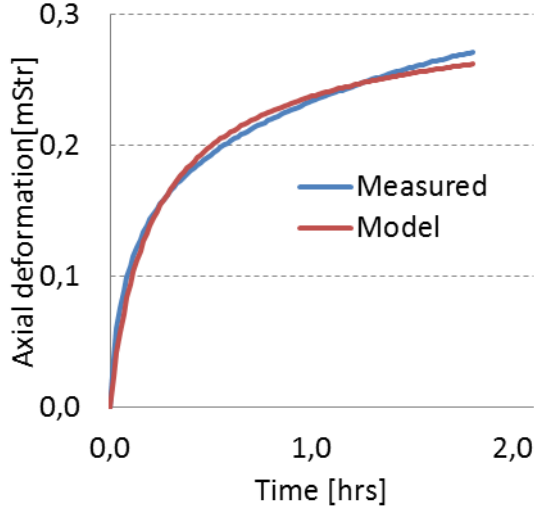
V.II FORMEL MODEL

V.III 313_02_04

V.IV   313_02_08
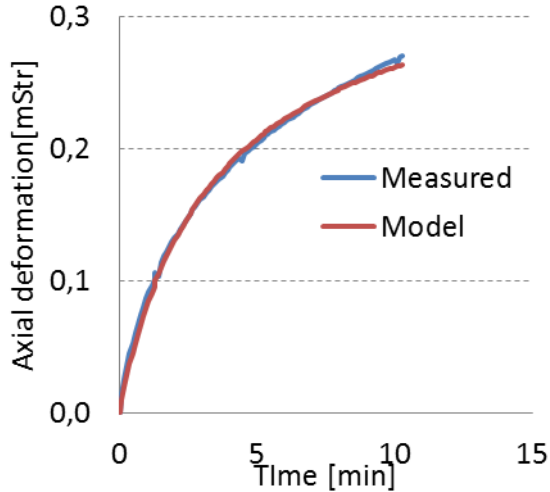

V.V   313_02_09

V.VI 313_02_12

V.VII 313_02_13

Appendix VI. Results from Specialization Project

Experiment	Stress	E1	E2	n1	n2
[#]	[MPa]				
5	13,49	8,6	1,5	4,4	59,5
7	12,97	36,1	1,3	23,4	603,3
10	11.86	56.2	1.7	50.9	645.0
11	12.75	18.2	1.4	6.8	443.0
12	12.42	30.4	1.0	75.5	409.9
13	9.95	32.7	1.1	61.3	837.0
15	12.96	49.0	1.4	93.9	970.4
16	13.10	50.0	1.0	47.4	802.2
Average	12.44	39.0	1.3	45.5	673.0
Variance	1.04	12.37	0.25	30.0	192.65
Var/avg %	8.4	31.7	19.5	66.0	28.6

Table- VI-I Summary of parameters in Burger's viscosity model

	der	dt	E*	n	q	Sigma	τ
			[MPa]		[1/Str]	[MPa]	[1/time]
5	0.60	0.17	1111.0	15.0	85.0	12.70	0.0100
10	0.00003	0.13	1969.0	1.0	110.0	11.90	0.0001
11	0.00005	0.03	1185.0	0.1	61.4	12.70	0.1300
12	0.00002	0.11	1185.0	1.3	61.4	12.70	0.0001
13	0.00005	0.10	1355.0	1.2	90.0	12.37	2.00E-06
15	0.00002	0.23	2231.0	1.6	132.5	12.84	1.00E-09
Average	0.10	0.16	1543.1	10.0	90.0	12.58	0.020
STD	0.21	0.09	411.0	17.0	23.5	0.31	0.045
STD/avg %	213.17	57.62	26.6	169.8	26.1	2.49	225.0

Table- VI-II Summary of parameters in FORMEL model